



HAL
open science

Long-term monitoring of large-scale magnetic fields across optical and near-infrared domains with ESPaDOnS, Narval, and SPIRou

S. Bellotti, J. Morin, L T Lehmann, P. Petit, G a J Hussain, J.-F. Donati, C
P Folsom, A. Carmona, E. Martioli, B. Klein, et al.

► **To cite this version:**

S. Bellotti, J. Morin, L T Lehmann, P. Petit, G a J Hussain, et al.. Long-term monitoring of large-scale magnetic fields across optical and near-infrared domains with ESPaDOnS, Narval, and SPIRou. *Astronomy and Astrophysics - A&A*, 2024, 686, pp.A66. 10.1051/0004-6361/202348043 . hal-04592914

HAL Id: hal-04592914

<https://hal.science/hal-04592914v1>

Submitted on 29 May 2024

HAL is a multi-disciplinary open access archive for the deposit and dissemination of scientific research documents, whether they are published or not. The documents may come from teaching and research institutions in France or abroad, or from public or private research centers.





















L'archive ouverte pluridisciplinaire **HAL**, est destinée au dépôt et à la diffusion de documents scientifiques de niveau recherche, publiés ou non, émanant des établissements d'enseignement et de recherche français ou étrangers, des laboratoires publics ou privés.



Distributed under a Creative Commons Attribution 4.0 International License

Long-term monitoring of large-scale magnetic fields across optical and near-infrared domains with ESPaDOnS, Narval, and SPIRou

The cases of EV Lac, DS Leo, and CN Leo[★]

S. Bellotti^{1,2} , J. Morin³ , L. T. Lehmann¹ , P. Petit¹ , G. A. J. Hussain² , J.-F. Donati¹ , C. P. Folsom⁴ , A. Carmona⁵ , E. Martioli^{6,7} , B. Klein⁸ , P. Fouqué¹ , C. Moutou¹ , S. Alencar⁹, E. Artigau¹⁰ , I. Boisse¹¹ , F. Bouchy¹² , J. Bouvier⁵ , N. J. Cook¹⁰ , X. Delfosse⁵ , R. Doyon¹⁰ , and G. Hébrard^{7,13} 

¹ Institut de Recherche en Astrophysique et Planétologie, Université de Toulouse, CNRS, IRAP/UMR 5277, 14 Avenue Edouard Belin, 31400 Toulouse, France

e-mail: stefano.bellotti@irap.omp.eu

² Science Division, Directorate of Science, European Space Research and Technology Centre (ESA/ESTEC), Keplerlaan 1, 2201 AZ Noordwijk, The Netherlands

³ Laboratoire Univers et Particules de Montpellier, Université de Montpellier, CNRS, 34095 Montpellier, France

⁴ Tartu Observatory, University of Tartu, Observatooriumi 1, Tõravere 61602 Tartumaa, Estonia

⁵ Univ. Grenoble Alpes, CNRS, IPAG, 38000 Grenoble, France

⁶ Laboratório Nacional de Astrofísica, Rua Estados Unidos 154, 37504-364 Itajubá, MG, Brazil

⁷ Institut d'Astrophysique de Paris, CNRS, UMR 7095, Sorbonne Université, 98 bis bd Arago, 75014 Paris, France

⁸ Sub-department of Astrophysics, Department of Physics, University of Oxford, Oxford OX1 3RH, UK

⁹ Universidade Federal de Minas Gerais, Belo Horizonte, MG 31270-901, Brazil

¹⁰ Université de Montréal, Département de Physique, IREX, Montréal, QC H3C 3J7, Canada

¹¹ Aix Marseille Univ, CNRS, CNES, LAM, Marseille, France

¹² Observatoire de Genève, Université de Genève, Chemin Pegasi, 51, 1290 Sauverny, Switzerland

¹³ Observatoire de Haute Provence, St Michel l'Observatoire, France

Received 22 September 2023 / Accepted 5 March 2024

ABSTRACT

Context. Dynamo models describing the generation of stellar magnetic fields for partly and fully convective stars are guided by observational constraints. Zeeman-Doppler imaging has revealed a variety of magnetic field geometries and, for fully convective stars in particular, a dichotomy: either strong, mostly axisymmetric, and dipole-dominated or weak, non-axisymmetric, and multipole-dominated. This dichotomy is explained either by dynamo bistability (i.e., two coexisting and stable dynamo branches) or by long-term magnetic cycles with polarity reversals, but there is no definite conclusion on the matter.

Aims. Our aim is to monitor the evolution of the large-scale field for a sample of nearby M dwarfs with masses between 0.1 and 0.6 M_{\odot} , which is of prime interest to inform distinct dynamo theories and explain the variety of magnetic field geometries studied in previous works. This also has the potential to put long-term cyclic variations of the Sun's magnetic field into a broader context.

Methods. We analysed optical spectropolarimetric data sets collected with ESPaDOnS and Narval between 2005 and 2016, and near-infrared SPIRou data obtained between 2019 and 2022 for three well-studied, active M dwarfs: EV Lac, DS Leo, and CN Leo. We looked for secular changes in time series of longitudinal magnetic field, width of unpolarised mean-line profiles, and large-scale field topology as retrieved with principal component analysis and Zeeman-Doppler imaging.

Results. We retrieved pulsating (EV Lac), stable (DS Leo), and sine-like (CN Leo) long-term trends in longitudinal field. The width of near-infrared mean-line profiles exhibits rotational modulation only for DS Leo, whereas in the optical it is evident for both EV Lac and DS Leo. The line width variations are not necessarily correlated to those of the longitudinal field, suggesting complex relations between small- and large-scale field. We also recorded topological changes in the form of a reduced axisymmetry for EV Lac and transition from a toroidal-dominated to poloidal-dominated regime for DS Leo. For CN Leo, the topology remained predominantly poloidal, dipolar, and axisymmetric, with only an oscillation in field strength.

Conclusions. Our results show a peculiar evolution of the magnetic field for each M dwarf individually, with DS Leo and EV Lac manifesting more evident variations than CN Leo. These findings confirm that M dwarfs with distinct masses and rotation periods can undergo magnetic long-term variations and suggest an underlying variety of cyclic behaviours of their magnetic fields.

Key words. techniques: polarimetric – stars: activity – stars: magnetic field – stars: individual: EV Lac – stars: individual: DS Leo – stars: individual: CN Leo

1. Introduction

The magnetic fields of low-mass stars ($M_* < 1.2 M_{\odot}$) are powered by dynamos (Schrijver & Zwaan 2000), and their study is

* The reduced data are available at the CDS via anonymous ftp to cdsarc.cds.unistra.fr (130.79.128.5) or via <https://cdsarc.cds.unistra.fr/viz-bin/cat/J/A+A/686/A66>

paramount to understanding stellar evolution and activity phenomena. The evolution of a star's rotation is linked to magnetic activity as the magnetic field couples with the stellar wind and results in angular momentum loss over the star's lifetime (Skumanich 1972; Vidotto et al. 2014; Finley & Matt 2017; See et al. 2019). Therefore, one can infer the stellar age and rotation period using magnetic activity as a proxy (Noyes et al.

1984; Lorenzo-Oliveira et al. 2018; Dungee et al. 2022). Moreover, stellar magnetic activity is responsible for inhomogeneities in brightness (spots, faculae, plages) and local velocity fields (suppression of convection) that may prevent the unambiguous detection and characterisation of exoplanets, especially those similar to the Earth (Queloz et al. 2001; Huerta et al. 2008; Meunier 2021). Finally, the stellar magnetism dictates the environment in which exoplanets orbit (e.g., Folsom et al. 2020; Bellotti et al. 2023a), influencing their potential habitability (e.g., Segura et al. 2010; Vidotto et al. 2013; Luger & Barnes 2015; Tilley et al. 2019).

On the low-mass end of the main sequence, M dwarfs are the most common spectral type in the solar neighbourhood (Reid et al. 2004), with masses ranging between 0.08 and $0.57 M_{\odot}$ (Pecaut & Mamajek 2013). Above $0.35 M_{\odot}$ (approximately M3.5 type), the internal structure is solar-like, that is, with an inner radiative core and an outer convective envelope separated by the tachocline (Chabrier & Baraffe 1997). The tachocline is an interface region of strong shear, where the magnetic field is thought to be amplified. Below $0.35 M_{\odot}$, M dwarfs possess fully convective interiors, and the absence of a tachocline challenges dynamo theories relying on a deep-seated interface (Durney et al. 1993; Chabrier & Küker 2006; Browning 2008; Yadav et al. 2015). Overall, M dwarfs represent exquisite laboratories to study dynamo-powered magnetic field generation, under similar and different physical interior conditions to those of the Sun.

Dynamo theories are informed by observations of stellar magnetic fields, which can be measured using two complementary approaches (Reiners 2012; Kochukhov 2021). The modulus of the magnetic field vector is estimated via radiative transfer modelling of Zeeman splitting and magnetic intensification of individual unpolarised spectral lines. Values of field strength between 0.2 and 7 kG have been reported (Shulyak et al. 2017, 2019; Reiners et al. 2022; Cristofari et al. 2023), and they follow the activity-rotation relation exhibiting a (quasi-)saturated and non-saturated regime (Reiners & Basri 2009; Shulyak et al. 2019; Reiners et al. 2022). The geometry of the large-scale field can be inferred by means of tomographic inversion techniques, for example Zeeman–Doppler imaging (ZDI; Semel 1989; Donati & Brown 1997) applied to spectropolarimetric time series of linearly and circularly polarised spectra (Morin et al. 2012).

The application of ZDI to spectropolarimetric data of partly and fully convective low-mass stars have revealed a wide variety of large-scale field geometries (e.g., Donati et al. 2008; Morin et al. 2008, 2010; Fares et al. 2013; Hébrard et al. 2016). Partly convective stars with masses higher than $0.5 M_{\odot}$ tend to have weak, predominantly toroidal, and non-axisymmetric fields, whereas stars with masses between 0.35 and $0.5 M_{\odot}$ harbour stronger, poloidal, and axisymmetric fields (Donati et al. 2008; Phan-Bao et al. 2009). For fully convective stars close to the $0.35 M_{\odot}$ boundary, the large-scale field is strong, mainly poloidal, and axisymmetric, while below $M < 0.2 M_{\odot}$ a dichotomy of topologies co-exist: weak, complex, and non-axisymmetric or strong, simple, and axisymmetric (Morin et al. 2008, 2010). This dichotomy can be explained by either two distinct and independent branches of dynamo known as bistability (Morin et al. 2011; Gastine et al. 2013; Kochukhov & Lavail 2017) or by assuming that fully convective M dwarfs undergo magnetic cycles, and previous ZDI reconstructions captured only a snapshot of a long-term topological variation (Kitchatinov et al. 2014). However, no definitive interpretation has been reached so far.

The Sun is an important benchmark for stellar cycles, because the large-scale dipolar component of the magnetic

field undergoes a polarity reversal in a cyclical fashion every 11 yr, and it is accompanied by an oscillation in the fraction of poloidal-to-toroidal magnetic energy (Sanderson et al. 2003; Charbonneau 2010). More precisely, the poloidal component peaks at cycle minimum, and the toroidal components increase towards cycle maximum. However, our understanding of the cyclic nature of the solar magnetism is still not complete (Charbonneau 2020), and its contextualisation advocates for additional magnetic field observations of distinct stellar types. In this direction, informing dynamo theories requires a long-term spectropolarimetric monitoring of selected M dwarfs, for which we can trace the secular evolution of the large-scale field geometry (Klein et al. 2021, 2022; Bellotti et al. 2023b). There is observational evidence of activity cycles for M dwarfs, from photometric and chromospheric activity monitoring (e.g., Suárez Mascareño et al. 2016, 2018; Fuhrmeister et al. 2023; Mignon et al. 2023), and from radial velocity searches of exoplanets (da Gomes Silva et al. 2012; Wargelin et al. 2017; Lopez-Santiago et al. 2020), but we are only starting to capture long-term behaviour that may resemble solar-like magnetic cycles (Bellotti et al. 2023b; Lehmann et al. 2024). For instance, the recent work of Bellotti et al. (2023b) reports the long-term evolution of the magnetic field of AD Leo, which has similarities with the evolution of the Sun’s field.

With this work we investigate the long-term monitoring of three active M dwarfs, EV Lac, DS Leo, and CN Leo, by analysing spectropolarimetric data collected across the optical and near-infrared domain. To investigate the long-term evolution, we analysed the full time series of the longitudinal magnetic field (B_l) and the full width at half maximum (FWHM) of unpolarised (Stokes I) mean-line profiles. We reconstructed the large-scale field topology via ZDI, and we inspected temporal changes in the morphology of circular polarisation profiles via principal component analysis (PCA; Lehmann & Donati 2022). The paper is structured as follows. In Sect. 2 we describe the near-infrared and optical spectropolarimetric observations. We outline the analysis of the longitudinal magnetic field in Sect. 3, the analysis FWHM of Stokes I in Sect. 4, the PCA technique in Sect. 5, and the ZDI reconstructions in Sect. 6. Finally, we present our conclusions in Sect. 7.

2. Observations

We used spectropolarimetric data collected in near-infrared and optical domains, and performed a large-scale magnetic field monitoring for three M-type stars: EV Lac (GJ 873), DS Leo (GJ 410), and CN Leo (GJ 406). A summary of their properties is given in Table 1.

According to stellar models, the transition between partly and fully convective interiors spans from 0.20 to $0.35 M_{\odot}$ (Dorman et al. 1989; Chabrier & Baraffe 1997; Rabus et al. 2019). Other factors like age, metallicity and magnetic field strength play a role (Mullan & MacDonald 2001; Maeder & Meynet 2000; van Saders & Pinsonneault 2012; Tanner et al. 2013). With such a range, DS Leo and CN Leo are partly and fully convective, respectively. With a mass of $0.32 M_{\odot}$, EV Lac is either partly convective or near the transition between the two regimes.

2.1. Near-infrared

All near-infrared observations were performed in circular polarisation mode with the SpectroPolarimètre InfraRouge (SPIRou)

Table 1. Properties of the M dwarfs examined.

Star	ID	Sp type	M_* [M_\odot]	R_* [R_\odot]	P_{rot} [d]	$v_{\text{eq}} \sin i$ [km s^{-1}]	i [deg]	$\log(L_X/L_{\text{bol}})$ [dex]	$\log R'_{\text{HK}}$ [dex]
DS Leo	GJ 410	M1.0	0.58	0.53	$13.91 \pm 0.01^{(\dagger)}$	2.0	60	-3.80	-4.16
EV Lac	GJ 873	M3.5	0.32	0.30	$4.36 \pm 0.01^{(\dagger)}$	4.0	60	-1.99	-3.75
CN Leo	GJ 406	M5.5	0.10	0.12	$2.70 \pm 0.01^{(\dagger)}$	2.0	$45 \pm 20^{(\dagger)}$...	-4.01

Notes. The columns list the following quantities: 1) and 2) stellar name and alternative identifier, 3) spectral type, 4) mass, 5) radius, 6) rotation period at equator, 7) equatorial projected rotational velocity, 8) inclination, 9) X-ray-to-bolometric luminosity ratio (Wright et al. 2011), and 10) CaII H&K index (Noyes et al. 1984; Boro Saikia et al. 2018). Columns 4) and 5) are from Cristofari et al. (2023), and columns 7) and 8) are from Morin et al. (2008), Hébrard et al. (2016), and Cristofari et al. (2023). Columns 9) and 10) are from Wright et al. (2011), Stelzer et al. (2013) and Boro Saikia et al. (2018), respectively. The dagger (\dagger) indicates that the parameter was estimated in this work.

as part of the large programme SPIRou Legacy Survey¹ (SLS; id P42, PI: Jean-François Donati). SPIRou is a stabilised high-resolution near-infrared spectropolarimeter (Donati et al. 2020) mounted on the 3.6 m Canada-France-Hawaii Telescope (CFHT) atop Maunakea, Hawaii. It provides a quasi-continuous coverage of the near-infrared spectrum from 0.96 to 2.5 μm (*YJHK* bands) at a spectral resolving power of $R \sim 70\,000$, with a 2-nm gap between 2.4371 and 2.4391 μm (Donati et al. 2020). Optimal extraction of SPIRou spectra was carried out with A PipelinE to Reduce Observations (APER0 v0.6.132), a fully automatic reduction package installed at CFHT (Cook et al. 2022). The journal of the observations is given in Appendix E.

Starting from the polarimetric products of APER0 (see Cook et al. 2022, for more details), we computed Stokes I (unpolarised) and V (circularly polarised) mean profiles using least-squares deconvolution (LSD; Donati et al. 1997; Kochukhov et al. 2010).² With this technique the observed spectrum is deconvolved with a line list, namely a series of Dirac delta functions located at each absorption line in the stellar spectrum and with the associated line features such as depth, and sensitivity to Zeeman effect (commonly known as Landé factor and indicated as g_{eff}). The deconvolution results in an individual, high-signal-to-noise ratio (S/N) kernel summarising the properties of thousands of spectral lines, and allowing us to extract polarimetric information from the spectrum.

For our stars, we used two line lists corresponding to a local thermodynamic equilibrium model (Gustafsson et al. 2008) characterised by $\log g = 5.0 [\text{cm s}^{-2}]$, $v_{\text{micro}} = 1 \text{ km s}^{-1}$, and $T_{\text{eff}} = 3000 \text{ K}$ (for CN Leo) and $T_{\text{eff}} = 3500 \text{ K}$ (for EV Lac and DS Leo). These two lists contain 1000 and 1400 atomic photospheric lines between 950 and 2600 nm with depth larger than 3% the continuum level. The depth threshold is chosen to remove shallow lines (with low effective S/N), while keeping a large number of lines with which to compute LSD profiles. The masks were synthesised using the Vienna Atomic Line Database³ (VALD, Ryabchikova et al. 2015), and contain information on g_{eff} (ranging from 0 to 3), which is not accessible with an empirical or molecular mask. Given the spectral type of EV Lac and DS Leo, we respectively tested a mask associated with 3000 K (590 lines) 4000 K (1550 lines), to check the robustness of our results. For both Stokes I and V , we adopted the weighting factor $dg_{\text{eff}}\lambda/(d_n g_{\text{eff},n} \lambda_n)$, with d is the line depth

and λ is the wavelength, whereas the quantities at denominator are the normalisation parameters (see Kochukhov et al. 2010, for more details).

A forest of telluric absorption lines due to the Earth's atmosphere pollute the wavelength domain in which SPIRou operates. As described in Cook et al. (2022) and Artigau et al. (2022), the removal of telluric contamination from science data is performed by APER0 with a two-step algorithm. First, a pre-cleaning is carried out by means of a TAPAS (Transmissions of the Atmosphere for Astronomical data; Bertaux et al. 2014) absorption model, which is also applied to a set of hot stars to obtain a library of telluric-correction residuals. From this, a telluric-residuals model is constructed and subtracted from the science frames. To account for potential residuals in the telluric correction, we ignored the following intervals of the spectrum when computing the LSD profiles: [950, 979], [1081, 1169], [1328, 1492], [1784, 2029], [2380, 2500] nm. These correspond to spectral windows where the telluric absorption is highest. The final number of spectral lines used in LSD is 588 and 830 for the $T_{\text{eff}} = 3000 \text{ K}$ and $T_{\text{eff}} = 3500 \text{ K}$ line lists, respectively.

We show an example of LSD Stokes profiles for the examined stars in Fig. 1. As mentioned by Lavail et al. (2018), the continuum of the Stokes I LSD profiles for M dwarfs lies below unity owing to molecular spectral lines that are not accounted in the line lists. We thus re-normalised the profiles to unity by fitting a linear model to the region outside the line, to include residuals of continuum normalisation at the level of the spectra. The Stokes V and N profiles were correspondingly re-scaled with the same fit. The operation of continuum normalisation does not alter the magnetic analyses presented here appreciably. For instance, the longitudinal field values computed with non-normalised LSD profiles are at most 5% larger compared to the values obtained from normalised LSD profiles. In a similar manner, the retrieved field topology and evolution are robust against LSD profiles normalisation, as long as a multi-epoch time series for a particular target is analysed in a consistent way.

EV Lac was observed for 163 nights between September 2019 and November 2021, spanning a period of ~ 800 days. We split the entire time series in smaller epochs based on the instrumental scheduling and visibility gaps, following Bellotti et al. (2023b). We obtained three epochs: 2019b (35 obs between 2019.86 and 2019.95), 2020b2021a (67 observations between 2020.57 and 2021.02) and 2021b (61 observations between 2021.47 and 2021.72). We recorded a S/N at 1650 nm per spectral element between 31 and 165, with a mean of 130, and an average airmass of 1.2.

DS Leo was observed for 130 nights between November 2020 and June 2022, spanning a period of ~ 580 days. The time series was split in two epochs: 2020b2021a (61 observations

¹ <http://spirou.irap.omp.eu/Observations/The-SPIRou-Legacy-Survey>

² We used the python LSD code available at <https://github.com/folsomcp/LSDpy>

³ <http://vald.astro.uu.se/> using the Montpellier mirror to request locally MARCS model atmospheres.

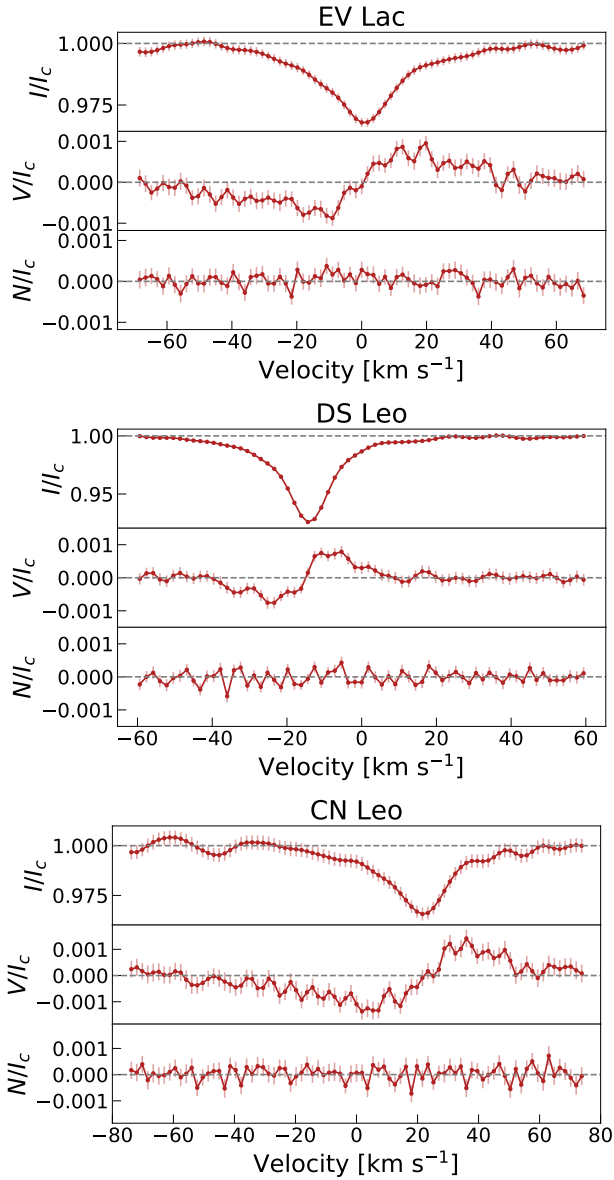


Fig. 1. Examples of Stokes profiles obtained with SPIRou for EV Lac, DS Leo and CN Leo. In each panel, Stokes I (top), V (middle), and null polarisation profile (bottom; see Bagnulo et al. 2009) are illustrated in units of unpolarised continuum (I_c). Clear circular polarisation signatures are present, with a S/N of 5000, 5600, and 3080 for EV Lac, DS Leo, and CN Leo, respectively. The different magnetic activity level of the stars is shown by the different widths of the average line profiles in both unpolarised and polarised light.

between 2020.27 and 2021.55) and 2021b2022a (69 observations between 2021.71 and 2022.46). The S/N ranged between 51 and 151, with a mean of 125, and the mean airmass is 1.3.

CN Leo was observed for 169 nights between April 2019 and June 2022, spanning a period of ~ 1150 days. The time series was split in four epochs: 2019a (19 observations between 2019.29 and 2019.47), 2019b2020a (37 observations between 2019.83 and 2020.44) and 2020b2021a (63 observations between 2020.83 and 2021.50) 2021b2022a (45 observations between 2021.87 and 2022.44). The S/N ranged between 40 and 146, with a mean of 111, and the average airmass is 1.3. Six observations in February 2019 were excluded due to an opti-

cal component not working nominally at very low temperatures, in a similar way to Bellotti et al. (2023b).

2.2. Optical

We used archival optical spectropolarimetric observations collected with ESPaDOnS and Narval. ESPaDOnS is the spectropolarimeter on the 3.6 m CFHT located atop Mauna Kea in Hawaii (Donati et al. 2006a), and Narval is the twin instrument on the 2 m *Télescope Bernard Lyot* (TBL) at the Pic du Midi Observatory in France (Donati 2003). Data reduction was performed with LIBRE-ESPRIT (Donati et al. 1997), and the continuum normalised spectra were retrieved from PolarBase (Petit et al. 2014).

The optical data sets were already examined in previous studies (Donati et al. 2008; Morin et al. 2008, 2010; Hébrard et al. 2016). For EV Lac, there are 79 observations taken between 2005 and 2016. The 2010 observations were affected by a malfunction of the rhombs which affected the circular polarisation signal, hence only the Stokes I data are used in the following analyses. For DS Leo, there are 94 observations between 2006 and 2014. For CN Leo, there are four observations in 2008, which we included only for the FWHM analysis (see Sect. 4).

Similarly to the near-infrared, we computed Stokes I and V profiles with LSD. For EV Lac and DS Leo, we adopted an optical 3500 K VALD mask containing 3240 lines in range 350–1080 nm and with depths larger than 40% the continuum level, similarly to Morin et al. (2008), Bellotti et al. (2022). For CN Leo, we used a 3000 K mask built in a similar manner and containing 3492 absorption lines. The number of lines in both masks already accounts for the removal of the wavelength intervals affected by telluric lines analogously to Bellotti et al. (2022). These are: [627,632], [655.5,657], [686,697], [716,734], [759,770], [813,835], and [895,986] nm. In the next sections, the observations will be phased with the following ephemeris

$$\text{HJD}_{\text{EVLac}} = 2\,458\,738.0805 + P_{\text{rot,EVLac}} \cdot n_{\text{cyc}} \quad (1)$$

$$\text{HJD}_{\text{DSLLeo}} = 2\,459\,158.1132 + P_{\text{rot,DSLLeo}} \cdot n_{\text{cyc}} \quad (2)$$

$$\text{HJD}_{\text{CNLeo}} = 2\,458\,590.0095 + P_{\text{rot,CNLeo}} \cdot n_{\text{cyc}} \quad (3)$$

where we separately used the first SPIRou observation for each star as heliocentric Julian Date reference, $P_{\text{rot},i}$ is the stellar rotation period of the i th star (see Sect. 3), and n_{cyc} represents the rotation cycle (tabulated in Appendix E).

3. Longitudinal magnetic field

The disk-integrated, line-of-sight component of the magnetic field (B_l) is computed from the first-order moment of a Stokes V profile (Rees & Semel 1979; Folsom et al. 2016). Formally,

$$B_l [\text{G}] = \frac{-2.14 \times 10^{11}}{\lambda_0 g_{\text{eff}} c} \frac{\int v V(v) dv}{\int (I_c - I) dv}, \quad (4)$$

where λ_0 and g_{eff} are the normalisation wavelength (in nm) and Landé factor of the LSD profiles, I_c is the continuum level, v is the radial velocity associated to a point in the spectral line profile in the star's rest frame (in km s^{-1}) and c the speed of light in vacuum (in km s^{-1}).

For all stars examined, the adopted normalisation wavelength is 1700 nm and 700 nm for the near-infrared and optical domains, respectively. The normalisation Landé factor is 1.191

in near-infrared and 1.154 in optical for EV Lac, 1.181 and 1.086 for DS Leo, and 1.223 for CN Leo (only near-infrared). Considering the larger line width in near-infrared than optical, the integration is computed within $\pm 50 \text{ km s}^{-1}$ and $\pm 30 \text{ km s}^{-1}$ from line centre for EV Lac and within $\pm 60 \text{ km s}^{-1}$ and $\pm 30 \text{ km s}^{-1}$ for CN Leo. For DS Leo, the integration intervals are $\pm 25 \text{ km s}^{-1}$ and $\pm 20 \text{ km s}^{-1}$, since it is a slower rotator.

The longitudinal field is a useful diagnostic of surface magnetic features, whose appearance on the visible disk is modulated at the stellar rotation period. For this reason, practical information can be extracted from the time series of B_l values with standard techniques (Folsom et al. 2018; Petit et al. 2021; Carmona et al. 2023; Fouqué et al. 2023; Donati et al. 2023b). We applied a Generalised Lomb-Scargle periodogram (Zechmeister & Kürster 2009) to the entire time series as well as the individual subsets of data for all the examined stars. The results are illustrated in Fig. 2.

For EV Lac and DS Leo, the peak at the expected rotation period is unambiguously higher than a false alarm probability (FAP) of 0.01%, which emphasises the dominant stellar activity signal and confirms B_l as suitable diagnostic. For CN Leo, the interpretation of the periodogram is more elaborate because of strong aliases of the observational cadence ($\sim 1 \text{ d}$), the gap between instrument runs ($\sim 30 \text{ d}$), and the time span of the time series ($\sim 1000 \text{ d}$). By ignoring these features, the periodogram shows a clear and unique peak at the expected stellar rotation period, for which there is no correspondence with the observing window function. If we restrict the periodogram analysis to each the four subsets of CN Leo (see Sect. 2), only the last one 2021b2022a does not show a spike at the expected rotation period. For all stars, we retrieve P_{rot} in agreement to known values from the literature: $P_{\text{rot, EV Lac}} = 4.36 \pm 0.01 \text{ d}$ (Morin et al. 2008), $P_{\text{rot, DS Leo}} = 13.91 \pm 0.01 \text{ d}$ (Hébrard et al. 2016), and $P_{\text{rot, CN Leo}} = 2.70 \pm 0.01 \text{ d}$ (Reinhold & Hekker 2020; Lafarga et al. 2021; Irving et al. 2023).

The longitudinal field computation was carried out for both optical and near-infrared domains for all stars, and is shown in Figs. 3–5. The journal of B_l values is reported in Appendix E.

3.1. EV Lac

EV Lac’s near-infrared measurements lie between 270 and -470 G , with a mean of -50 G and a median error bar of 19 G . In comparison, the optical data have a larger spread, ranging between 380 and -540 G with a mean of -90 G and a median error bar of 16 G . When a 3000 K, near-infrared mask is used to compute the LSD profiles, the range of B_l spans between -480 and 286 G , with a mean of -52 G and a median error bar of 21 G . The Stokes I profiles derived with the colder mask are on average 20% deeper than those associated with the 3500 K mask, and the amplitude of Stokes V profiles is on average $\sim 20\%$ larger. These differences in the Stokes profiles cancel out according to Eq. (4), ultimately making the results consistent. Overall, the near-infrared B_l values seem to progressively restore the amplitude with time, after a potential minimum in 2016, making the overall trend look like a beating signal. However, the dearth of data between 2010 and 2019 prevents us from constraining the phenomenon further.

When EV Lac’s near-infrared data are phase-folded at $P_{\text{rot, EV Lac}} = 4.36 \text{ d}$, we note a clear rotational modulation for the three epochs (see Fig. 3). The phase variations are modelled with a Levenberg–Marquardt least squares sine fit, and we observe an increasing amplitude of the field variations, indicating a decrease in the field axisymmetry or a field enhancement

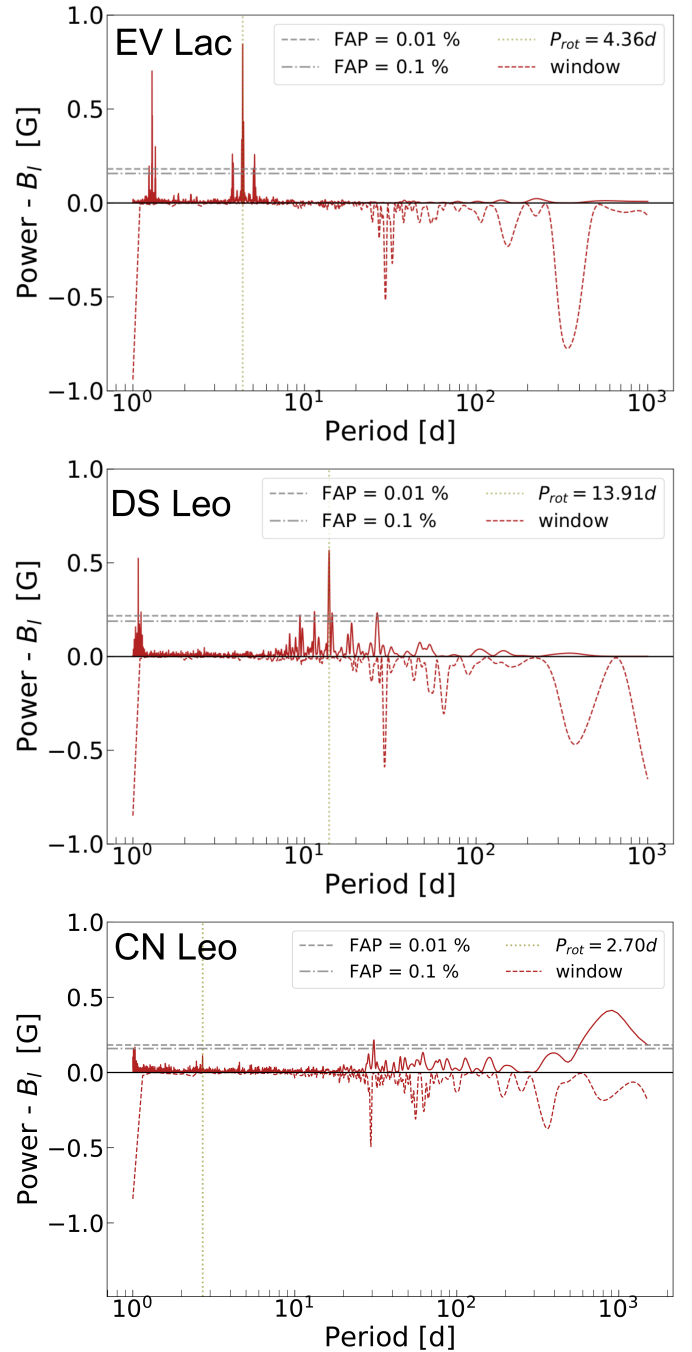


Fig. 2. Generalised Lomb-Scargle periodogram of the longitudinal field near-infrared time series, from top to bottom EV Lac, DS Leo, and CN Leo. In each panel the rotation period corresponding to the highest peak is highlighted with a green dotted line, while two FAP levels (0.1% and 0.01%) are shown as grey horizontal lines. The window function of the entire time series is included and mirrored with respect to the x -axis (VanderPlas 2018) to highlight aliases due to the observation cadence and scheduling.

over time. A detail investigation will be performed with Zeeman-Doppler imaging in Sect. 6.

3.2. DS Leo

DS Leo is the least magnetically active star of our sample. The longitudinal field near-infrared measurements fall within $\pm 56 \text{ G}$

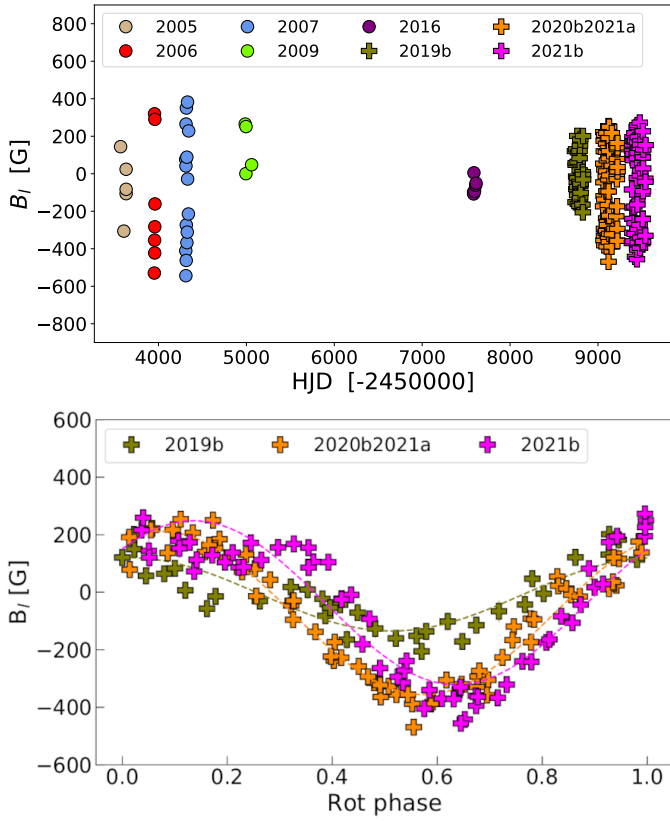


Fig. 3. Temporal evolution of the longitudinal magnetic field for EV Lac. The shape of the data points distinguishes optical (circles) from near-infrared (squares), and the colour represents the epoch in which the data were collected. Top: full time series of measurements with ESPaDOnS, NARVAL, and SPIRou. Bottom: phase-folded curves of SPIRou data points colour-coded by epoch; the associated least-squares sine fits are shown as dashed lines. The rotation period used is listed in Table 1.

with a median error bar of 7 G, whereas the optical ones range between -25 and 80 G, with a median error of 7 G (excluding a visible outlier at more than 150 G). The dispersion of the near-infrared data is comparable to the optical (20 G against 24 G) and there is a shift of the near-infrared mean towards zero by 16 G relative to the optical one. The phase-folded curves of the two epochs (2020b2021a and 2021b2022a) do not reveal particular changes, as the variations are both characterised by sinusoidal trends and similar amplitudes (see Fig. 4). The results do not change appreciably when a 4000 K synthetic mask is used against the 3500 K. There is a $\sim 40\%$ difference in Stokes I depth and amplitude of Stokes V between the two masks, which again cancels out in Eq. (4). The range of B_l values with the hotter mask is between -50 and 60 G with a median error bar of 8 G.

3.3. CN Leo

For CN Leo, the B_l measurements range from -630 to -240 G with a median error bar of 40 G, implying that we observe only the negative polarity of the large-scale field, similar to AD Leo (Bellotti et al. 2023b). These are compatible with the average B_l of -691 ± 54 G reported in Morin et al. (2010). The field values exhibit a sine-like oscillation of about 1000 d as well as fluctuations within each epoch. Although the scatter of the global and epoch-by-epoch time series is lower or compatible with the

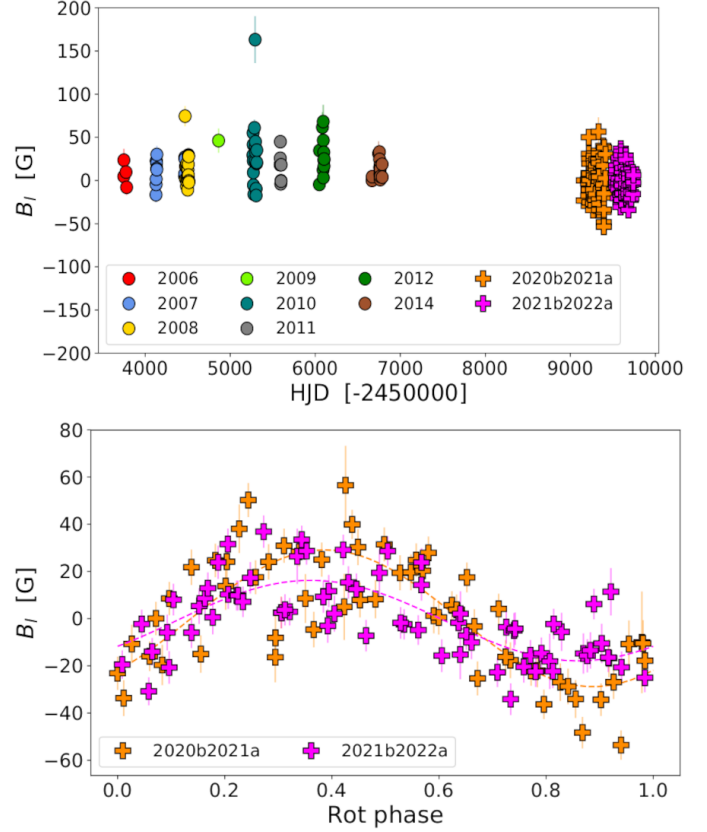


Fig. 4. Temporal evolution of the longitudinal magnetic field for DS Leo. The format is the same as in Fig. 3.

respective median error bar, which would make the oscillations dubious, the time series is dense, hence we are more sensitive to the epoch-to-epoch variability (see Fig. 5). If we bin the full time series with 50-d intervals, we are still able to capture a sinusoidal variation of 1000 d. When we phase-fold the four epochs at the stellar rotation period, we do not note any evident rotational modulation (the amplitude of the variations is consistent with zero within uncertainties), so we expect the field topology to be a dipole with negative polarity, and with the magnetic axis almost aligned with the rotation axis of the star.

4. FWHM of Stokes I

Since the Zeeman effect is proportional to Landé factor, modulus of the magnetic field (B), and the square of the spectral line wavelength, the width of Stokes I profiles computed in the near-infrared domain for stars with intense magnetic fields can be used as a proxy for Zeeman broadening measurements to first order (Donati et al. 2023a; Bellotti et al. 2023b). The value B encapsulates the magnetic field at both small and large scales, while the longitudinal field probes the large-scales only. Thus, the temporal analysis of the FWHM of Stokes I and its correlation to B_l can shed more light on the link between the two distinct spatial scales. In addition, the FWHM may exhibit a long-term evolution that correlates with the large-scale field evolution, as shown for AD Leo by Bellotti et al. (2023b).

The FWHM analysis can inform the design of activity-filtering techniques for radial velocity searches of exoplanets. Haywood et al. (2022) show that, for the Sun, the rotationally-modulated line broadening correlates with the azimuthal distribution of the small-scale magnetic flux, and Lienhard et al.

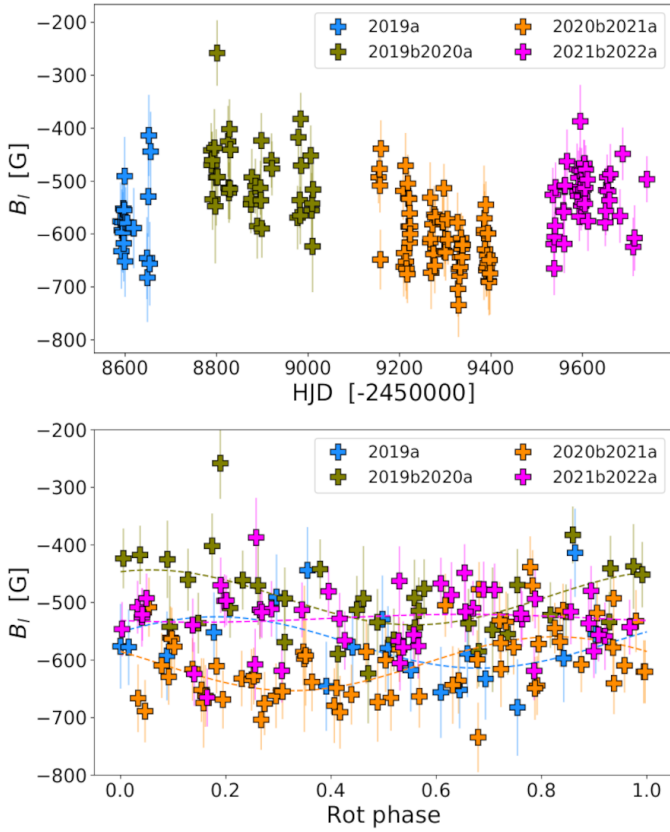


Fig. 5. Temporal evolution of the longitudinal magnetic field for CN Leo. The format is the same as in Fig. 3.

(2023) report the efficient activity-filtering in solar radial velocity time series using a novel proxy based on the total unsigned magnetic flux. For AU Mic Klein et al. (2021) report the correlation between the radial velocity and FWHM variations, when the latter were computed with magnetically sensitive lines. In Appendix B, we describe first-order computations of the unsigned magnetic field using the FWHM as a proxy.

Following Bellotti et al. (2023b), we applied LSD using magnetically sensitive ($g_{\text{eff}} > 1.2$) and weakly-sensitive ($g_{\text{eff}} < 1.2$) line masks. In the near-infrared domain, the masks contain 420 and 400 lines for the 3500 K case (EV Lac and DS Leo), respectively, and for the 3000 K case (CN Leo) they contain 280 and 300 lines. In optical, the masks contain 1650 and 1500 lines for the 3500 K case. In the following, the reference data set is the one obtained using the full mask, for either stellar temperature or wavelength domain. To compute the FWHM, we modelled the Stokes I LSD profiles with a combination of a Voigt and a linear model, the latter to account for residuals of continuum normalisation.

4.1. Rotational modulation and short-term variability

We used Eq. (3) to phase-fold the FWHM time series at each epoch and for both the full and high- g_{eff} masks. With the latter mask, Klein et al. (2021) show enhanced rotationally-modulated variations for AU Mic, whereas Bellotti et al. (2023b) do not report a modulation for near-infrared SPIRou observations of AD Leo, given the large dispersion of the data set. We proceeded in a similar manner to Bellotti et al. (2023b), and we fitted the observed FWHM values with a constant and a sine model at the

stellar rotation period. The analysis is summarised in Table 2 and illustrated in Fig. 6 for DS Leo and in Appendix B for EV Lac and CN Leo.

For EV Lac, the FWHM of Stokes I profiles from near-infrared observations does not exhibit evident rotational modulation (see Fig. B.2), since the change in reduced χ^2 between a constant and a sine model is only marginal. In some cases, like 2021b with high- g_{eff} lines, the χ_r^2 increases when using a sine model, but it is not statistically significant (Press et al. 1992). Only in 2020b2021a we observe a χ_r^2 improvement of about two when using the sine model for either of the chosen masks, and we correspondingly visualise a hint of rotational modulation, especially for the full mask. If we colour-code the high- g_{eff} data by rotational cycle, we do not observe any specific behaviour, as the dispersion over different cycles (and within an individual epoch) is comparable.

For the optical observations, the FWHM of EV Lac's Stokes I profiles manifests clear rotational modulation in 2006, 2007, and 2010 regardless of the mask employed (see Fig. B.2). A plausible explanation for observing rotational modulation in optical but not in near-infrared could be given by the larger contribution of the Zeeman effect in the latter domain. The distortions induced by the Zeeman effect on the line profile shape cannot be modelled effectively by a simple Voigt kernel, and act as a dispersive factor of the FWHM measurement. For this reason, the FWHM may lose its diagnostic power in the near-infrared for strong magnetic fields.

For DS Leo, in the SPIRou 2020b2021a epoch, the phase-folded data points vary with the stellar rotation, quantified by a decrease in χ^2 from 2.8 to 0.9 (for the default mask) and from 6.2 to 2.9 (for the high- g_{eff} mask) when using a sine model rather than a constant (see Fig. 6). The sine model for the default mask fits the data approximately down to noise level. In the SPIRou 2021b2022a epoch, there is no clear rotational modulation instead and the variations can be equivalently explained by a constant model. If present, the modulation is enhanced or quenched when high- g_{eff} or low- g_{eff} lines are adopted. Colour-coding the high- g_{eff} by cycle number reveals short-term variability, as distinct modulations for different rotational cycles can be extracted. This is more evident for 2020b2021a, as the variations of the data points appear 'stacked', that is, FWHM values belonging to different rotational cycles exhibit a vertical offset. This feature could be explained by the presence of differential rotation, since the shear would have displaced magnetic regions on the surface during the time span of our observations, making the cycle-averaged FWHM oscillate. The quantification of differential rotation will be investigated in Sect. 6.

For optical observations of DS Leo, we were able to capture the rotational modulation of the FWHM in most epochs (Fig. 6), especially when using magnetically sensitive lines. This supports our weak-field considerations, because the contribution of Zeeman effect to the line shape is less important for DS Leo both in near-infrared and in optical, compared to EV Lac and CN Leo.

For CN Leo, the FWHM of near-infrared profiles does not manifest rotational modulation, similar to EV Lac (see Fig. B.3), as the χ_r^2 associated with a constant and a sine model is marginally different. Colour-coding the data points by rotational cycle does not reveal any specific feature that could be associated to short-term variability. We observe an increased dispersion at phases larger than 0.5 for almost all epochs when using high- g_{eff} lines, which could bias the measurement of the average FWHM, and which we attributed to the magnetic field, since low- g_{eff} lines are approximately constant at all phases. For the optical, the limited number of observations

Table 2. Comparison of a constant line against a sine fit for the FWHM phase variations of EV Lac, DS Leo, and CN Leo.

Epoch	Mask	Mean [km s ⁻¹]	Mean error [km s ⁻¹]	STD [km s ⁻¹]	RMS _{const} [km s ⁻¹]	$\chi^2_{r,const}$	RMS _{sine} [km s ⁻¹]	$\chi^2_{r,sine}$
EV Lac								
2019b	Default	22	0.65	1.68	1.68	6.9	1.45	5.9
	$g_{\text{eff}} > 1.2$	29	1.12	4.39	4.39	19.7	4.17	19.7
2020b2021a	Default	21	0.44	1.00	1.00	6.2	0.82	4.4
	$g_{\text{eff}} > 1.2$	28	0.87	2.62	2.62	12.9	2.45	10.7
2021b	Default	21	0.46	0.98	0.98	4.8	0.90	4.5
	$g_{\text{eff}} > 1.2$	28	0.74	2.57	2.57	13.0	2.44	16.1
DS Leo								
2020b2021a	Default	13	0.18	0.29	0.29	2.8	0.16	0.9
	$g_{\text{eff}} > 1.2$	14	0.21	0.47	0.47	6.2	0.33	2.9
2021b2022a	Default	13	0.18	0.21	0.21	1.5	0.20	1.3
	$g_{\text{eff}} > 1.2$	14	0.20	0.32	0.32	3.1	0.30	2.7
CN Leo								
2019a	Default	15	0.34	1.27	1.27	16.7	1.22	19.7
	$g_{\text{eff}} > 1.2$	21	1.19	3.73	3.73	19.8	3.44	22.5
2019b2020a	Default	17	0.36	1.41	1.41	19.1	1.35	16.6
	$g_{\text{eff}} > 1.2$	25	1.57	4.44	4.44	15.3	4.27	13.6
2020b2021a	Default	16	0.37	1.69	1.69	45.8	1.61	39.8
	$g_{\text{eff}} > 1.2$	22	1.51	5.08	5.08	26.8	4.74	23.1
2021b2022a	Default	17	0.34	1.37	1.37	25.7	1.29	24.7
	$g_{\text{eff}} > 1.2$	22	1.41	4.94	4.94	16.3	4.65	15.8

Notes. The columns are: 1) subset of the time series, 2) line list used in LSD computation, 3) mean FWHM, 4) mean error bar, 5) standard deviation of the data sets, 6) RMS (root mean square) residual of a constant line fit equal to the average of the data set, 7) reduced χ^2 of a constant model, 8) RMS residual of a sine fit at the stellar rotation period, and 9) reduced χ^2 of a sine model.

(four) prevents us from performing a rotational modulation analysis.

4.2. Correlation between FWHM and B_l

The longitudinal magnetic field is a proxy for large-scale magnetic field, and the FWHM is a proxy for the small-scale field, so we inspected their correlations to yield more insights on the link between these two spatial scales. In particular, we computed Pearson correlation coefficients via 5000 bootstrap iterations. The values summarised in Table 3 correspond to the mean and standard deviation of the coefficient distribution. The analysis was carried out for the FWHM computed with the three masks: full, low- g_{eff} , and high- g_{eff} . The analysis is illustrated in Fig. 7 for optical observations of EV Lac and Fig. B.4 for optical and near-infrared observations of DS Leo. CN Leo was excluded because the FWHM from near-infrared lines is not modulated by rotation.

For EV Lac, there is a positive correlation for 2006 data, which increases when going from low- g_{eff} lines (Pearson $R = 0.19$) to high- g_{eff} lines (Pearson $R = 0.59$). This is the expected behaviour from the principle of Zeeman effect: the line profile is broader when the field is stronger. A positive correlation is also seen in 2007, but its strength does not vary according to the line mask adopted.

For DS Leo, we observe a variety of relations: there is a positive correlation that increases going from low- g_{eff} to high- g_{eff} lines in 2007 and 2011, whereas in 2012 and 2014, there is an anti-correlation that becomes stronger for low- g_{eff} lines. For 2008 and 2010, there is one outlying data point at large B_l values that likely biases the correlation coefficient, as the bulk of the data points does not manifest particular correlations. When looking at the SPIRou 2020b2021a epoch, we do not observe

significant correlation, the Pearson R coefficient being smaller than 0.2 for the three masks.

While not straightforward to interpret, these results altogether suggest an underlying complexity in the link between small- and large-scale field, which may not be encapsulated in a simple scaling. The variety of correlations for different epochs for DS Leo may stem from the fact that, for early M dwarfs, the ratio of magnetic field recovered with polarised light relative to unpolarised light is only a few percent (and it increases to dozens of percents for mid-M, [Reiners & Basri 2009](#); [Morin et al. 2010](#); [Kochukhov 2021](#)), hence there is an even less obvious scaling between small- and large-scale fields.

4.3. Long-term variations of FWHM

We inspected the long-term behaviour of the epoch-averaged FWHM of Stokes I , when computed with the full, high- g_{eff} , and low- g_{eff} line masks. For AD Leo, [Bellotti et al. \(2023b\)](#) show that the evolution of the epoch-averaged FWHM correlates with the secular trend of B_l and the magnetic flux measured by modelling the Zeeman broadening and intensification. The results for the stars examined are shown in Fig. 8.

For EV Lac, no clear trend is observed. In near-infrared, the average FWHM decreased from 22 to 21 km s⁻¹ for the full mask, while it was stable around 16 km s⁻¹ for the low- g_{eff} mask. For high- g_{eff} , there is a slight temporal decrease from 29 km s⁻¹ to just below 28 km s⁻¹. In optical, we observe the same slight oscillation when adopting the three line masks, around 14 km s⁻¹, above 12 km s⁻¹ and below 12 km s⁻¹ for the high- g_{eff} , full, and low- g_{eff} masks, respectively.

For DS Leo, the mean FWHM from near-infrared observations is 13 km s⁻¹, 14 km s⁻¹ and 11 km s⁻¹ for the full, high- g_{eff}

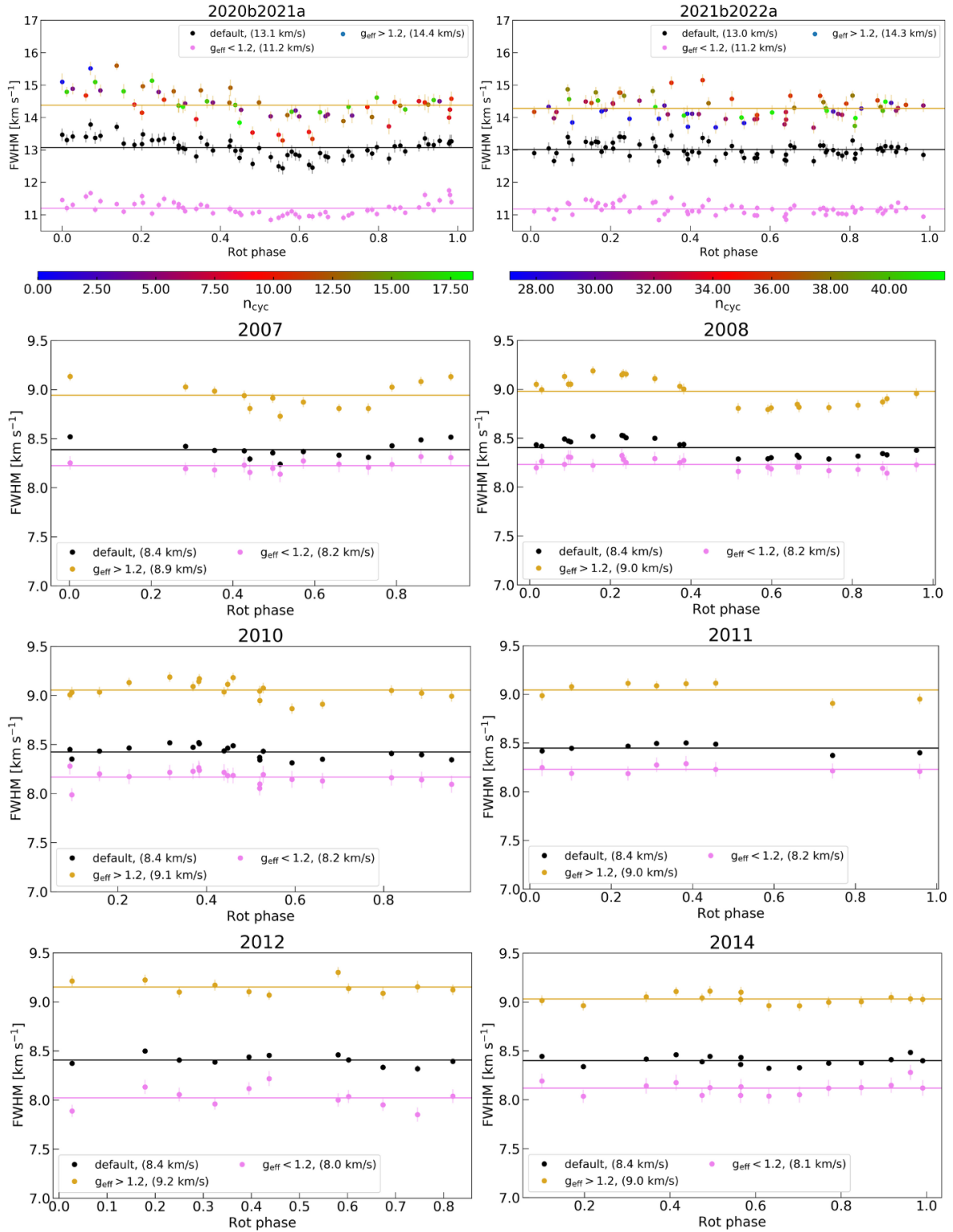


Fig. 6. Rotational modulation analysis of FWHM for DS Leo. The top two panels correspond to the near-infrared epochs (2020b2021a and 2021b2022a), whereas the remaining panels correspond to the optical epochs (2007, 2008, 2010, 2011, 2012, and 2014). In each panel are shown the phase-folded time series of FWHM computed with the full, low- g_{eff} , and high- g_{eff} mask with a horizontal line representing the mean FWHM value (also reported in each legend). For the near-infrared epochs the high- g_{eff} time series is colour-coded by rotational cycle to inspect signs of short-term variability. Observed stacked data points: observations within the first five cycles tend to fall at high FWHM values, then progressively at lower FWHM between cycle number 5 and 11, and at higher FWHM values again in the latest cycles.

and low- g_{eff} mask and for both epochs. In optical, the mean FWHM is stable around 8.0 km s^{-1} , 9.0 km s^{-1} and 8.4 km s^{-1} for the full, high- g_{eff} and low- g_{eff} masks. Therefore, we do

not observe a significant evolution. The same conclusion is reached when computing near-infrared LSD profiles with a 4000 K mask.

Table 3. Correlation coefficients between $|B_l|$ and FWHM of EV Lac and DS Leo, for the epochs in which we observed rotational modulation at the stellar rotation period.

Epoch	Full	High- g_{eff}	Low- g_{eff}
EV Lac			
2006	0.33 ± 0.39	0.49 ± 0.36	0.08 ± 0.48
2007	0.27 ± 0.29	0.30 ± 0.28	0.29 ± 0.30
DS Leo			
2007	0.24 ± 0.26	0.10 ± 0.29	0.34 ± 0.23
2008	-0.35 ± 0.15	-0.34 ± 0.15	-0.51 ± 0.12
2010	-0.07 ± 0.33	0.19 ± 0.24	-0.49 ± 0.42
2011	0.84 ± 0.12	0.86 ± 0.09	0.20 ± 0.28
2012	-0.51 ± 0.25	0.27 ± 0.29	-0.66 ± 0.18
2014	-0.38 ± 0.20	-0.15 ± 0.23	-0.55 ± 0.19
2020b2021a	0.09 ± 0.12	0.20 ± 0.12	-0.11 ± 0.11

Notes. The columns are: 1) subset of the time series, 2) average Pearson correlation coefficient from bootstrap analysis using the full LSD mask, 3) the high- g_{eff} mask, and 4) the low- g_{eff} mask.

For CN Leo, the low- g_{eff} lines are stable around 12 km s^{-1} , the full mask values evolve from 15 km s^{-1} to 17 km s^{-1} and then back to 16 km s^{-1} , while the high- g_{eff} mask values from 21 km s^{-1} to 25 km s^{-1} and back to 22 km s^{-1} . Such temporal variation is anti-correlated with the long-term sine oscillation of B_l (in absolute value), the average FWHM being largest when the B_l is smallest.

5. Principal component analysis

Lehmann & Donati (2022) presented a method based on principal component analysis (PCA) that reveals key properties of the stellar magnetic topology and its temporal evolution directly from the LSD Stokes V profiles, without prior assumptions about stellar parameters such as $v_{\text{eq}} \sin i$ and inclination. The PCA method provides information about the degree of axisymmetry, the poloidal-to-toroidal fraction of the axisymmetric field, the field complexity (i.e., dipolar or more complex topology), and the temporal evolution of these three parameters. Information about the axisymmetric field are captured by the mean Stokes V profile of the observed time series and information about the non-axisymmetric field in the mean-subtracted Stokes V profiles. The PCA method analyses the mean Stokes V profile to infer the degree of axisymmetry and whether the axisymmetric field is more poloidal or toroidal. Furthermore, by determining the eigenvectors and coefficients of the mean-subtracted Stokes V profiles using PCA, information about the field complexity and its evolution with time can be obtained. For more information about the PCA method see Lehmann & Donati (2022) and Lehmann et al. (2024).

We studied the near-infrared LSD Stokes V time series collected by SPIRou for EV Lac, DS Leo and CN Leo similar to our analysis for AD Leo (Bellotti et al. 2023b). As in Lehmann et al. (2024), we used the S/N-weighted mean profiles and the weighted PCA analysis (Delchambre 2015), as they provide better results for long time series with varying S/N.

5.1. EV Lac

The mean Stokes V profile of EV Lac is antisymmetric to the line centre, suggesting that the axisymmetric field is predominantly poloidal (see Fig. 9a), and begins to split at the line centre owing

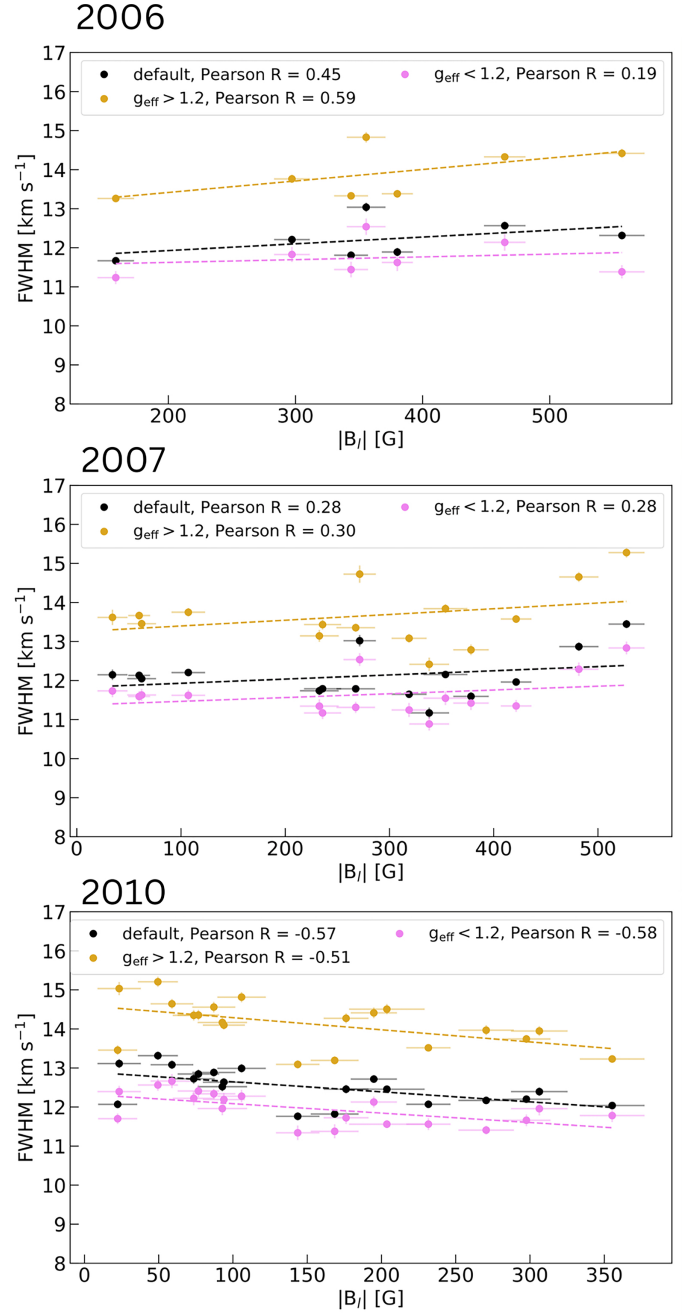


Fig. 7. Correlation analysis between FWHM and $|B_l|$ for EV Lac. The three panels correspond to the optical epochs in which rotational modulation is present: 2006, 2007, and 2010. In all panels the data points are colour-coded based on the line mask used for LSD: full (black), low- g_{eff} (purple), and high- g_{eff} (yellow).

to the strong magnetic field of EV Lac. The PCA method is based on the weak-field approximation valid for $B \ll 1 \text{ kG}$. For EV Lac the total unsigned magnetic field values are above this limit with 4.3 kG (Shulyak et al. 2017), which causes the visible splitting at line centre of the mean Stokes V profile. Therefore, we need to be cautious about our conclusions derived with the PCA method. This also applies for CN Leo which exhibits a total field value of $\sim 2.3 \text{ kG}$ (Shulyak et al. 2019), although we do not record a clear Stokes V splitting. As a double-check, we simulated the Stokes V profile using synthetic and observed magnetic field maps while artificially increasing or decreasing the magnetic field strength. Our simulations for the three stars of our

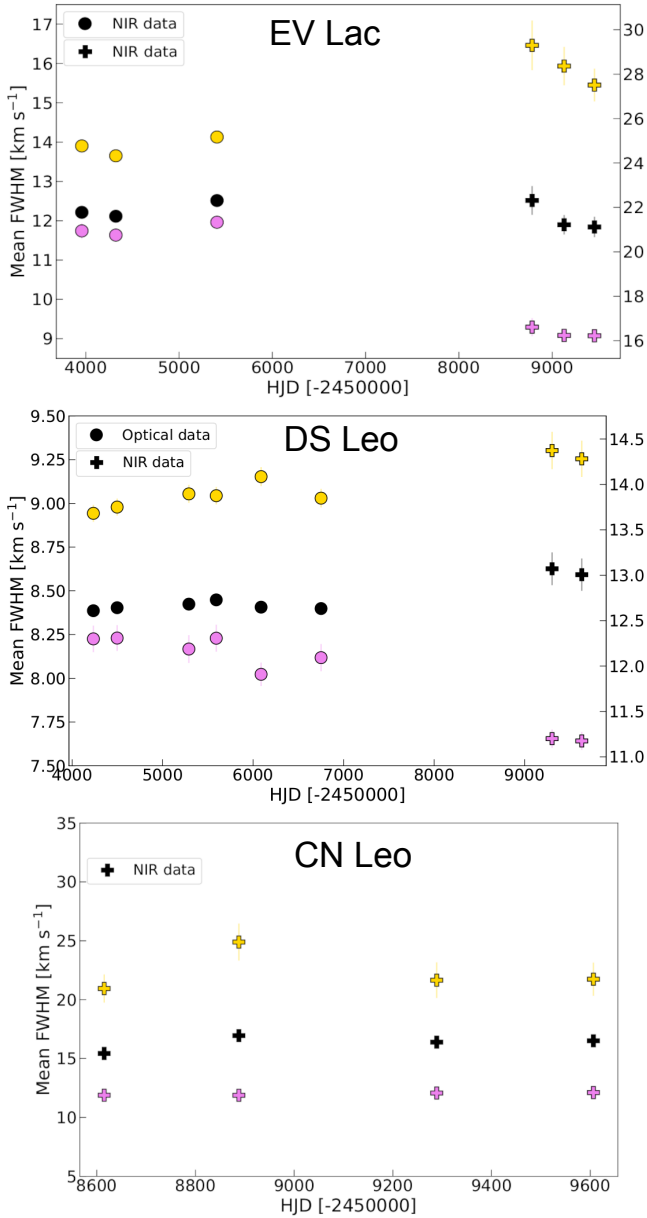


Fig. 8. Long-term evolution of the epoch-averaged FWHM. The panels show the results from optical (circles) and near-infrared (pluses) observations of EV Lac (top), DS Leo (middle), and CN Leo (bottom). In all panels, the data points are colour-coded based on the line mask used for LSD: full (black), low- g_{eff} (purple), and high- g_{eff} (yellow). The left y-axis refers to the optical observations, and the right y-axis to the near-infrared observations.

sample show that the conclusions derived with the PCA method remained valid for $B > 1$ kG in the case of EV Lac (and CN Leo), even if it is based on the weak-field approximation.

A signal is present in the first three eigenvectors of the PCA analysis of the mean-subtracted Stokes V profile capturing the information about the non-axisymmetric component of EV Lac’s topology, with the first two displaying an antisymmetric shape and the third a symmetric shape relative to the line centre (see Fig. 9b). The large number of eigenvectors containing a signal symbolises a non-axisymmetric field topology.

Figure 9c shows the per-epoch analysis of EV Lac for the Stokes V mean profile capturing the information of the axisymmetric field and the PCA coefficients of the first three eigenvec-

tors allowing the analysis of the non-axisymmetric field. The coefficients are derived from the weighted PCA of the mean-subtracted Stokes V time series using the weighted mean profile computed over all epochs (e.g., Fig. 9a), and not the weighted mean profile of each individual epoch (e.g., Fig. 9c left column). This because, in the latter case, the mean value of the coefficients would be centred for each epoch, and the amplitudes of the variations could not be compared between epochs.

We observe that the amplitude of the mean Stokes V profile increases from 2019b to 2020b/2021a. It remains antisymmetric with respect to the line centre for all epochs, which indicates a poloidal-dominated axisymmetric component for 2019b to 2021b. Since the amplitude of the coefficients also increases from 2019b to 2021a, we conclude that the field of EV Lac strengthens between 2019b and 2021a. The most complex phase variations of the coefficients occur in the first epoch 2019b, suggesting that the topology of EV Lac has the lowest dipole fraction and therefore is most complex in 2019b. Somehow opposite is the second epoch 2020b/2021a: the coefficients show sinusoidal curves for all three eigenvectors, reflecting a tilted, dipole-dominated topology. In the last epoch 2021b, the coefficients still show a sinusoidal trend, but become slightly more flat between rotational phase 0.0–0.3.

5.2. DS Leo

Figure C.1 shows the PCA analysis for DS Leo. The mean profile reflecting the axisymmetric component of the topology is mainly symmetric to the line centre, indicating a significant toroidal field fraction ($>5\%$) of the axisymmetric field, see Fig. C.1a. The PCA analysis of the mean-subtracted profiles allows the analysis of the non-axisymmetric component. Two eigenvectors emerge from the noise, one antisymmetric and one symmetric, indicating a non-axisymmetric topology. The degree of axisymmetry is however larger than EV Lac’s, as fewer eigenvectors show a signal (see Fig. C.1b).

The per-epoch analysis shows a decrease in amplitude of the mean Stokes V profile, as well as of the phase variations of the coefficients, indicating a weakening of the magnetic field from the first to the second epoch. For both epochs, the coefficient of the first eigenvector exhibits the typical sinusoidal trend of a tilted dipole, and the pointing phase of the dipole appears to be stable. The coefficient of the second eigenvector manifests a more complex trend that evolves from 2020b/2021a to 2021b/2022a. This reflects the evolution of other magnetic field features in addition to the tilted dipole. We clearly see that the coefficients also vary within the epochs, implying that the magnetic field of DS Leo evolves on the timescale of its rotation period, as already suggested by Lehmann & Donati (2022) in their analysis of the 2008 optical observations of DS Leo.

5.3. CN Leo

CN Leo exhibits a strong and antisymmetric Stokes V mean profile, indicating a predominantly poloidal axisymmetric field, as illustrated in Fig. C.2a. The first eigenvector is antisymmetric and there is evidence for a second, symmetric eigenvector, albeit the larger noise (Fig. C.2b). This suggests that CN Leo is the most axisymmetric M dwarf of our sample.

The per-epoch Stokes V mean profiles show a varying amplitude, together with the amplitude of the rotational modulation of the coefficients, which could be due to variability in either field strength or axisymmetry (see Fig. C.2c). The first epoch 2019a appears to be highly axisymmetric, as the coefficients cluster around zero. The second epoch 2019b/2020a has a clear

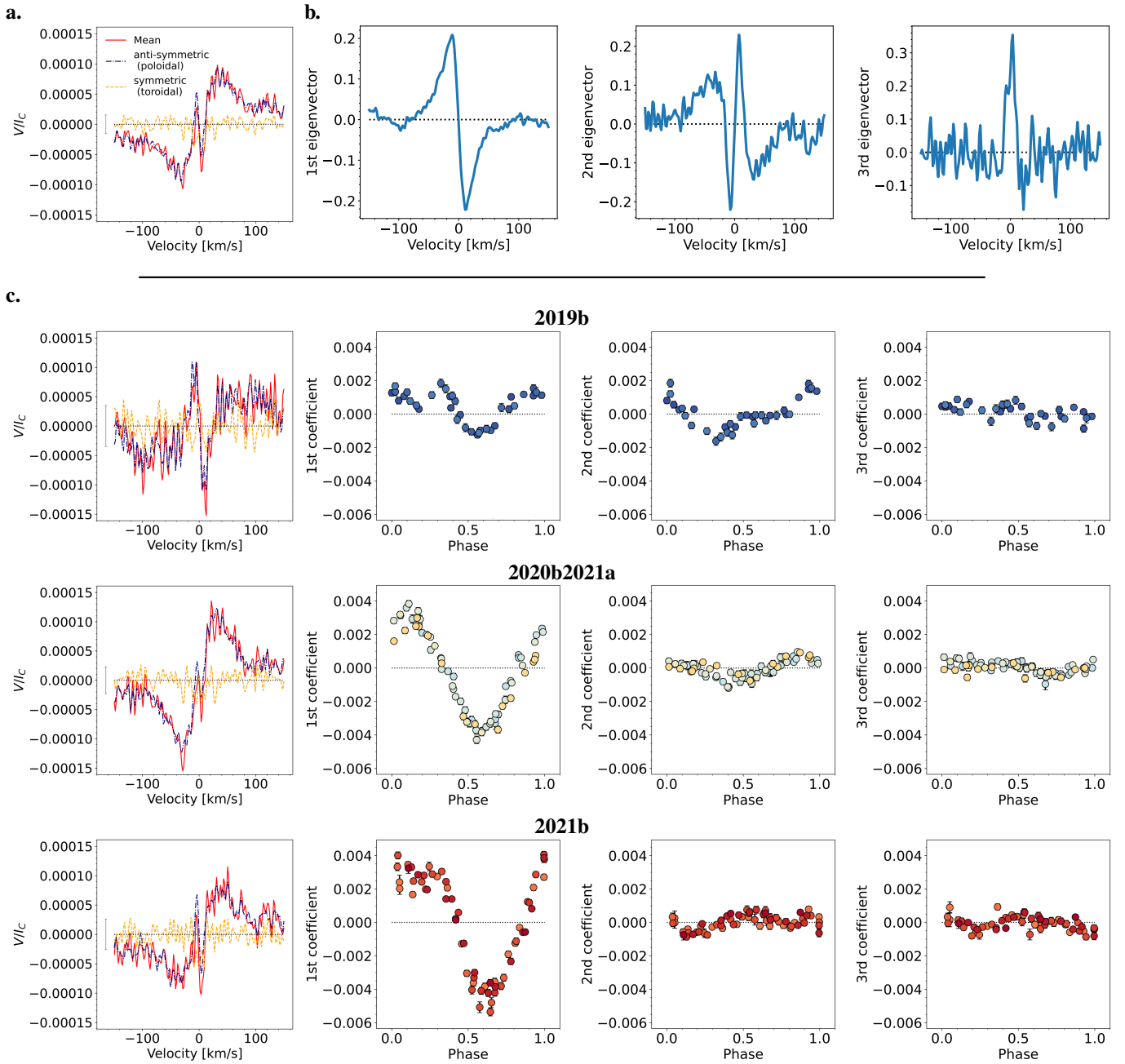


Fig. 9. PCA analysis for EV Lac. (a) Mean profile (red) for all observations and its decomposition in the antisymmetric (blue dashed) and symmetric (yellow dotted) component (with respect to the line centre) related to the poloidal and toroidal axisymmetric field, respectively. (b) First three eigenvectors of the mean-subtracted Stokes V profiles. (c) Mean profile (left column), and the coefficients of the first three eigenvectors (three columns to the right) for each season (one season per row). The mean profiles of the individual seasons are plotted in the same format as in panel a. The coefficients are colour-coded by rotation cycle.

sinusoidal variation in the coefficients of the first eigenvector, implying a larger tilt angle of the dipole relative to the other epochs, and the mean of the coefficients is offset towards positive values. The third epoch 2020b2021a is characterised by a less clear sinusoidal variation in the coefficients, with their mean offset towards negative values. The fourth epoch 2021b2022a resemble the first one, with the mean of the coefficients around zero.

6. Magnetic imaging

We applied Zeeman-Doppler imaging to reconstruct the large-scale magnetic field at the surface of EV Lac, DS Leo and

CN Leo. The magnetic geometry is described as the sum of a poloidal and a toroidal component, which are both expressed through spherical harmonics decomposition. In particular, we employed the formalism outlined in [Lehmann & Donati \(2022\)](#). The algorithm proceeds iteratively, by synthesising Stokes V profiles and comparing them with the observations, in order to fit the spherical harmonics coefficients $\alpha_{\ell,m}$, $\beta_{\ell,m}$, and $\gamma_{\ell,m}$ (with ℓ and m the degree and order of the mode, respectively), until a maximum-entropy solution at a fixed reduced χ^2 is reached ([Skilling & Bryan 1984](#); [Semel 1989](#); [Donati & Brown 1997](#)). We employed the `zdi.py` code described in [Folsom et al. \(2018\)](#), and which was

implemented by Bellotti et al. (2023b) to incorporate the Unno-Rachkovsky's solutions to polarised radiative transfer equations in a Milne-Eddington atmosphere (Unno 1956; Rachkovsky 1967; Landi Degl'Innocenti & Landolfi 2004) and the filling factor formalism adopted by Morin et al. (2008).

The filling factors f_I and f_V represent the fraction of the cell of the stellar surface grid covered by magnetic regions and magnetic regions producing net circular polarisation, respectively (Morin et al. 2008; Kochukhov 2021). With the inclusion of f_V , we assume that the polarisation signal comes from a multitude of magnetic spots whose local field strength is B/f_V distributed following a certain large-scale structure such that the magnetic field modulus averaged over a grid cell is equal to B . In practice, using f_V enables us to reproduce the amplitude (scaling with the magnetic field B) and the Zeeman splitting (scaling with B/f_V) observed for Stokes V LSD profiles. The values of filling factors are assumed constant throughout the stellar surface grid.

The Unno-Rachkovsky models of the local line profiles (for both Stokes I and V) are described by the following parameters (del Toro Iniesta 2003; Landi Degl'Innocenti & Landolfi 2004): the Gaussian width (w_G , related to thermal broadening), the Lorentzian width (w_L , related to pressure broadening), the ratio of the line to continuum absorption coefficients (η_0), and the slope of the source function in the Milne-Eddington atmosphere (β). Before applying ZDI, and for each epoch of our three stars, we perform a parameter optimisation based on a χ^2 minimisation approach. In practice, we generate a series of synthetic Stokes I profiles for a grid of parameters, and compare them with the median observed Stokes I for a specific epoch, until a minimum χ^2 is found. The parameters corresponding to the χ^2 minimum are then used for the ZDI reconstruction. For EV Lac, we used $w_G = 0.1 \text{ km s}^{-1}$, $w_L = 12.0 \text{ km s}^{-1}$, and $\eta_0 = 9.8$, for DS Leo, we used $w_G = 0.5 \text{ km s}^{-1}$, $w_L = 4.4 \text{ km s}^{-1}$, and $\eta_0 = 17.0$, and for CN Leo, we used $w_G = 0.5 \text{ km s}^{-1}$, $w_L = 10.0 \text{ km s}^{-1}$, and $\eta_0 = 9.5$. The value of β is derived considering that, for a Milne-Eddington atmosphere, the local continuum flux relative to the flux at disc centre is

$$I_c/I_c^0 = (1 + \beta \cos \theta)/(1 + \beta), \quad (5)$$

where θ is the angle between the line of sight and stellar surface normal (Landi Degl'Innocenti & Landolfi 2004). A standard linear limb darkening law is given, for instance, by

$$I_c/I_c^0 = 1 - \eta + \eta \cos \theta, \quad (6)$$

where η is the limb darkening coefficient (Gray 2005). From Eqs. (5) and (6), we derive

$$\beta = \eta/(1 - \eta). \quad (7)$$

In our case, we adopted a linear limb darkening coefficient in H band of 0.2 (Claret & Bloemen 2011), hence β is consistently fixed to 0.25 in all ZDI reconstructions (for more details, see Erba et al. 2024).

Once the line parameters were fixed, we searched for the optimised value of filling factor f_V for each epoch of our stars. The procedure is similar to an optimisation of stellar parameters or differential rotation search (see Petit et al. 2002). We run ZDI for a grid of f_V values between 1.0% and 100%, and we recorded the χ^2 reached by ZDI each time. The χ^2 distribution is fit with a parabola around the minimum, and the value of f_V corresponding to the minimum χ^2 represents the optimal value. The 1σ error bars on f_V are determined as the $\Delta\chi^2 = 1$ variation away from the χ^2 minimum (Press et al. 1992).

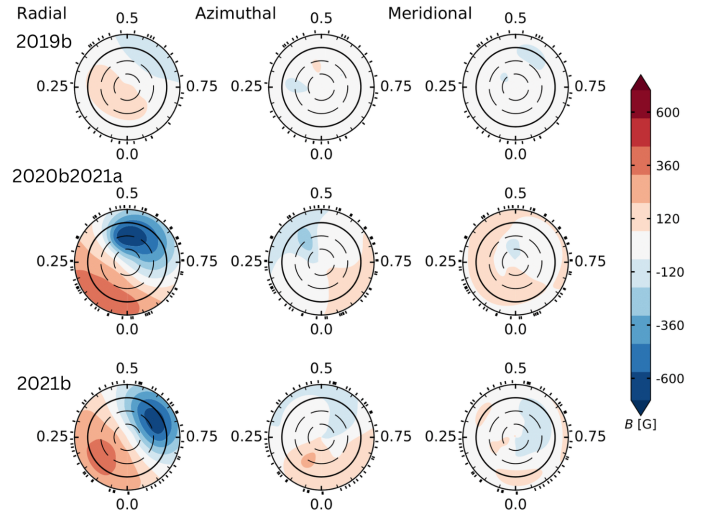


Fig. 10. Reconstructed ZDI maps in flattened polar view of EV Lac for (from left to right) 2019b, 2020b2021a, and 2021b. In each column the radial (top), azimuthal (middle), and meridional (bottom) components of the magnetic field vector are displayed. The radial ticks are located at the rotational phases when the observations were collected, while the concentric circles represent different stellar latitudes: $+30^\circ$ and $+60^\circ$ (dashed lines), and equator (solid line). The colour bar range is set by the maximum (in absolute value) of the magnetic field and illustrates the positive (red) and negative (blue) magnetic polarity for each epoch.

Finally, the maximum degree of the harmonic expansion was set to $\ell_{\max} = 8$ for all stars, consistently with the spatial resolution dictated by $v_{\text{eq}} \sin i$ and previous ZDI reconstructions (Morin et al. 2008; Hébrard et al. 2016). We note that only the modes with ℓ up to three have the most significant contribution in the reconstructed field maps. We did not observe appreciable differences in the ZDI reconstructions for filling factor f_I between 0.0 and up to 0.5 in some cases, hence we fixed it to $f_I = 0.0$.

We summarise the properties of all the magnetic field reconstructions in Table 4. The obliquity refers to the colatitude of the maximum of the dipolar component. It is obtained by first computing the poloidal-dipolar component of the field using the α_{lm} coefficient, and then by locating the colatitude associated with the maximum.

6.1. EV Lac

The optical maps of EV Lac were reconstructed by Morin et al. (2008) using the 2006 and 2007 data collected with ESPaDOnS and Narval. They found a strong ($B_{\text{mean}} = 500 \text{ G}$), non-axisymmetric, mostly dipolar field, composed mainly by two magnetic spots of distinct polarity at opposite longitudes. They were able to constrain a differential rotation rate of 1.7 mrad d^{-1} which was consistent with solid body rotation within 3σ .

To carry out tomographic inversion for EV Lac near-infrared SPIRou data, we assumed $i = 60^\circ$, $v_{\text{eq}} \sin i = 4.0 \text{ km s}^{-1}$, $P_{\text{rot}} = 4.36 \text{ d}$, and solid body rotation (Morin et al. 2008). The Stokes V time series is shown in Fig. D.1. The profiles are fitted down to a χ_r^2 level of 0.9, 1.2, and 1.4 from an initial value of 1.2, 5.0, and 6.5 for 2019b, 2020b2021a, and 2021b, respectively.

We constrained the filling factor f_V to 9% and 19% for 2020b2021a and 2021b, while we could not for 2019b, hence we set it to 100%. The typical error bar on f_V is at most 1%. Using either 9% or 19% on 2019b has only marginal effects on the map and the magnetic energy repartition, and the same level

of χ^2 is achieved. This could result from a lower effective S/N at this epoch, which prevents us from reliably constraining f_V . The fact that we can fix $f_V = 100\%$ for this epoch means that modelling the horizontal splitting of the Stokes V lobes is not necessary, and weak-field approximation could be equivalently assumed.

For the two remaining epochs, it is not straightforward to claim an evolution of the small-scale features represented by a change in f_V from 9% to 19%. If we set f_V to the median value of the two epochs (i.e., 14%), we observe only slight differences in the reconstructed maps: the field is more axisymmetric (an additional 4%) and in 2020b2021a the field is also more octupolar (additional 4%). While still limited, a variation of f_V has more impact on 2020b2021a than 2021b because of the stronger constraint on f_V in the former epoch.

The maps of the magnetic field and their characteristics are shown in Fig. 10 and Table 4. In all epochs, most of the magnetic energy is stored in the poloidal (>99%) and dipolar (>65%) components, with a substantial contribution from the quadrupolar modes (>10%). The field is non-axisymmetric, and the axisymmetric energy fraction decreases over time from 25% to 2%. Likewise, the obliquity of the field increases from 50° to 87° . The average magnetic field strength for the 2019b epoch is lower than the two other epochs. Considering that the Stokes V models of the 2019b epoch does not fully reproduce the amplitude of the LSD profiles, the magnetic field strength is likely underestimated. A differential rotation search on the SPIRou time series was inconclusive.

6.2. DS Leo

The large-scale magnetic field map for DS Leo was reconstructed initially by Donati et al. (2008) using Narval data collected in 2007 and 2008. They obtained a predominantly toroidal field geometry encircling the star, whereas the poloidal component was mainly dipolar. The average field strength was 100 G, and the axisymmetry of the poloidal component decreased between 2007 and 2008. Later, Hébrard et al. (2016) applied ZDI to HARPS-Pol and Narval observations collected in 2014, and consistently found a mostly-toroidal, axisymmetric geometry, with the poloidal component accounting for less than half the magnetic energy and mostly dipolar. Compared to the previous reconstructions, the average field strength decreased down to 80 G and the dipolar component increased from 50% to 88%, already suggesting a rapidly evolving magnetic field. There are two Narval epochs with unpublished data, namely 2010 and 2012, for which we recovered the magnetic field map in this work, as outlined in Appendix A.

We reconstructed the large-scale magnetic field for the 2020b2021a and 2021b2022a SPIRou epochs. The input parameters are $i = 60^\circ$, $v_{\text{eq}} \sin i = 2 \text{ km s}^{-1}$ (Hébrard et al. 2016), $P_{\text{rot}} = 13.91 \text{ d}$, and we initially postulated solid body rotation. The time series of Stokes V profiles for the two epochs is shown in Appendix D. The profiles were fitted to a χ_r^2 level of 1.4 and 1.2 from an initial value of 2.7 and 1.6 for 2020b2021a and 2021b2022a, respectively. We also constrained f_V values of 10% and 6% for the two epochs (with error bars of 1%).

We searched for differential rotation using the method of Donati et al. (2000) and Petit et al. (2002). Basically, we fixed the entropy at a certain value and inspected a dense grid of $(P_{\text{rot,eq}}, d\Omega)$ pairs to find the combination that minimises the χ_r^2 between observations and synthetic models, as illustrated in Fig. 11. The best parameters are measured by fitting a 2D paraboloid to the χ^2 distribution, and the error bars are obtained

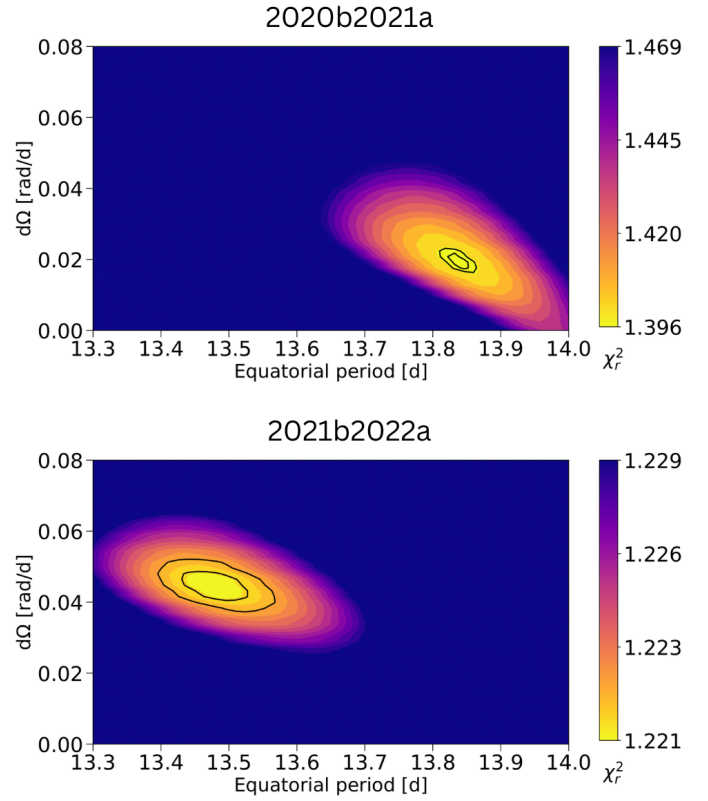


Fig. 11. Differential rotation search for DS Leo. Top: 2020b2021a. Bottom: 2021b2022a. The plots show the χ_r^2 landscape over a grid of $(P_{\text{rot,eq}}, d\Omega)$ pairs, with the 1σ and 3σ contours. The best values are obtained by fitting a 2D paraboloid around the minimum, while their error bars are estimated from the projection of the 1σ contour on the respective axis (Press et al. 1992).

from a variation of $\Delta\chi^2 = 1$ away from the minimum (Press et al. 1992; Petit et al. 2002). Differential rotation is implemented in `zdiipy` with the following equation

$$\Omega(\theta) = \Omega_{\text{eq}} - d\Omega \sin^2(\theta) \quad (8)$$

with $\Omega(\theta)$ the rotation frequency at colatitude θ , Ω_{eq} the rotation frequency at equator, and $d\Omega$ the differential rotation rate (Folsom et al. 2018).

We found $P_{\text{rot,eq}} = 13.836 \pm 0.016 \text{ d}$ and $d\Omega = 0.0192 \pm 0.0020 \text{ rad d}^{-1}$ for 2020b2021a, implying a rotation period at the pole of $14.447 \pm 0.069 \text{ d}$ (see Eq. (8)). For 2021b2022a, we obtained $P_{\text{rot,eq}} = 13.469 \pm 0.054 \text{ d}$ and $d\Omega = 0.0448 \pm 0.0045 \text{ rad d}^{-1}$, and the rotation period at the pole was $14.899 \pm 0.172 \text{ d}$. Assuming the $(P_{\text{rot,eq}}, d\Omega)$ pairs as input parameters for ZDI, the Stokes V fit is improved down to a χ_r^2 level of 1.25 and 1.10 for 2020b2021a and 2021b2022a, respectively. Finally, the inverse of the differential rotation rate represents the pole-equator lap time ($t_{\text{lap}} = 2\pi/d\Omega$). For 2020b2021a (time span of 256 d) and 2021b2022a (time span of 205 d) respectively, we obtained a t_{lap} of $327 \pm 34 \text{ d}$ and $140 \pm 14 \text{ d}$. During this time, magnetic regions on the surface are presumably distorted by the shear of differential rotation. The short-term variability emerging from the SPIRou time series of FWHM values (see Fig. 6) can be attributed to differential rotation since the equator-pole lap time is comparable to the time span of the epochs considered, meaning that differential rotation could have shifted the magnetic regions on the surface affecting the mean level of FWHM for that specific cycle.

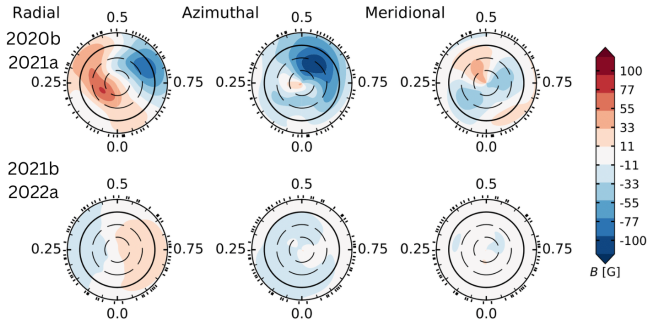


Fig. 12. Reconstructed ZDI maps in flattened polar view of DS Leo. Left: 2020b2021a. Right: 2021b2022a. The maps account for the constrained differential rotation. The format is the same as in Fig. 10.

We obtained tighter constraints on $d\Omega$ for 2020b2021a relative to 2021b2022a because the field is less complex in the second epoch, that is to say it is characterised by a lower number of magnetic features tracking differential rotation. Besides, the error bars are smaller than the literature measurements because our time series contained a larger number of observations (Donati et al. 2008; Hébrard et al. 2016). In general, the error bars on the differential rotation parameters are only statistical and do not account for systematics, hence they are likely underestimated. The values of equator/pole period encompass our measurement obtained from the periodogram analysis of B_l , and fall within the range of literature values (Donati et al. 2008; Hébrard et al. 2016). Our $d\Omega$ values are generally lower than estimated in the literature, but compatible within 3σ from Donati et al. (2008), and 1σ from Hébrard et al. (2016). Such difference could be due to an evolution of the shear at the surface of the star, as studied also by Donati et al. (2023a) for AU Mic, but deciphering the exact mechanism is not a straightforward task. Figure 11 also shows that there is an anti-correlation between $P_{\text{rot,eq}}$ and $d\Omega$ (or equivalently an $\Omega_{\text{eq}}-d\Omega$ correlation), likely due to the fact that we mainly trace one latitude when searching for differential rotation.

The maps are shown in Fig. 12 and their properties are reported in Table 4. In 2020b2021a, the magnetic energy is distributed almost equally in poloidal and toroidal components, with the dipolar mode accounting for most of the energy (64%). While the toroidal component is mostly axisymmetric (90%), the poloidal component is largely non-axisymmetric (4%). In 2021b2022a, the poloidal component takes over the toroidal one, counting 73% of the magnetic energy against 26%. The dipolar mode remains the dominant one (83%), featuring a moderate increase similarly to the one reported in Hébrard et al. (2016). In terms of axisymmetry, the toroidal component is stable, while the poloidal one increases from 4% to 9%. Between the two epochs, the average field strength decreased from 44 to 18 G.

6.3. CN Leo

There is no reconstruction of the magnetic field in the literature for this star. From four spectropolarimetric observations, Morin et al. (2010) detected strong Zeeman signatures corresponding to longitudinal fields of 600 G (as large as the maximum of EV Lac). The shape of Stokes V profiles and the absence of intermittency in the amplitude of the profiles suggested an axisymmetric, poloidal dipole.

From the rotation period $P_{\text{rot}} = 2.70 \pm 0.01$ d we measured (see Sect. 3) and the equatorial projected velocity $v_{\text{eq}} \sin i =$

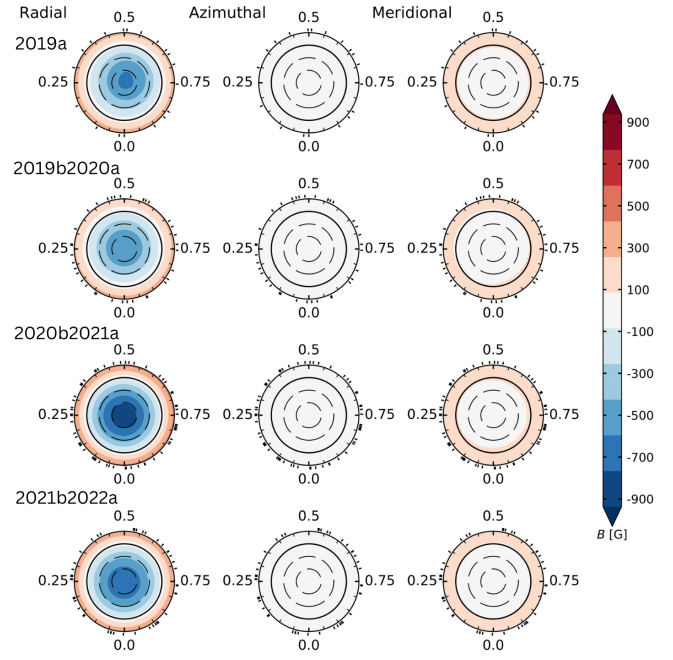


Fig. 13. Reconstructed ZDI maps in flattened polar view of CN Leo. From left to right: 2019a, 2019b2020a, 2020b2021a, and 2021b2022a. The format is the same as in Fig. 10.

2 ± 1 km s $^{-1}$ estimated by Cristofari et al. (2023), we obtained $R \sin i = P_{\text{rot}} v_{\text{eq}} \sin i / 50.59 = 0.107 \pm 0.053 R_{\odot}$, where the denominator accounts for the unit conversion of the variables involved. Considering the radius measurement for CN Leo by Rabus et al. (2019) of $R = 0.151 \pm 0.005 R_{\odot}$, we infer an inclination of $i = 45 \pm 20^{\circ}$.

The reconstruction of the large-scale magnetic field at the surface of CN Leo was performed for the 2019a, 2019b2020a, 2020b2021a and 2021b2022a epochs. The input parameters are $i = 45^{\circ}$, $v_{\text{eq}} \sin i = 2.0$ km s $^{-1}$, $P_{\text{rot}} = 2.7$ d, and solid body rotation.

The profiles were fitted to a χ^2_r level of 0.9, 1.0, 1.2, and 1.2 from an initial value of 2.9, 3.5, 6.8, and 6.7 for 2019a, 2019b2020a, 2020b2021a, and 2021b2022a, respectively. The f_V values were constrained to be 16%, 13%, 19% and 16% for the same epochs, with an error bar of 1%. The Stokes V time series is shown in Appendix D.

The maps of the magnetic field and their characteristics are shown in Fig. 13 and Table 4. In all epochs, most of the magnetic energy is stored in the poloidal (>99%), dipolar (>99%) and axisymmetric (>99%) components, without any significant variation over time. The field strength follows the sine-like long-term oscillation exhibited by B_l , meaning that it starts from an average field of 350 G, it decreases to 320 G, then increases to 490 G and finally decreases to 420 G.

6.4. Summary of the ZDI reconstructions

The evolution of the large-scale magnetic field for EV Lac, DS Leo, and CN Leo is summarised in Fig. 14. For completeness, we also included the evolution of AD Leo as reconstructed by Bellotti et al. (2023b), which sees a decrease of field strength accompanied by an increase of the obliquity of the magnetic field axis.

For EV Lac, the magnetic topology was found to be predominantly non-axisymmetric using optical data

Table 4. Properties of the magnetic map for EV Lac, DS Leo, and CN Leo, reconstructed from different epochs of SPIRou near-infrared time series.

	EV Lac			DS Leo			CN Leo			
	2019b	2020b2021a	2021b	2020b2021a	2021b2022a	2019a	2019b2020a	2020b2021a	2021b2022a	
f_V [%]	...	9	19	10	6	15	12	18	15	
B_{mean} [G]	72.5	297.7	265.1	44.3	17.9	350.2	321.8	486.9	420.1	
B_{max} [G]	175.8	700.0	690.5	115.2	34.9	650.4	607.8	937.6	820.9	
B_{pol} [%]	99.1	99.7	99.2	55.9	72.9	99.9	99.9	99.9	99.9	
B_{tor} [%]	0.9	0.3	0.8	44.1	27.0	0.1	0.1	0.1	0.1	
B_{dip} [%]	63.1	88.7	82.8	64.0	83.2	99.4	99.4	99.3	99.2	
B_{quad} [%]	25.4	9.4	14.6	28.5	13.1	0.5	0.6	0.6	0.7	
B_{oct} [%]	10.2	1.3	2.4	3.9	2.6	0.0	0.0	0.1	0.1	
B_{axisym} [%]	25.1	12.1	1.8	39.4	30.6	99.5	99.6	99.9	99.9	
$B_{\text{axisym,pol}}$ [%]	24.6	12.0	1.2	3.9	9.2	99.5	99.6	99.9	99.9	
Obliquity [°]	50.5	68.5	86.5	75.5	69.5	4.5	3.5	1.5	1.5	

Notes. The following quantities are listed: filling factor on Stokes V ; mean magnetic strength; maximum magnetic strength; poloidal and toroidal magnetic energy as a fraction of the total energy; dipolar, quadrupolar and octupolar magnetic energy as a fraction of the poloidal energy; axisymmetric magnetic energy as a fraction of the total energy; and obliquity of the dipolar component relative to the rotation axis. To compute the local magnetic field (i.e., within a grid cell of the ZDI stellar model) the field strength should be divided by the associated filling factor f_V .

(Morin et al. 2008), and we observed an even less axisymmetric field from SPIRou data, with the negative pole of the dipolar component lying approximately at equator. From the SPIRou observations, we also noted a rise in field strength from 57 G in 2019b to around 200 G in 2020b2021a and 2021b, following a similar evolution with respect to B_l .

For DS Leo, the poloidal component saw a progressive increase with respect to the toroidal one (from 20 to 70% of the total magnetic energy), and it remained highly non-axisymmetric throughout (Donati et al. 2008; Hébrard et al. 2016). The complexity of the poloidal component of the field has also decreased in the same timescale, since the field is predominantly dipolar. Moreover, the average reconstructed field strength has reduced, from an initial 100 G in 2007 to 15 G in the 2021b2022a SPIRou epoch. The panel of DS Leo in Fig. 14 includes two field topologies, in 2010 and 2012, which we reconstructed using unpublished Narval data (see Appendix A).

For CN Leo, there is no substantial evolution in four years, the topology being mainly poloidal, dipolar and axisymmetric. The only feature is a varying field strength, whose oscillations correlate with the longitudinal field evolution (in absolute value).

Similarly to what reported by Bellotti et al. (2023b), we caution that the field strength reported may be underestimated, owing to the limitation of the ZDI model at reproducing the shape of the Stokes V lobes (see e.g., Fig. D.1). The near-infrared Stokes V profiles manifest evident noise that is not rotationally modulated, and which prevents the ZDI model to capture all the information present in the profile.

To describe the magnetic field vector, we employed the formalism of Lehmann & Donati (2022), which sees the substitution of β_{lm} with $\alpha_{lm} + \beta_{lm}$ in the spherical harmonics equations. The main effect of using the latter is to change the appearance of the meridional and azimuthal magnetic field maps, making them resemble the radial field map, and avoid unnecessary large values of β_{lm} . If we use the standard formalism (see e.g., Donati et al. 2006b) with α_{lm} and β_{lm} disjointed, the reconstructed maps of EV Lac vary less than 3% in poloidal energy fraction, less than 5% in dipolar, quadrupolar, and octupolar components, and less than 2% in axisymmetric fraction. The average field strength decreases by at most 100 G. For CN Leo, the variations are similar or lower. This is in agreement with what was previously

found also for AD Leo (see appendix of Bellotti 2023). Overall, the properties of the magnetic topology and its long-term evolution are reconstructed consistently adopting either of the two spherical harmonics formalisms.

7. Discussion and conclusions

In this work we presented the long-term spectropolarimetric monitoring of three well-studied, active M dwarfs: EV Lac, DS Leo, and CN Leo. We used archival optical data collected with ESPaDOnS and Narval, as well as near-infrared SPIRou data obtained as part of the Legacy Survey between 2019 and 2022. We carried out distinct analyses to capture the evolution of the magnetic field, employing the longitudinal field as a proxy of the large-scale field component and the FWHM of Stokes I LSD profiles as a proxy for the small-scale component. We analysed qualitatively the secular evolution of the large-scale magnetic field via principal component analysis and reconstructed its topology by means of Zeeman-Doppler imaging.

We found different trends in the magnetic field behaviour, potentially hinting at a variety of magnetic cycles. Our conclusions are the following:

1. The longitudinal magnetic field analysis showed a pulsating trend for EV Lac with variations between ± 400 G around 2007, then between ± 200 G in 2016, and finally between ± 300 G in 2020. However, the dearth of observations between 2010 and 2019 prevent us from drawing firm conclusions on this behaviour. DS Leo did not manifest any specific trend as the mean field remained reasonably stable around 0 G, and the measurements within ± 50 G. CN Leo exhibited a sine-like trend, characterised by a period of 2.7 yr, an amplitude of 100 G, and an average of -500 G.
2. We observed rotational modulation of the FWHM of Stokes I for optical observations of EV Lac and DS Leo, and near-infrared observations of DS Leo, likely stemming from distinct contributions of the Zeeman effect in the two wavelength domains. The FWHM of near-infrared line profiles for stars with intense magnetic fields is expected to be more impacted than at optical wavelengths, resulting in larger scatter in the time series.

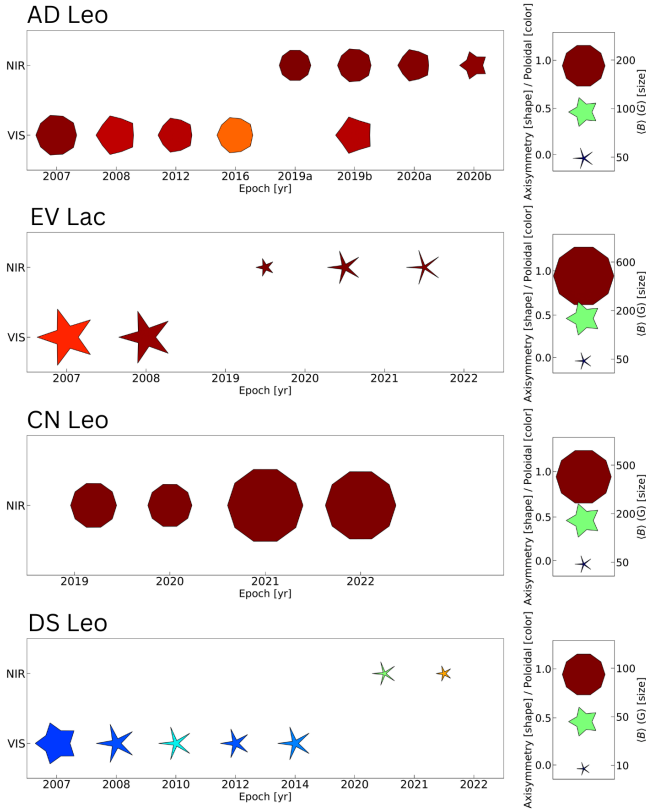


Fig. 14. Evolution of the magnetic topology of AD Leo, EV Lac, CN Leo, and DS Leo. The temporal baseline covers 15 yr, including the archival optical maps (Donati et al. 2008; Morin et al. 2008; Hébrard et al. 2016) and the near-infrared maps reconstructed with SPIRou data in this work and in Bellotti et al. (2023b) for AD Leo. The field strength, level of axisymmetry, and dominant field component (poloidal or toroidal) are encoded with the symbol size, shape, and colour, respectively. The red and blue data points represent poloidal- and toroidal-dominated field geometries, whereas round and star-like shapes indicate mostly axisymmetric and non-axisymmetric configurations.

- For the optical epochs of EV Lac and DS Leo where the rotational modulation of the FWHM is evident, we observed both negative and positive correlations with $|B_l|$, whereas in some cases this correlation was absent. The interpretation of these results is not straightforward. They indicate an underlying complexity in the link between the small-scale field (traced by FWHM) and the large-scale field (traced by B_l), which may not be encapsulated in a simple scaling.
- The long-term behaviour of the epoch-averaged FWHM of Stokes I reflects the secular evolution of the longitudinal field. This is enhanced in particular when high- g_{eff} lines are used, whereas low- g_{eff} lines tend to yield stable FWHM values throughout the time series.
- Using PCA, we obtained the variations in axisymmetry, poloidal-to-toroidal fraction of the axisymmetric component, and complexity for EV Lac, DS Leo, and CN Leo directly from the LSD Stokes V time series, without prior assumptions on stellar parameters or the need of elaborate field topology models.
- The ZDI reconstructions also revealed distinct secular changes in the magnetic topology. For EV Lac the field remained mainly poloidal, dipolar, and with a significant contribution of quadrupolar field. The axisymmetry has decreased almost to 0% in the most recent epoch. For

DS Leo, the poloidal component increased over time with a simultaneous decrease in axisymmetry. The toroidal component has a substantial contribution to the energy budget still, and is mainly axisymmetric, similarly to the optical reconstructions (Donati et al. 2008; Hébrard et al. 2016). For CN Leo, the field maintained a poloidal, dipolar, and axisymmetric configuration, with the field strength following a fluctuating trend similar to B_l .

If we group the long-term evolution of the large-scale field geometry according to spectral type, it seems that the cyclic variability decreases towards later spectral types, as also pointed out by Fuhrmeister et al. (2023) from a long-term monitoring of chromospheric activity indicators. From our work we see that the field of DS Leo (early M type) undergoes rapid variations on short timescales; the field of EV Lac still manifests an evident topological change, but on longer timescales (similar to AD Leo, Bellotti et al. 2023b); and for CN Leo (late M type), there is no substantial evolution. This phenomenon could be correlated to the magnetic field intensity, with stronger fields (i.e. later spectral types) being able to quench surface shear and induce intrinsic stability, as already pointed out by Donati et al. (2008) and Morin et al. (2008).

With the exception of DS Leo, activity cycles were reported for EV Lac and CN Leo from photometric or chromospheric activity monitoring. For EV Lac, Mavridis & Avgoloupis (1986) constrained a 5 yr activity cycle based on flare activity and B -band photometric oscillations over a baseline of 9 yr. Given the gap in our B_l time series between 2010 and 2016, we cannot easily compare the reported timescale with our B_l variations. For CN Leo, photometric analysis of the All Sky Automated Survey (ASAS) light curves revealed an activity cycle of 8.9 ± 0.2 yr (Suárez Mascareño et al. 2016) or 12.0 ± 4.4 yr (Irving et al. 2023). These are 3.3 and 4.4 times longer than the 2.7 yr sine-like variations we recorded for B_l . In contrast, Fuhrmeister et al. (2023) and Mignon et al. (2023) did not report any significant long-term periodicity from chromospheric activity monitoring of CN Leo. These results may resemble what is described for Sun-like stars because there are cases in which magnetic cycles and polarity flips are phased with chromospheric cycles (Boro Saikia et al. 2016; Jeffers et al. 2017), whereas in other cases regular chromospheric oscillations are not reflected in polarimetric variations (Boro Saikia et al. 2022). At the same time, different activity indexes may be sensitive to different regions in the stellar atmospheres, and therefore timescales, which may explain why they did not capture long-term variability for CN Leo (e.g., Cortés-Zuleta et al. 2023; Mignon et al. 2023).

In conclusion, the peculiar evolution of the large-scale magnetic field for the stars examined here provides us with a glimpse of a potential variety in cyclic trends for M dwarfs. This advocates for additional spectropolarimetric monitoring of active M dwarfs for a better constraint on the timescales involved and the extent of such variety over distinct stellar masses and rotation periods.

Acknowledgements. We thank the anonymous referee for the thorough review of the manuscript and the suggestions. We acknowledge funding from the French National Research Agency (ANR) under contract number ANR-18-CE31-0019 (SPiASH). SB acknowledges funding from the European Space Agency (ESA), under the visiting researcher programme. XD acknowledges funding within the framework of the Investissements d’Avenir programme (ANR-15-IDEX-02), through the funding of the ‘Origin of Life’ project of the Univ. Grenoble-Alpes. EM acknowledges funding from FAPEMIG under project number APQ-02493-22 and research productivity grant number 309829/2022-4 awarded by the CNPq, Brazil. BK acknowledges funding from the European Research Council (ERC) under the European Union’s Horizon 2020 research and innovation programme

(Grant agreement No. 865624). Based on observations obtained at the Canada-Hawaii Telescope (CFHT) which is operated by the National Research Council (NRC) of Canada, the Institut National des Sciences de l'Univers of the Centre National de la Recherche Scientifique (CNRS) of France, and the University of Hawaii. The observations at the CFHT were performed with care and respect from the summit of Maunakea which is a significant cultural and historic site. We gratefully acknowledge the CFHT QSO observers who made this project possible. This work has made use of the VALD database, operated at Uppsala University, the Institute of Astronomy RAS in Moscow, and the University of Vienna; Astropy, 12 a community-developed core Python package for Astronomy (Astropy Collaboration 2013, 2018); NumPy (van der Walt et al. 2011); Matplotlib: Visualization with Python (Hunter 2007); SciPy (Virtanen et al. 2020).

References

- Artigau, É., Cadieux, C., Cook, N. J., et al. 2022, *AJ*, **164**, 84
- Astropy Collaboration (Robitaille, T. P., et al.) 2013, *A&A*, **558**, A33
- Astropy Collaboration (Price-Whelan, A. M., et al.) 2018, *AJ*, **156**, 123
- Bagnulo, S., Landolfi, M., Landstreet, J. D., et al. 2009, *PASP*, **121**, 993
- Bellotti, S. 2023, PhD Thesis, IRAP, France
- Bellotti, S., Petit, P., Morin, J., et al. 2022, *A&A*, **657**, A107
- Bellotti, S., Fares, R., Vidotto, A. A., et al. 2023a, *A&A*, **676**, A139
- Bellotti, S., Morin, J., Lehmann, L. T., et al. 2023b, *A&A*, **676**, A56
- Bertaux, J. L., Lallement, R., Ferron, S., Boonne, C., & Bodichon, R. 2014, *A&A*, **564**, A46
- Boro Saikia, S., Jeffers, S. V., Morin, J., et al. 2016, *A&A*, **594**, A29
- Boro Saikia, S., Marvin, C. J., Jeffers, S. V., et al. 2018, *A&A*, **616**, A108
- Boro Saikia, S., Lüftinger, T., Folsom, C. P., et al. 2022, *A&A*, **658**, A16
- Browning, M. K. 2008, *ApJ*, **676**, 1262
- Carmona, A., Delfosse, X., Bellotti, S., et al. 2023, *A&A*, **674**, A110
- Chabrier, G., & Baraffe, I. 1997, *A&A*, **327**, 1039
- Chabrier, G., & Küker, M. 2006, *A&A*, **446**, 1027
- Charbonneau, P. 2010, *Liv. Rev. Sol. Phys.*, **7**, 3
- Charbonneau, P. 2020, *Liv. Rev. Sol. Phys.*, **17**, 4
- Claret, A., & Bloemen, S. 2011, *A&A*, **529**, A75
- Cook, N. J., Artigau, É., Doyon, R., et al. 2022, *PASP*, **134**, 114509
- Cortés-Zuleta, P., Boisse, I., Klein, B., et al. 2023, *A&A*, **673**, A14
- Cristofari, P. I., Donati, J. F., Folsom, C. P., et al. 2023, *MNRAS*, **522**, 1342
- da Gomes Silva, J., Santos, N. C., Bonfils, X., et al. 2012, *A&A*, **541**, A9
- Delchambre, L. 2015, *MNRAS*, **446**, 3545
- del Toro Iniesta, J. C. 2003, *Introduction to Spectropolarimetry* (Cambridge: Cambridge University Press)
- Donati, J. F. 2003, in *Solar Polarization*, eds. J. Trujillo-Bueno, & J. Sanchez Almeida, *ASP Conf. Ser.*, **307**, 41
- Donati, J. F., & Brown, S. F. 1997, *A&A*, **326**, 1135
- Donati, J. F., Semel, M., Carter, B. D., Rees, D. E., & Collier Cameron, A. 1997, *MNRAS*, **291**, 658
- Donati, J. F., Mengel, M., Carter, B. D., et al. 2000, *MNRAS*, **316**, 699
- Donati, J. F., Catala, C., Landstreet, J. D., & Petit, P. 2006a, in *Solar Polarization 4*, eds. R. Casini, & B. W. Lites, *ASP Conf. Ser.*, **358**, 362
- Donati, J. F., Howarth, I. D., Jardine, M. M., et al. 2006b, *MNRAS*, **370**, 629
- Donati, J. F., Morin, J., Petit, P., et al. 2008, *MNRAS*, **390**, 545
- Donati, J. F., Kouchak, D., Moutou, C., et al. 2020, *MNRAS*, **498**, 5684
- Donati, J. F., Cristofari, P. I., Finocietti, B., et al. 2023a, *MNRAS*, **525**, 455
- Donati, J. F., Lehmann, L. T., Cristofari, P. I., et al. 2023b, *MNRAS*, **525**, 2015
- Dorman, B., Nelson, L. A., & Chau, W. Y. 1989, *ApJ*, **342**, 1003
- Dungee, R., van Saders, J., Gaidos, E., et al. 2022, *ApJ*, **938**, 118
- Durney, B. R., De Young, D. S., & Roxburgh, I. W. 1993, *Sol. Phys.*, **145**, 207
- Erba, C., Folsom, C. P., David-Uraz, A., et al. 2024, *ApJ*, submitted [arXiv:2401.09722]
- Fares, R., Moutou, C., Donati, J. F., et al. 2013, *MNRAS*, **435**, 1451
- Finley, A. J., & Matt, S. P. 2017, *ApJ*, **845**, 46
- Folsom, C. P., Petit, P., Bouvier, J., et al. 2016, *MNRAS*, **457**, 580
- Folsom, C. P., Bouvier, J., Petit, P., et al. 2018, *MNRAS*, **474**, 4956
- Folsom, C. P., Ó Fionnagáin, D., Fossati, L., et al. 2020, *A&A*, **633**, A48
- Fouqué, P., Martioli, E., Donati, J. F., et al. 2023, *A&A*, **672**, A52
- Fuhrmeister, B., Czesla, S., Perdelwitz, V., et al. 2023, *A&A*, **670**, A71
- Gastine, T., Morin, J., Duarte, L., et al. 2013, *A&A*, **549**, L5
- Gray, D. F. 2005, *The Observation and Analysis of Stellar Photospheres* (Cambridge: Cambridge University Press)
- Gustafsson, B., Edvardsson, B., Eriksson, K., et al. 2008, *A&A*, **486**, 951
- Haywood, R. D., Milbourne, T. W., Saar, S. H., et al. 2022, *ApJ*, **935**, 6
- Hébrard, É. M., Donati, J. F., Delfosse, X., et al. 2016, *MNRAS*, **461**, 1465
- Huerta, M., Johns-Krull, C. M., Prato, L., Hartigan, P., & Jaffe, D. T. 2008, *ApJ*, **678**, 472
- Hunter, J. D. 2007, *Comput. Sci. Eng.*, **9**, 90
- Irving, Z. A., Saar, S. H., Wargelin, B. J., & do Nascimento, J.-D. 2023, *ApJ*, **949**, 51
- Jeffers, S. V., Boro Saikia, S., Barnes, J. R., et al. 2017, *MNRAS*, **471**, L96
- Kitchatinov, L. L., Moss, D., & Sokoloff, D. 2014, *MNRAS*, **442**, L1
- Klein, B., Donati, J.-F., Moutou, C., et al. 2021, *MNRAS*, **502**, 188
- Klein, B., Zicher, N., Kavanagh, R. D., et al. 2022, *MNRAS*, **512**, 5067
- Kochukhov, O. 2021, *A&ARv*, **29**, 1
- Kochukhov, O., & Lavail, A. 2017, *ApJ*, **835**, L4
- Kochukhov, O., Makaganiuk, V., & Piskunov, N. 2010, *A&A*, **524**, A5
- Lafarga, M., Ribas, I., Reiners, A., et al. 2021, *A&A*, **652**, A28
- Landi Degl'Innocenti, E. 1992, in *Magnetic Field Measurements*, eds. F. Sanchez, M. Collados, & M. Vazquez, 71
- Landi Degl'Innocenti, E., & Landolfi, M. 2004, *Polarization in Spectral Lines* (Dordrecht: Kluwer Academic Publishers), 307
- Lavaill, A., Kochukhov, O., & Wade, G. A. 2018, *MNRAS*, **479**, 4836
- Lehmann, L. T., & Donati, J. F. 2022, *MNRAS*, **514**, 2333
- Lehmann, L. T., Donati, J. F., Fouqué, P., et al. 2024, *MNRAS*, **527**, 4330
- Lienhard, F., Mortier, A., Cegla, H. M., et al. 2023, *MNRAS*, **522**, 5862
- Lopez-Santiago, J., Martino, L., Míguez, J., & Vázquez, M. A. 2020, *AJ*, **160**, 273
- Lorenzo-Oliveira, D., Freitas, F. C., Meléndez, J., et al. 2018, *A&A*, **619**, A73
- Luger, R., & Barnes, R. 2015, *Astrobiology*, **15**, 119
- Maeder, A., & Meynet, G. 2000, *ARA&A*, **38**, 143
- Mavridis, L. N., & Avgoloupis, S. 1986, *A&A*, **154**, 171
- Meunier, N. 2021, arXiv e-prints [arXiv:2104.06072]
- Mignon, L., Meunier, N., Delfosse, X., et al. 2023, *A&A*, **675**, A168
- Morin, J. 2012, in *EAS Pub. Ser.*, eds. C. Reylé, C. Charbonnel, & M. Schultheis, 57, 165
- Morin, J., Donati, J. F., Petit, P., et al. 2008, *MNRAS*, **390**, 567
- Morin, J., Donati, J. F., Petit, P., et al. 2010, *MNRAS*, **407**, 2269
- Morin, J., Delfosse, X., Donati, J. F., et al. 2011, in *SF2A-2011: Proceedings of the Annual meeting of the French Society of Astronomy and Astrophysics*, eds. G. Alecian, K. Belkacem, R. Samadi, & D. Valls-Gabaud, 503
- Mullan, D. J., & MacDonald, J. 2001, *ApJ*, **559**, 353
- Noyes, R. W., Hartmann, L. W., Baliunas, S. L., Duncan, D. K., & Vaughan, A. H. 1984, *ApJ*, **279**, 763
- Pecaut, M. J., & Mamajek, E. E. 2013, *ApJS*, **208**, 9
- Petit, P., Donati, J. F., & Collier Cameron, A. 2002, *MNRAS*, **334**, 374
- Petit, P., Louge, T., Théado, S., et al. 2014, *PASP*, **126**, 469
- Petit, P., Folsom, C. P., Donati, J. F., et al. 2021, *A&A*, **648**, A55
- Phan-Bao, N., Lim, J., Donati, J.-F., Johns-Krull, C. M., & Martín, E. L. 2009, *ApJ*, **704**, 1721
- Press, W. H., Teukolsky, S. A., Vetterling, W. T., & Flannery, B. P. 1992, *Numerical Recipes in FORTRAN. The Art of Scientific Computing* (Cambridge: Cambridge University Press)
- Queloz, D., Henry, G. W., Sivan, J. P., et al. 2001, *A&A*, **379**, 279
- Rabus, M., Lachaume, R., Jordán, A., et al. 2019, *MNRAS*, **484**, 2674
- Rachkovsky, D. N. 1967, *Izvestiya Ordena Trudovogo Krasnogo Znameni Krymskoj Astrofizicheskoy Observatorii*, **37**, 56
- Rees, D. E., & Semel, M. D. 1979, *A&A*, **74**, 1
- Reid, I. N., Cruz, K. L., Allen, P., et al. 2004, *AJ*, **128**, 463
- Reiners, A. 2012, *Liv. Rev. Sol. Phys.*, **9**, 1
- Reiners, A., & Basri, G. 2009, *A&A*, **496**, 787
- Reiners, A., Shulyak, D., Käpylä, P. J., et al. 2022, *A&A*, **662**, A41
- Reinhold, T., & Hekker, S. 2020, *A&A*, **635**, A43
- Ryabchikova, T., Piskunov, N., Kurucz, R. L., et al. 2015, *Phys. Scr.*, **90**, 054005
- Saar, S. H. 1994, in *Infrared Solar Physics*, eds. D. M. Rabin, J. T. Jefferies, & C. Lindsey, 154, 493
- Sanderson, T. R., Appourchaux, T., Hoeksema, J. T., & Harvey, K. L. 2003, *J. Geophys. Res. (Space Physics)*, **108**, 1035
- Schrjver, C. J., & Zwaan, C. 2000, *Solar and Stellar Magnetic Activity* (Cambridge: Cambridge University Press)
- See, V., Matt, S. P., Finley, A. J., et al. 2019, *ApJ*, **886**, 120
- Segura, A., Walkowicz, L. M., Meadows, V., Kasting, J., & Hawley, S. 2010, *Astrobiology*, **10**, 751
- Semel, M. 1989, *A&A*, **225**, 456
- Shulyak, D., Reiners, A., Wende, S., et al. 2011, in *16th Cambridge Workshop on Cool Stars, Stellar Systems, and the Sun*, eds. C. Johns-Krull, M. K. Browning, & A. A. West, *ASP Conf. Ser.*, **448**, 1263
- Shulyak, D., Reiners, A., Engeln, A., et al. 2017, *Nature*, **1**, 0184
- Shulyak, D., Reiners, A., Nagel, E., et al. 2019, *A&A*, **626**, A86
- Skilling, J., & Bryan, R. K. 1984, *MNRAS*, **211**, 111
- Skumanich, A. 1972, *ApJ*, **171**, 565
- Stelzer, B., Marino, A., Micela, G., López-Santiago, J., & Liefke, C. 2013, *MNRAS*, **431**, 2063
- Suárez Mascareño, A., Rebolo, R., & González Hernández, J. I. 2016, *A&A*, **595**, A12

- Suárez Mascareño, A., Rebolo, R., González Hernández, J. I., et al. 2018, *A&A*, **612**, A89
- Tanner, J. D., Basu, S., & Demarque, P. 2013, *ApJ*, **767**, 78
- Tilley, M. A., Segura, A., Meadows, V., Hawley, S., & Davenport, J. 2019, *Astrobiology*, **19**, 64
- Unno, W. 1956, *PASJ*, **8**, 108
- VanderPlas, J. T. 2018, *ApJS*, **236**, 16
- van der Walt, S., Colbert, S. C., & Varoquaux, G. 2011, *Comput. Sci. Eng.*, **13**, 22
- van Saders, J. L., & Pinsonneault, M. H. 2012, *ApJ*, **746**, 16
- Vidotto, A. A., Jardine, M., Morin, J., et al. 2013, *A&A*, **557**, A67
- Vidotto, A. A., Jardine, M., Morin, J., et al. 2014, *MNRAS*, **438**, 1162
- Virtanen, P., Gommers, R., Burovski, E., et al. 2020, <https://doi.org/10.5281/zenodo.4100507>
- Wargelin, B. J., Saar, S. H., Pojmański, G., Drake, J. J., & Kashyap, V. L. 2017, *MNRAS*, **464**, 3281
- Wright, N. J., Drake, J. J., Mamajek, E. E., & Henry, G. W. 2011, *ApJ*, **743**, 48
- Yadav, R. K., Christensen, U. R., Morin, J., et al. 2015, *ApJ*, **813**, L31
- Zechmeister, M., & Kürster, M. 2009, *A&A*, **496**, 577
- Zeeman, P. 1897, *Nature*, **55**, 347

Appendix A: ZDI analysis of unpublished DS Leo data

In this appendix, we provide the ZDI reconstruction of the large-scale magnetic field of DS Leo for two Narval epochs with unpublished data, namely 2010 and 2012. The input parameters were $i = 60^\circ$ and $v_{\text{eq}} \sin(i) = 2 \text{ km s}^{-1}$ for both epochs. For 2010, we successfully constrained differential rotation with a procedure similar to the one described in Sec. 6. As shown in Fig. A.1, the optimised parameters are $P_{\text{rot,eq}} = 13.51 \pm 0.08 \text{ d}$ and $d\Omega = 0.074 \pm 0.012 \text{ rad d}^{-1}$. These values are compatible with those estimated from Narval 2008 observations (Donati et al. 2008) and 2014 observations (Hébrard et al. 2016) within 1σ , and are 3.9 and 1.7 times larger than the SPIRou 2020b2021a and 2021b2022a values, respectively. This confirms that the differential rotation rate of DS Leo may be transitioning to slower values over time. For the 2012 Narval epoch, the differential rotation search is inconclusive, hence we fixed the stellar input parameters for ZDI to $P_{\text{rot}} = 13.91 \text{ d}$ and $d\Omega = 0.0 \text{ rad d}^{-1}$. The maximum degree of the harmonic expansion was set to $l_{\text{max}} = 8$, and the linear limb darkening coefficient to 0.6964 (Claret & Bloemen 2011).

Table A.1. Properties of the magnetic map for the 2010 and 2012 Narval unpublished epochs.

	2010	2012
B_{mean} [G]	64.7	49.4
B_{max} [G]	129.5	113.9
B_{pol} [%]	36.7	21.1
B_{tor} [%]	63.3	78.9
B_{dip} [%]	71.6	47.3
B_{quad} [%]	21.5	36.8
B_{oct} [%]	4.2	14.0
B_{axisym} [%]	64.7	81.8
$B_{\text{axisym,pol}}$ [%]	8.8	15.1

Notes. The following quantities are listed: mean magnetic strength; maximum magnetic strength; poloidal and toroidal magnetic energy as a fraction of the total energy; dipolar, quadrupolar, and octupolar magnetic energy as a fraction of the poloidal energy; axisymmetric magnetic energy as a fraction of the total energy.

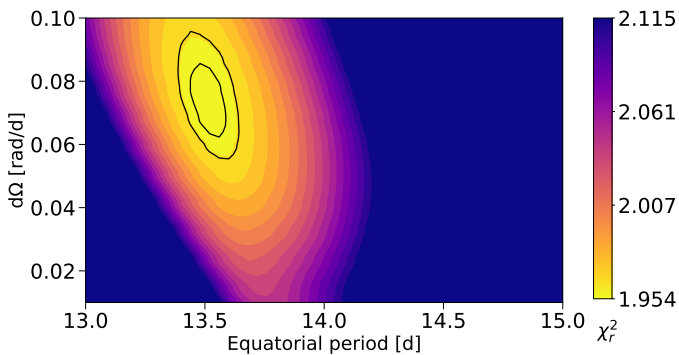


Fig. A.1. Differential rotation search for DS Leo for the 2010 Narval data set. The plots show the χ_r^2 landscape over a grid of $(P_{\text{rot,eq}}, d\Omega)$ pairs, with the same format as in Fig. 11.

The profiles are shown in Fig. A.2, where we observe clear Zeeman signatures in 2010 and noisier Stokes V profiles in 2012. While we were not able to optimise the filling factor f_V for the

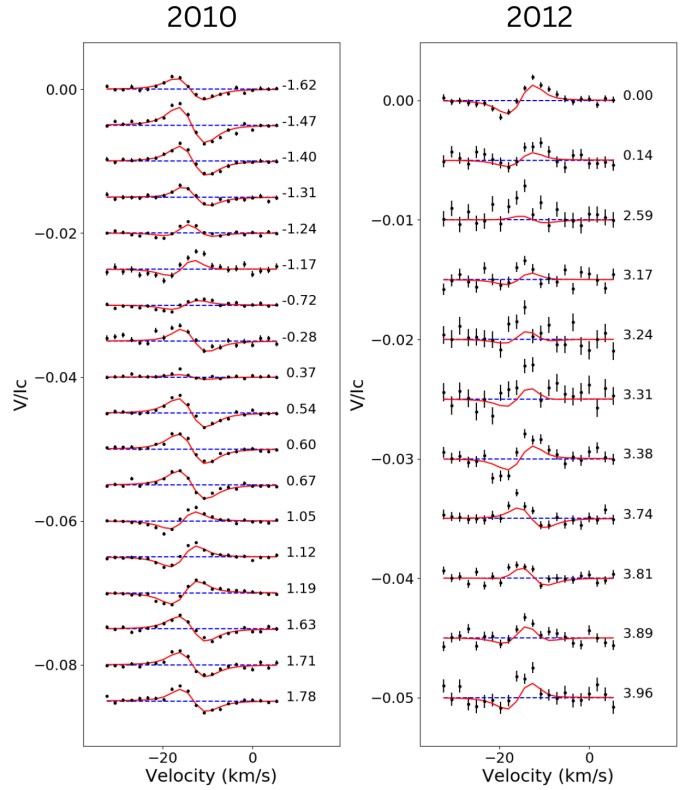


Fig. A.2. Narval time series of Stokes V profiles of DS Leo. Top left: 2010. Bottom: 2012. The cycles in this plot are computed with Eq. (3) while using the median HJD for each epoch. The format is the same as in Fig. D.1.

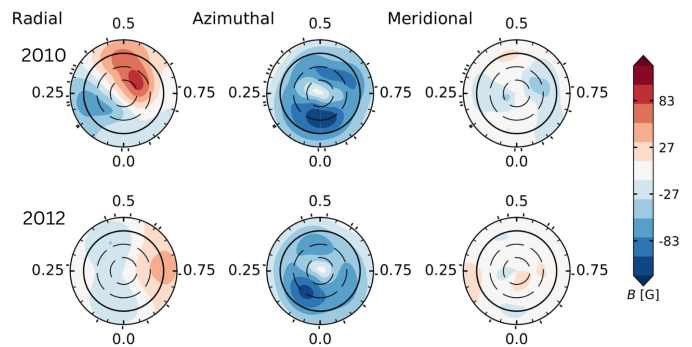


Fig. A.3. Reconstructed ZDI maps in flattened polar view of DS Leo. Left: 2010. Right: 2012. The 2010 map accounts for the constrained differential rotation. The format is the same as in Fig. 10.

2010 epoch, we constrained it to be $f_V = 14\%$ for the 2012 epoch. However, setting $f_V = 100\%$ for the reconstruction of the 2012 time series does not alter the map appreciably, hence we proceeded with $f_V = 100\%$ for both 2010 and 2012 Stokes V time series. The profiles were fitted to a χ_r^2 level of 1.9 from an initial value of 15.8 and 3.7 for 2010 and 2012, respectively.

The maps are given in Fig. A.3 and the corresponding field characteristics are reported in Table A.1. Overall, the characteristics reveal a complex topology, consistently with previous field reconstructions (Donati et al. 2008; Hébrard et al. 2016). For both 2010 and 2012, the field is predominantly toroidal ($> 60\%$), and the poloidal component is mostly dipolar ($> 50\%$), with a significant quadrupolar component (21 and 36% for 2010 and 2012, respectively). The poloidal component is also mostly

non-axisymmetric, accounting for 9% of the magnetic energy in 2010 and 15% in 2012. The mean field strength is approximately 64 and 49 G for 2010 and 2012, compatible with the decrease in field strength reported by Hébrard et al. (2016) for the 2014 Narval epoch.

Appendix B: Additional FWHM analyses and figures

In Fig. B.1, we show the different Stokes I profiles for EV Lac, DS Leo and CN Leo when computed with magnetically sensitive ($g_{\text{eff}} > 1.2$) and insensitive ($g_{\text{eff}} < 1.2$) lines. These profiles were used for the FWHM analyses described in Sec. 4.

B.1. Proxy of the unsigned magnetic field

For all three stars, the mean FWHM and the dispersion of individual epochs is larger when employing high- g_{eff} lines than the full and the low- g_{eff} mask, owing to a larger influence of the Zeeman effect on the broadening of the lines. The values are reported in Table B.1 and an illustration of the different Stokes I profiles for the two line selections is given in Fig. B.1. Taking the epoch-averaged Stokes I profiles, we computed the quadratic differential broadening between the low- and high- g_{eff} masks.

For example, the mean FWHM for EV Lac in the SPIRou 2019b epoch when using low- and high- g_{eff} is 17 and 29 km s⁻¹, respectively. The corresponding quadratic differential broadening is $\delta v_B = 24$ km s⁻¹. We then solve the following formula

$$\delta v_B = 1.4 \cdot 10^{-6} \lambda_0 g_{\text{eff}} B, \quad (\text{B.1})$$

for B , with δv_B in km s⁻¹, λ_0 in nm and B in G. The value of B obtained from Eq. B.1 is then divided by two because the Zeeman effect is symmetric, acting in both the positive and negative direction with respect to line centre. The above value of differential quadratic broadening translates into $B = 5.4$ kG. The wavelength λ_0 is the normalisation wavelength of the low-Landé lines (700 nm for optical and 1700 nm for near-infrared) and g_{eff} the normalisation Landé factor. For EV Lac, the latter is 0.85 in optical and 0.95 in near-infrared, for DS Leo is 0.82 and 0.94, and for CN Leo it is 0.98 in near-infrared. The proportionality factor encapsulates fundamental constants such as speed of light, electron mass and electron charge (Zeeman 1897; Landi Degl'Innocenti et al. 1992).

For EV Lac, we obtained B within 4.9-5.4 kG in near-infrared and 4.2-4.8 kG in optical, which are similar to the estimates reported in the literature from Zeeman broadening and intensification modelling (Saar et al. 1994; Shulyak et al. 2017, 2019). For DS Leo, B is 2 kG and 2.5 kG for optical and near-infrared. For CN Leo, B is 4.9 kG for optical and 3.7-4.7 kG for near-infrared. The values for DS Leo and CN Leo are larger than the literature estimates, that is, twice for DS Leo (Shulyak et al. 2011) and 1.6 times for CN Leo (Shulyak et al. 2019). These discrepancies are unlikely to be associated with a magnetic field evolution, as we did not capture a significant temporal change of FWHM (see Sec. 4.3). Instead, they probably stem from the

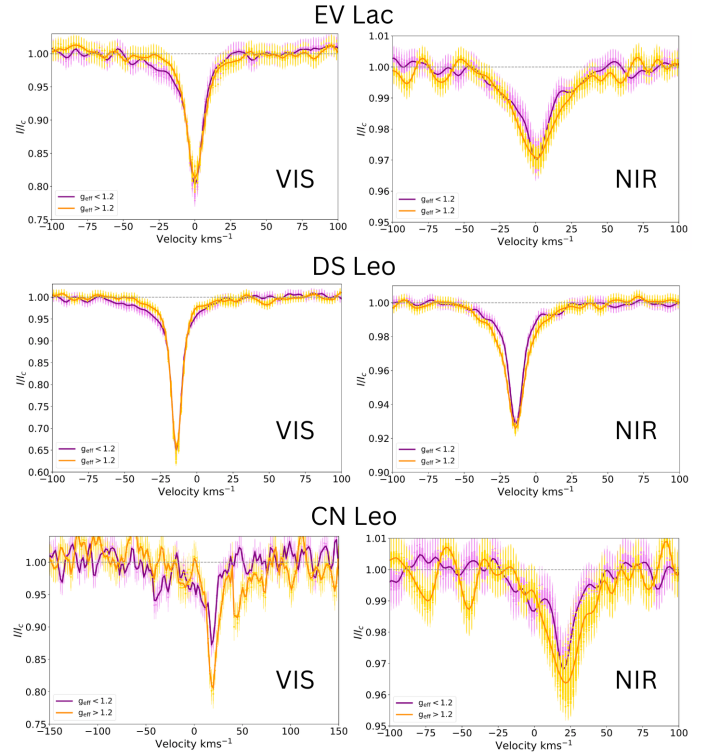


Fig. B.1. Comparison of Stokes I profiles for EV Lac, DS Leo, and CN Leo when computed with different line selections based on magnetic sensitivity. Each panel contains all the observations and their median for high- g_{eff} (yellow) and low- g_{eff} (purple) line selections.

fact that, for instance, the identification of the continuum in the vicinity of the lines is not straightforward, affecting the modelling from which the FWHM is estimated. Identifying the continuum is complicated by the unaccounted molecular lines in the LSD line list and the lower S/N due to the low number of spectral lines used in LSD, as displayed in Fig. B.1. For DS Leo in near-infrared, we also carried out this exercise starting from a 4000 K mask, but we found values of B around 1.7 kG, thus still higher than the literature values.

B.2. Complementary figures to the FWHM analysis

We also present the analysis investigating the rotational modulation of the FWHM obtained with the different masks, in optical and near-infrared, for EV Lac and CN Leo. For EV Lac, we observe rotational modulation in the optical epochs, whereas in near-infrared we cannot capture such behaviour due to a larger dispersion of the data. Likewise, CN Leo's near-infrared time series of FWHM does not reveal rotational modulation (see Sec. 4 for a detailed description). We finally illustrate the correlation analysis between FWHM and $|B|$ for DS Leo, for which we note a variety of correlations depending on the epoch considered.

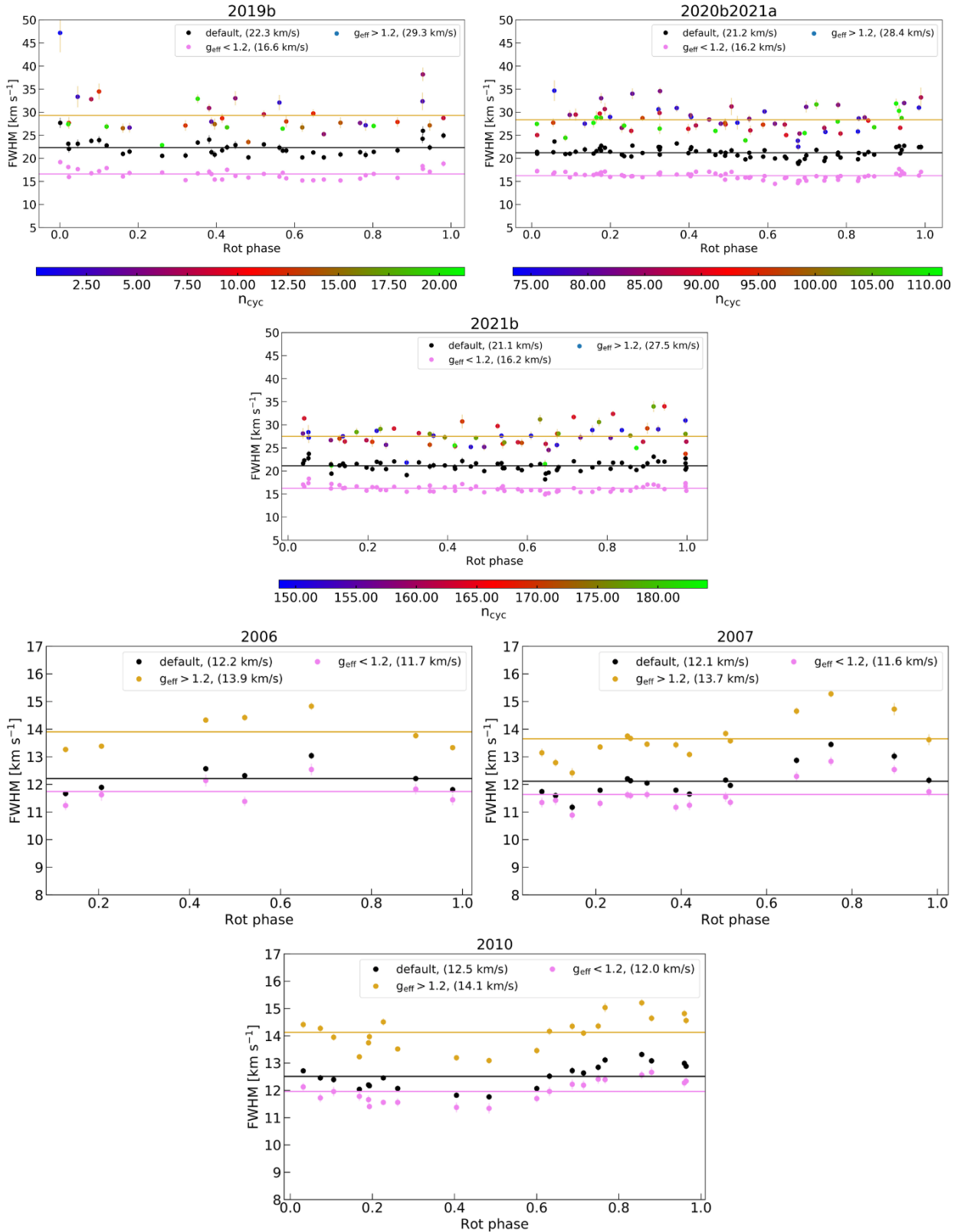


Fig. B.2. Rotational modulation analysis of FWHM for EV Lac. The three upper panels correspond to the near-infrared epochs (2019b, 2020b2021a, and 2021b), whereas the three lower panels correspond to the optical epochs containing enough data points (2006, 2007, and 2010). Plotted in each panel is the phase-folded time series of FWHM computed with the full, low- g_{eff} , and high- g_{eff} mask with a horizontal line representing the mean FWHM value. For the near-infrared epochs the high- g_{eff} time series is colour-coded by rotational cycle to inspect signs of short-term variability. The latter can be seen as data points that are at significantly different values of FWHM at different cycles, but sharing the same rotational phase (e.g., phase 0.05 or 0.30 of the 2020b2021a epoch).

Table B.1. Unsigned magnetic field estimates from differential broadening measurements for EV Lac, DS Leo, and CN Leo.

Epoch	Domain	$\langle \text{FWHM}_{g_{\text{eff}} < 1.2} \rangle$ [km s ⁻¹]	$\langle \text{FWHM}_{g_{\text{eff}} > 1.2} \rangle$ [km s ⁻¹]	δFWHM [km s ⁻¹]	B [kG]
EV Lac					
2005	VIS	11.5	14.1	8.3	4.8
2006	VIS	11.7	13.9	7.4	4.4
2007	VIS	11.6	13.7	7.1	4.2
2010	VIS	12.0	14.6	8.3	4.8
2012	VIS	12.0	14.1	7.5	4.4
2019b	NIR	16.6	29.3	24.1	5.4
2020b2021a	NIR	16.2	28.4	23.3	5.2
2021b	NIR	16.2	27.5	22.2	4.9
DS Leo					
2006	VIS	8.4	9.4	4.2	2.6
2007	VIS	8.2	8.9	3.5	2.2
2008	VIS	8.2	9.0	3.6	2.2
2009	VIS	8.2	9.1	3.9	2.4
2010	VIS	8.2	9.1	3.9	2.4
2011	VIS	8.2	9.0	3.8	2.2
2012	VIS	8.0	9.2	4.4	2.8
2014	VIS	8.1	9.0	4.0	2.5
2020b2021a	NIR	11.2	14.4	9.0	2.0
2021b2022a	NIR	11.2	14.3	8.9	2.0
CN Leo					
2008	VIS	7.0	12.1	9.9	4.9
2019a	NIR	11.9	20.9	17.3	3.7
2019b2020a	NIR	11.9	24.9	21.9	4.7
2020b2021a	NIR	12.1	21.6	17.8	3.8
2021b2022a	NIR	12.1	21.8	18.1	3.9

Notes. The columns are: 1) epoch of the observations, 2) wavelength domain, 3) average FWHM of low- g_{eff} lines, 4) average FWHM of high- g_{eff} lines, 5) quadratic differential broadening, and 6) total unsigned magnetic field.

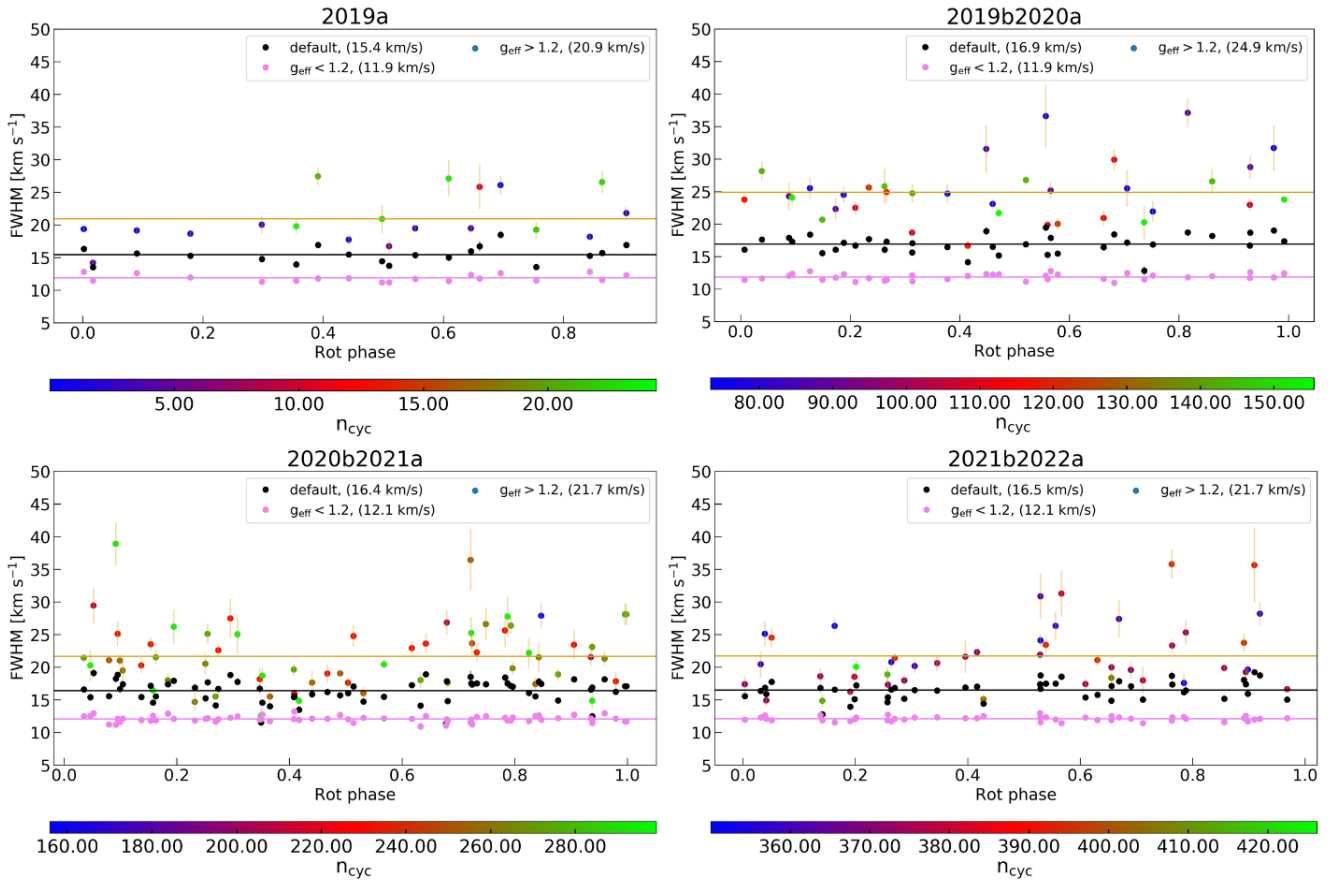


Fig. B.3. Rotational modulation analysis of FWHM for CN Leo. The panels illustrate the near-infrared epochs: 2019a, 2019b2020a, 2020b2021a, and 2021b2022a. The format is the same as in Fig. B.2.

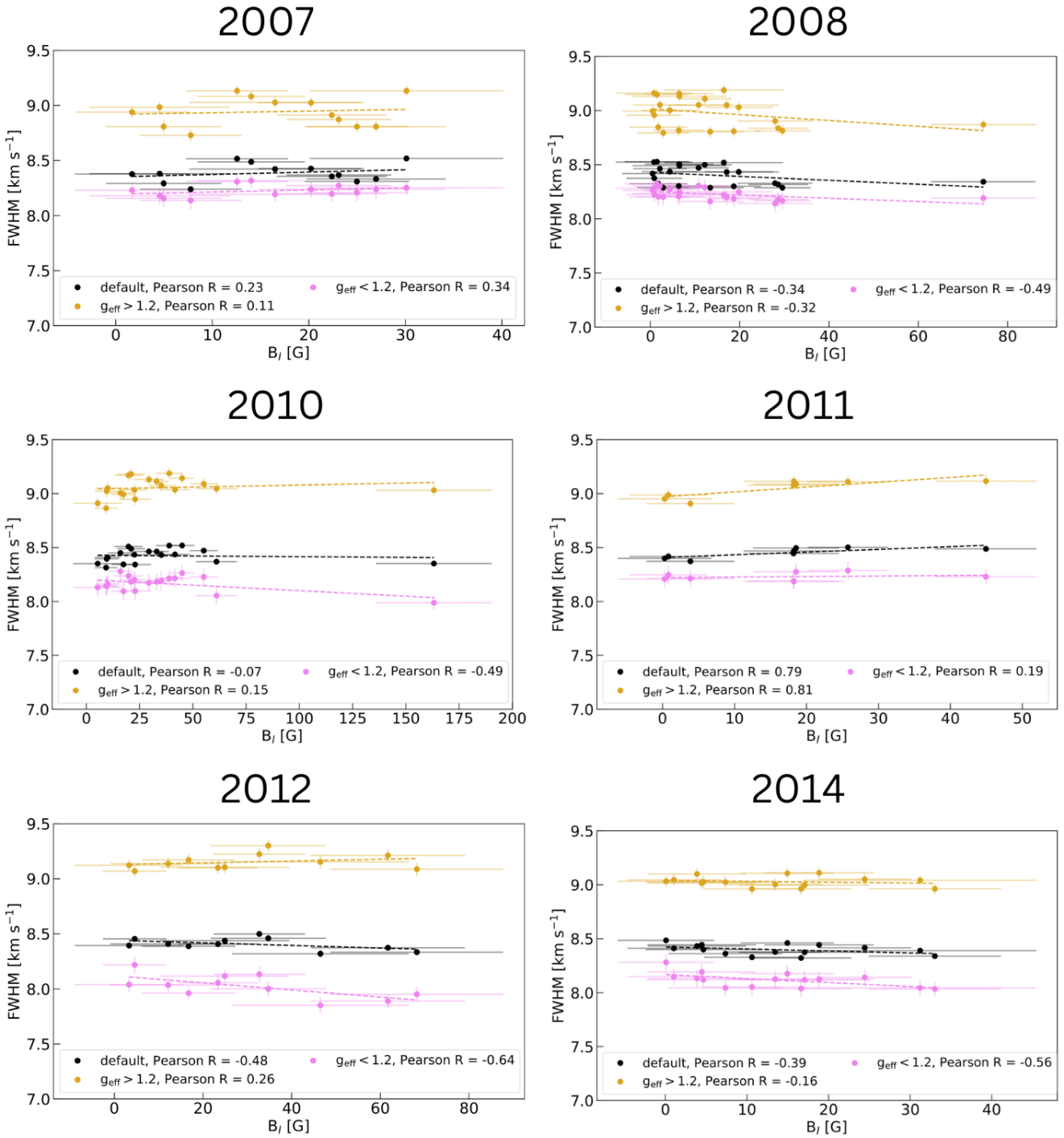


Fig. B.4. Correlation analysis between FWHM and $|B_l|$ for DS Leo. The six panels correspond to the optical epochs in which rotational modulation is present: 2007, 2008, 2010, 2011, 2012, and 2014. In all panels the data points are colour-coded based on the line mask used for LSD: full (black), low- g_{eff} (purple), and high- g_{eff} (yellow).

Appendix C: Complementary figures to PCA

In this appendix, we illustrate the PCA analysis applied to DS Leo and CN Leo outlined in Sec. 5. The mean Stokes V profile

analysis and the per-epoch analysis of the coefficients are shown in Fig. C.1 and Fig. C.2.

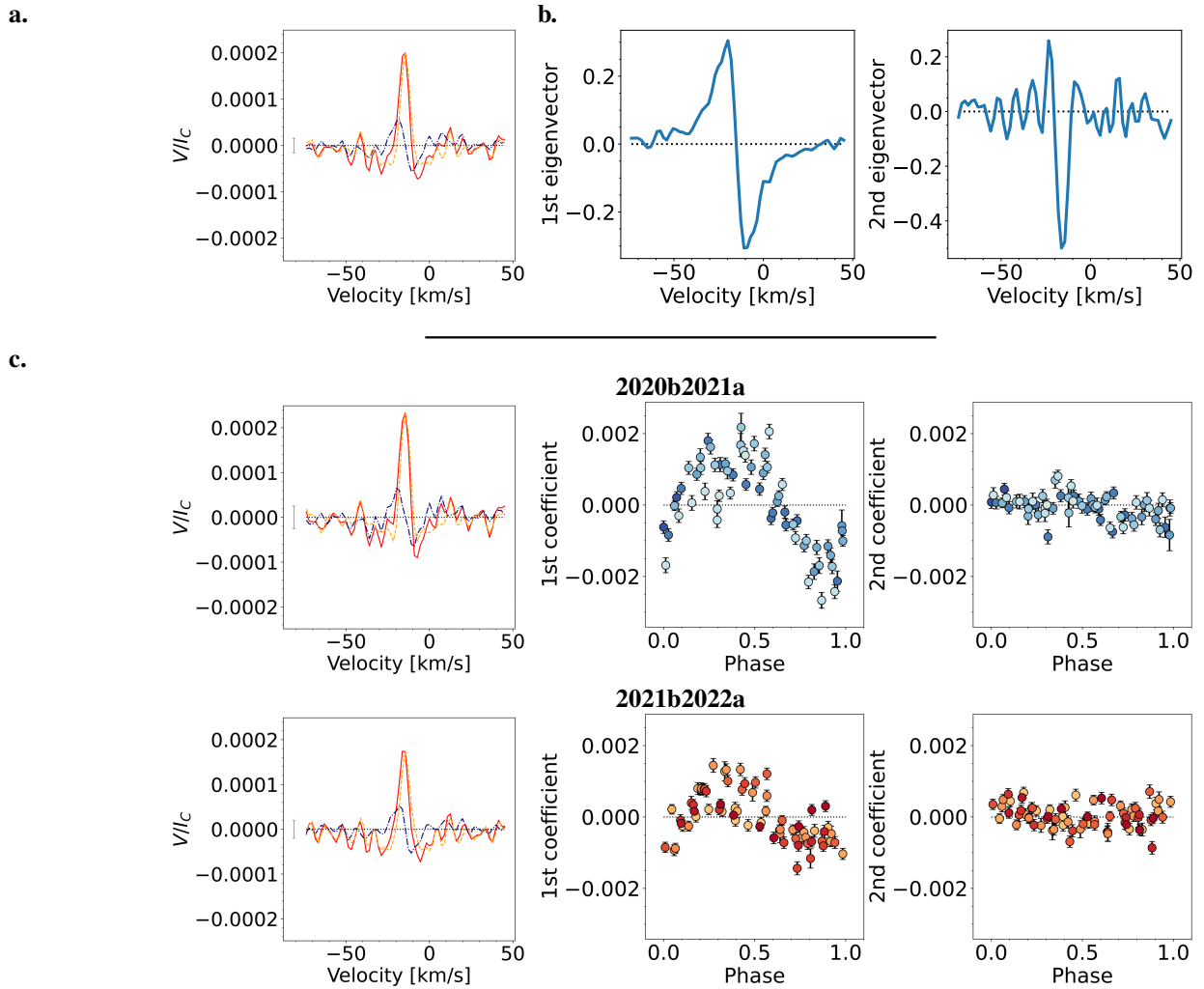


Fig. C.1. Same as Fig. 9, but for DS Leo.

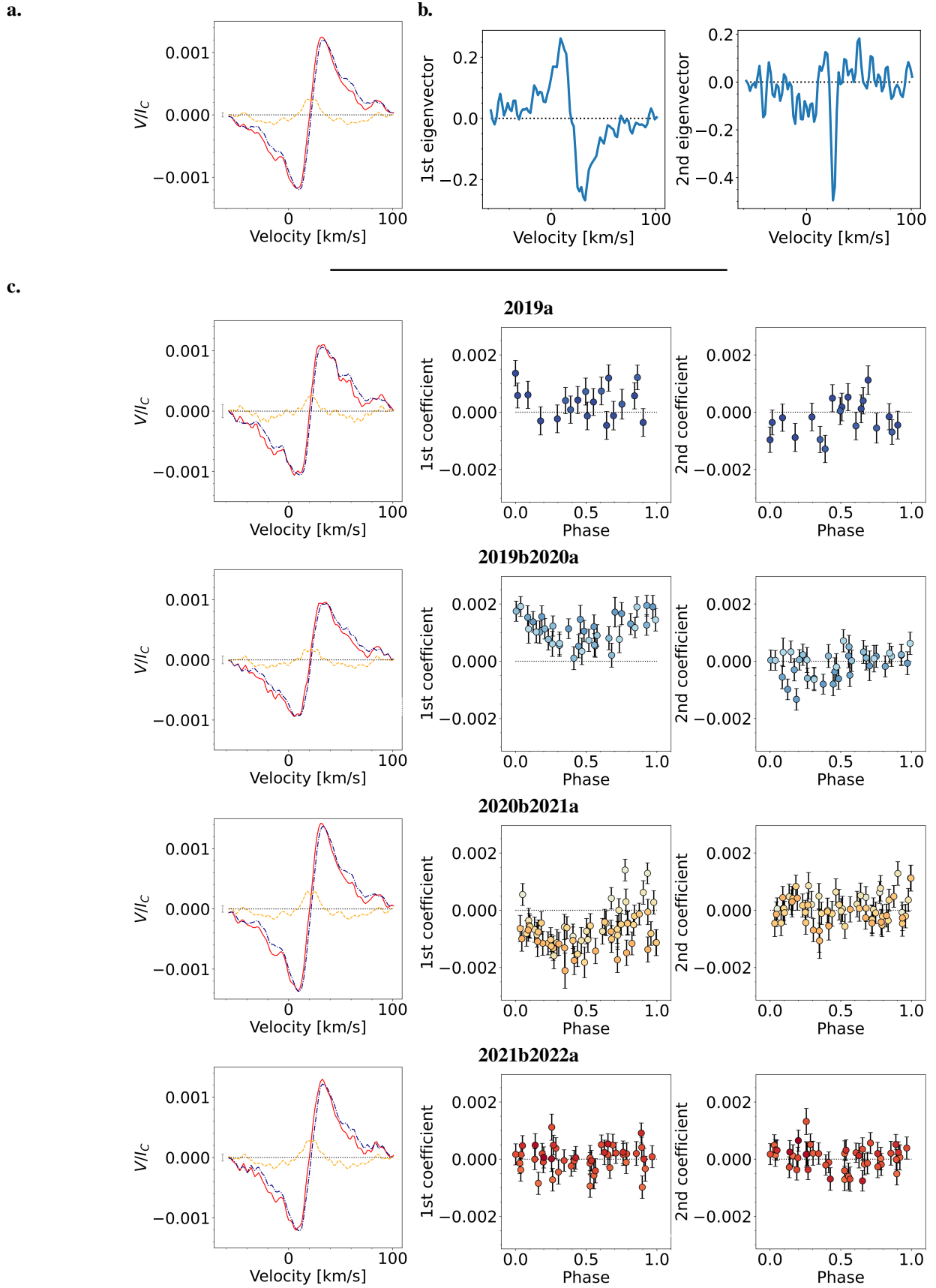


Fig. C.2. Same as Fig. 9, but for CN Leo.

Appendix D: Complementary figures to the ZDI analysis

In this appendix, we provide complementary figures to the Zeeman-Doppler imaging analysis (see Sec. 6). Fig. D.1,

Fig. D.2 and Fig. D.3 show the near-infrared time series of circularly polarised Stokes V profiles for EV Lac, DS Leo, and CN Leo.

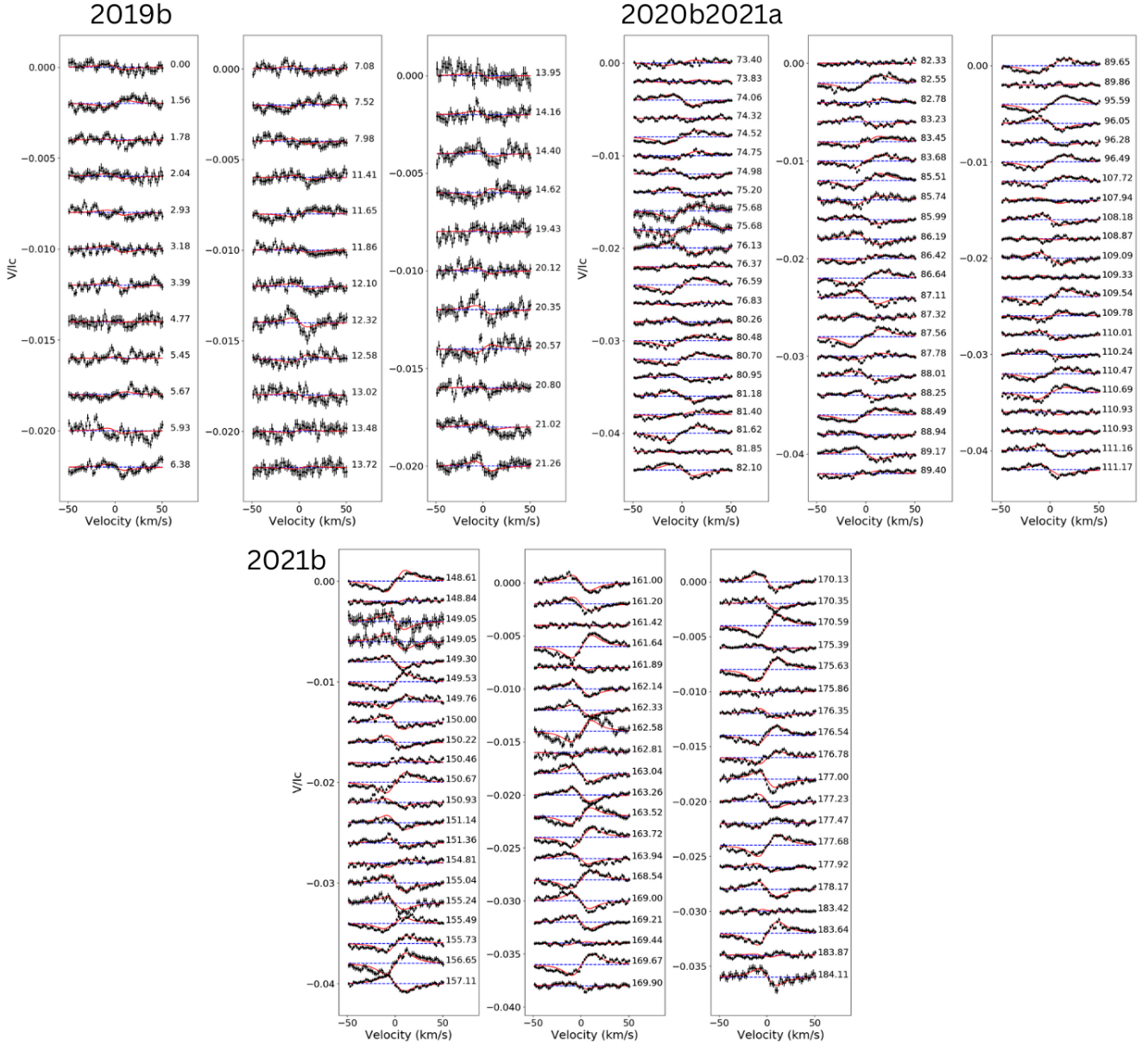


Fig. D.1. SPIRou time series of Stokes V profiles of EV Lac. Top left: 2019b. Top right: 2020b2021a. Bottom: 2021b. The observations are shown in black and the models in red, and the rotational cycle is printed on the right (see Eq. (3)). The profiles are offset vertically for visualisation purposes.

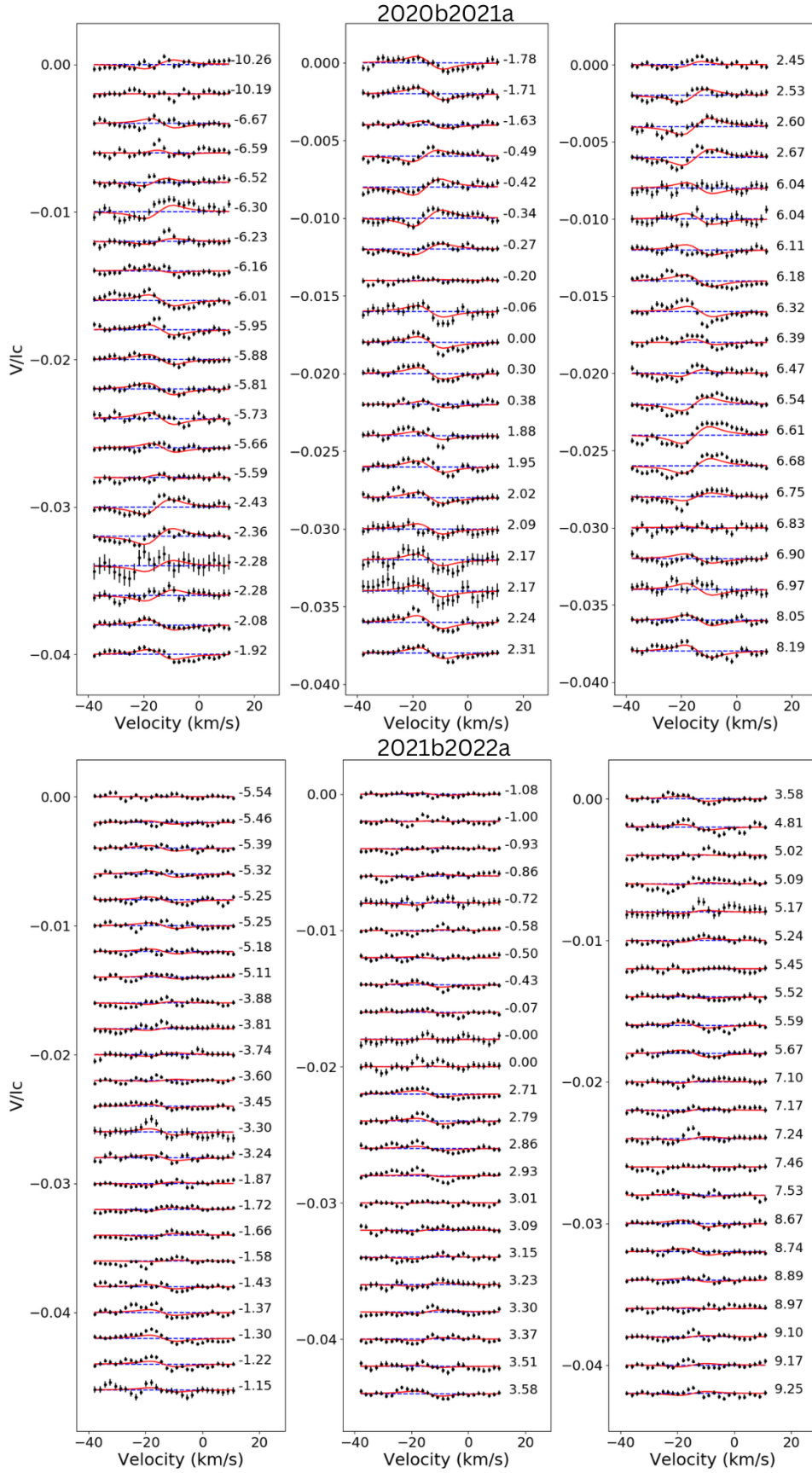


Fig. D.2. SPIRou time series of Stokes V profiles of DS Leo. Top: 2020b2021a. Bottom: 2021b2022a. The cycles in this plot are computed with Eq. (3) while using the median HJD for each epoch. The format is the same as in Fig. D.1.

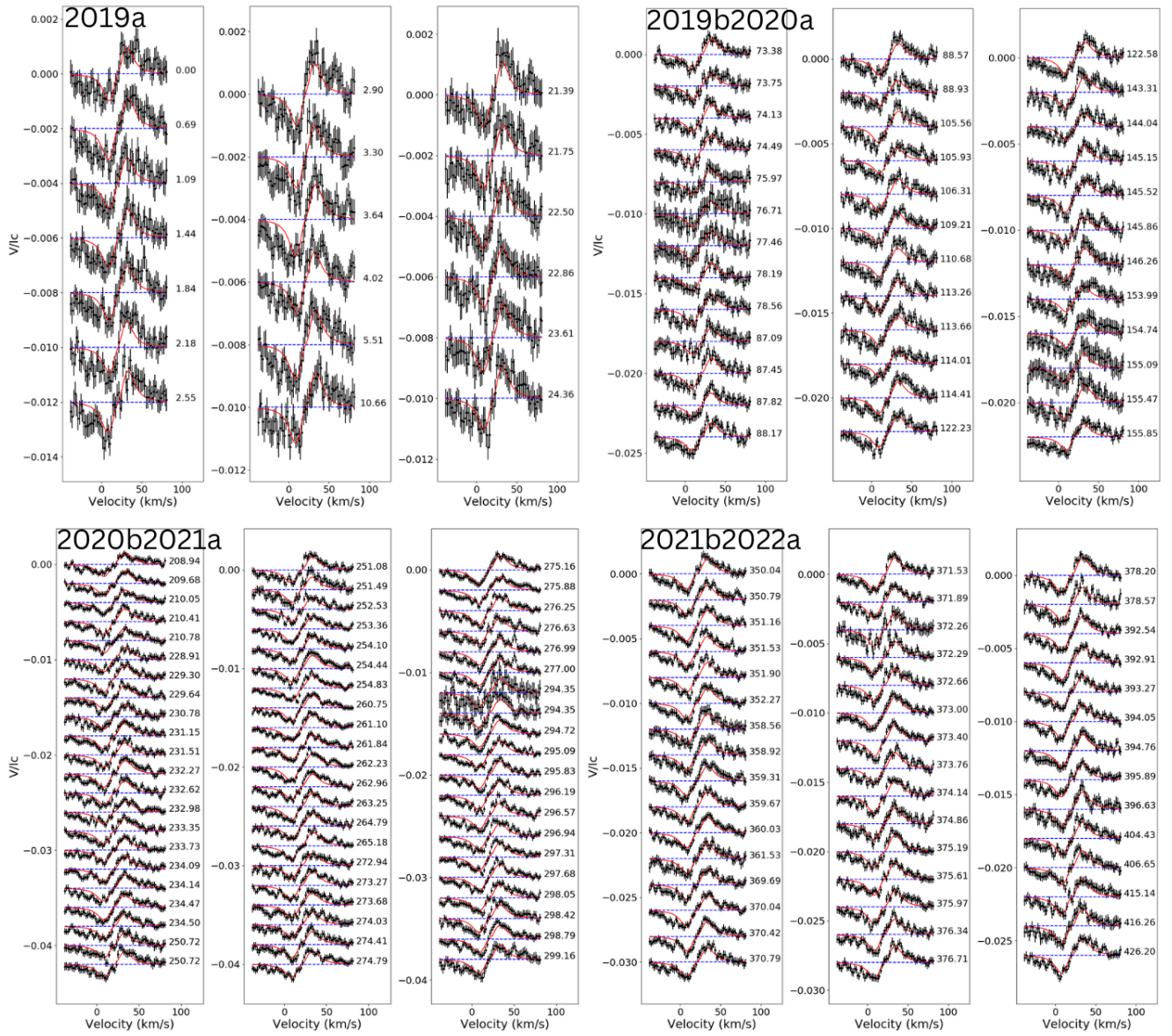


Fig. D.3. SPIRou time series of Stokes V profiles of CN Leo. Top left: 2019a. Top right: 2019b2020a. Bottom left: 2020b2021a. Bottom right: 2021b2022a. The format is the same as in Fig. D.1.

Appendix E: Observing log

This appendix lists the spectropolarimetric observations of EV Lac, DS Leo and CN Leo collected with ESPaDOnS, Nar-

val and SPIRou. Tables with longitudinal magnetic field values analysed in Sec. 3 are also provided.

Table E.1. EV Lac observations collected with SPIRou. The columns are: (1 and 2) date and universal time of the observations, (3) heliocentric Julian date, (4) rotational cycle of the observations found using Eq. (3), (5) exposure time of a polarimetric sequence, (6) signal-to-noise ratio at 1650 nm per polarimetric sequence, (7) RMS noise level of Stokes V signal in units of unpolarised continuum.

Date	UT [hh:mm:ss]	HJD [-2450000]	n_{cyc}	t_{exp} [s]	S/N	σ_{LSD} [$10^{-4}I_c$]
2019						
September 11	13:55:51.10	8738.0805	0.00	4x61	177	1.5
September 18	9:14:04.52	8744.8848	1.56	4x61	258	1.5
September 19	8:18:23.93	8745.8461	1.78	4x61	273	1.6
September 20	11:55:01.36	8746.9965	2.04	4x61	219	1.8
September 24	8:10:20.29	8750.8405	2.93	4x61	277	1.5
September 25	10:26:04.22	8751.9348	3.18	4x61	274	1.5
September 26	8:19:18.57	8752.8467	3.39	4x61	279	1.8
October 02	8:44:59.95	8758.8646	4.77	4x61	208	1.8
October 05	8:01:27.77	8761.8343	5.45	4x61	271	1.8
October 06	7:41:48.50	8762.8207	5.67	4x61	279	2.0
October 07	10:11:10.32	8763.9244	5.93	4x61	235	1.8
October 09	9:39:22.98	8765.9023	6.38	4x61	262	1.6
October 12	10:46:51.96	8768.9492	7.08	4x61	237	1.6
October 14	8:56:36.72	8770.8726	7.52	4x61	248	1.6
October 16	8:59:26.66	8772.8746	7.98	4x61	240	1.6
October 31	8:22:51.21	8787.8492	11.41	4x61	192	1.7
November 01	8:45:36.02	8788.8650	11.65	4x61	222	1.3
November 02	7:17:00.73	8789.8035	11.86	4x61	242	1.5
November 03	8:05:36.05	8790.8372	12.10	4x61	217	1.6
November 04	7:12:06.27	8791.8001	12.32	4x61	167	2.1
November 05	10:10:50.67	8792.9242	12.58	4x61	214	1.7
November 07	8:39:07.45	8794.8605	13.02	4x61	196	1.9
November 09	8:40:23.42	8796.8614	13.48	4x61	213	1.8
November 10	9:19:14.54	8797.8884	13.72	4x61	208	1.9
November 11	9:11:19.59	8798.8829	13.95	4x61	171	2.0
November 12	7:45:35.45	8799.8233	14.16	4x61	232	1.7
November 13	8:19:17.48	8800.8467	14.40	4x61	206	1.7
November 14	7:44:47.84	8801.8228	14.62	4x61	230	1.8
December 05	6:51:09.99	8822.7855	19.43	4x61	188	1.9
December 08	7:17:20.12	8825.8037	20.12	4x61	220	1.7
December 09	7:39:53.15	8826.8194	20.35	4x61	204	2.1
December 10	6:23:03.35	8827.7660	20.57	4x61	221	1.8
December 11	6:43:05.45	8828.7799	20.80	4x61	244	1.6
December 12	5:41:28.65	8829.7371	21.02	4x61	265	1.5
December 13	6:46:22.38	8830.7822	21.26	4x61	229	1.6
2020						
July 27	14:59:58.04	9058.1250	73.40	4x61	238	1.5
July 29	11:20:47.34	9059.9728	73.83	4x61	259	1.3
July 30	11:14:11.73	9060.9682	74.06	4x61	257	1.3
July 31	14:56:34.88	9062.1226	74.32	4x61	245	1.3
August 01	11:55:22.15	9062.9968	74.52	4x61	267	1.5
August 02	11:19:59.63	9063.9722	74.75	4x61	265	1.4
August 03	12:13:13.60	9065.0092	74.98	4x61	261	1.3
August 04	10:42:02.97	9065.9459	75.20	4x61	281	1.5
August 06	12:38:28.82	9068.0267	75.68	4x61	139	2.3
August 06	12:44:56.78	9068.0312	75.68	4x61	129	2.2
August 08	12:36:54.83	9070.0256	76.13	4x61	182	1.9
August 09	13:04:12.53	9071.0446	76.37	4x61	229	1.5
August 10	12:26:01.62	9072.0181	76.59	4x61	276	1.4
August 11	13:28:42.14	9073.0616	76.83	4x61	270	1.2

Table E.1. Continued.

Date	UT [hh:mm:ss]	HJD [-2450000]	n_{cyc}	t_{exp} [s]	S/N	σ_{LSD} [$10^{-4}I_c$]
August 26	11:49:46.00	9087.9929	80.26	4x61	227	1.5
August 27	11:20:50.23	9088.9728	80.48	4x61	262	1.5
August 28	10:03:49.00	9089.9193	80.70	4x61	305	1.4
August 29	12:07:39.46	9091.0053	80.95	4x61	279	1.2
August 30	12:10:25.30	9092.0072	81.18	4x61	240	1.4
August 31	11:56:19.84	9092.9975	81.40	4x61	284	1.3
September 01	10:23:01.42	9093.9327	81.62	4x61	283	1.3
September 02	10:16:13.69	9094.9279	81.85	4x61	285	1.2
September 03	12:27:38.73	9096.0192	82.10	4x61	277	1.4
September 04	12:28:09.24	9097.0196	82.33	4x61	270	1.6
September 05	12:12:24.68	9098.0086	82.55	4x61	233	1.4
September 06	11:50:38.31	9098.9935	82.78	4x61	253	1.3
September 08	10:55:48.32	9100.9554	83.23	4x61	285	1.2
September 09	10:11:06.99	9101.9244	83.45	4x61	297	1.6
September 10	10:13:11.62	9102.9258	83.68	4x61	299	1.3
September 18	9:25:02.88	9110.8924	85.51	4x61	255	1.5
September 19	10:05:48.40	9111.9207	85.74	4x61	194	1.7
September 20	11:48:32.60	9112.9920	85.99	4x61	288	1.3
September 21	8:20:51.79	9113.8478	86.19	4x61	216	1.7
September 22	8:35:31.66	9114.8580	86.42	4x61	281	1.2
September 23	8:13:19.93	9115.8426	86.64	4x61	277	1.6
September 25	9:15:08.47	9117.8855	87.11	4x61	313	1.4
September 26	7:33:25.24	9118.8149	87.32	4x61	246	1.4
September 27	7:42:07.90	9119.8209	87.56	4x61	306	1.5
September 28	7:41:26.06	9120.8204	87.78	4x61	306	1.4
September 29	7:38:29.25	9121.8184	88.01	4x61	304	1.4
September 30	8:40:14.19	9122.8613	88.25	4x61	299	1.2
October 01	9:45:52.92	9123.9069	88.49	4x61	261	1.4
October 03	8:12:28.39	9125.8420	88.94	4x61	256	1.5
October 04	8:57:10.35	9126.8730	89.17	4x61	280	1.5
October 05	8:29:39.33	9127.8539	89.40	4x61	270	1.5
October 06	10:31:49.98	9128.9388	89.65	4x61	267	1.4
October 07	8:22:05.70	9129.8487	89.86	4x61	305	1.2
November 01	8:15:35.26	9154.8442	95.59	4x61	307	1.4
November 03	9:05:33.11	9156.8789	96.05	4x61	313	1.1
November 04	8:50:23.57	9157.8683	96.28	4x61	280	1.3
November 05	6:47:10.96	9158.7828	96.49	4x61	307	1.4
December 24	6:12:25.23	9207.7586	107.72	4x61	292	1.4
December 25	4:53:19.85	9208.7037	107.94	4x61	286	1.3
December 26	5:33:37.73	9209.7317	108.18	4x61	299	1.2
December 29	6:13:56.63	9212.7597	108.87	4x61	254	1.3
December 30	4:44:03.71	9213.6973	109.09	4x61	237	1.4
December 31	5:48:42.91	9214.7422	109.33	4x61	261	1.6
2022						
January 01	4:37:16.34	9215.6925	109.54	4x61	253	1.6
January 02	5:09:55.69	9216.7152	109.78	4x61	269	1.3
January 03	5:47:29.85	9217.7413	110.01	4x61	278	1.3
January 04	5:00:26.60	9218.7086	110.24	4x61	291	1.2
January 05	5:17:26.10	9219.7204	110.47	4x61	261	1.4
January 06	5:01:25.17	9220.7093	110.69	4x61	289	1.3
January 07	5:21:18.80	9221.7231	110.93	4x61	275	1.5
January 07	6:08:01.35	9221.7556	110.93	4x61	257	1.3
January 08	5:29:10.80	9222.7286	111.16	4x61	251	1.4
January 08	6:17:39.99	9222.7623	111.17	4x61	272	1.3
June 20	12:20:33.62	9386.0143	148.61	4x61	300	1.4
June 21	12:09:03.29	9387.0063	148.84	4x61	253	1.4
June 22	10:34:16.22	9387.9405	149.05	4x61	170	3.2
June 22	10:40:11.40	9387.9446	149.05	4x61	133	2.8
June 23	12:19:50.11	9389.0138	149.30	4x61	311	1.1

Table E.1. Continued.

Date	UT [hh:mm:ss]	HJD [−2450000]	n_{cyc}	t_{exp} [s]	S/N	σ_{LSD} [$10^{-4}I_c$]
June 24	13:12:53.35	9390.0506	149.53	4x61	287	1.5
June 25	13:02:56.56	9391.0437	149.76	4x61	285	1.8
June 26	13:28:16.27	9392.0613	150.00	4x61	308	1.4
June 27	13:07:23.34	9393.0468	150.22	4x61	324	1.3
June 28	13:48:12.59	9394.0751	150.46	4x61	292	1.4
June 29	12:23:06.45	9395.0160	150.67	4x61	304	1.6
June 30	14:57:58.81	9396.1236	150.93	4x61	248	1.4
July 01	12:53:56.69	9397.0375	151.14	4x61	266	1.4
July 02	12:38:58.59	9398.0271	151.36	4x61	280	1.3
July 17	13:01:17.98	9413.0426	154.81	4x61	222	1.4
July 18	12:56:59.07	9414.0396	155.04	4x61	244	1.6
July 19	10:45:04.51	9414.9480	155.24	4x61	255	1.8
July 20	12:29:36.88	9416.0206	155.49	4x61	305	1.3
July 21	13:44:44.47	9417.0727	155.73	4x61	276	1.4
July 25	14:01:52.56	9421.0846	156.65	4x61	201	2.1
July 27	13:32:52.79	9423.0645	157.11	4x61	280	1.3
August 13	12:41:46.76	9440.0290	161.00	4x61	293	1.4
August 14	9:26:02.95	9440.8931	161.20	4x61	302	1.3
August 15	8:41:13.87	9441.8620	161.42	4x61	301	1.2
August 16	8:27:44.94	9442.8526	161.64	4x61	305	1.3
August 17	9:59:38.41	9443.9164	161.89	4x61	275	1.4
August 18	12:25:00.60	9445.0174	162.14	4x61	312	1.3
August 19	7:49:01.33	9445.8257	162.33	4x61	303	1.2
August 20	9:48:31.18	9446.9087	162.58	4x61	194	2.0
August 21	10:45:00.86	9447.9479	162.81	4x61	220	1.7
August 22	10:23:55.51	9448.9333	163.04	4x61	277	1.5
August 23	9:57:29.39	9449.9149	163.26	4x61	308	1.4
August 24	13:07:34.34	9451.0469	163.52	4x61	255	1.6
August 25	9:05:11.93	9451.8786	163.72	4x61	286	1.3
August 26	8:53:03.17	9452.8702	163.94	4x61	309	1.3
September 15	9:41:58.73	9472.9042	168.54	4x61	304	1.4
September 17	9:37:52.17	9474.9013	169.00	4x61	308	1.2
September 18	8:05:34.97	9475.8372	169.21	4x61	323	1.3
September 19	7:42:11.87	9476.8210	169.44	4x61	310	1.0
September 20	8:37:10.74	9477.8592	169.67	4x61	316	1.3
September 21	8:14:05.06	9478.8431	169.90	4x61	259	1.4
September 22	8:09:20.14	9479.8398	170.13	4x61	328	1.3
September 23	7:50:05.57	9480.8265	170.35	4x61	322	1.3
September 24	7:57:29.68	9481.8316	170.59	4x61	327	1.4
October 15	7:00:00.33	9502.7917	175.39	4x61	329	1.2
October 16	7:58:44.35	9503.8325	175.63	4x61	306	1.4
October 17	7:39:54.74	9504.8194	175.86	4x61	265	1.3
October 19	11:41:55.58	9506.9874	176.35	4x61	317	1.3
October 20	7:14:06.57	9507.8015	176.54	4x61	292	1.3
October 21	8:04:58.67	9508.8368	176.78	4x61	277	1.5
October 22	6:47:00.27	9509.7826	177.00	4x61	260	1.6
October 23	7:23:28.60	9510.8080	177.23	4x61	302	1.1
October 24	8:28:04.13	9511.8528	177.47	4x61	261	1.6
October 25	6:06:35.30	9512.7546	177.68	4x61	300	1.3
October 26	7:02:29.73	9513.7934	177.92	4x61	305	1.2
October 27	9:46:41.47	9514.9074	178.17	4x61	295	1.1
November 19	6:45:55.17	9537.7819	183.42	4x61	309	1.2
November 20	6:27:30.27	9538.7691	183.64	4x61	286	1.1
November 21	6:25:45.70	9539.7679	183.87	4x61	240	1.4
November 22	7:03:53.33	9540.7944	184.11	4x61	177	2.4

Table E.2. DS Leo observations collected with SPIRou. The columns are the same as in Table E.1.

Date	UT [hh:mm:ss]	HJD [−2450000]	n_{cyc}	t_{exp} [s]	S/N	σ_{LSD} [$10^{-4}I_c$]
2020						
November 04	14:41:01.65	9158.1132	0.00	4x66	242	1.3
November 05	14:32:49.50	9159.1076	0.07	4x66	248	1.3
December 24	13:11:16.12	9208.0545	3.59	4x55	250	1.5
December 25	14:26:36.37	9209.1069	3.67	4x66	255	1.4
December 26	12:54:42.75	9210.0431	3.73	4x83	221	1.4
December 29	14:46:25.61	9213.1208	3.95	4x83	172	2.0
December 30	14:48:29.36	9214.1222	4.03	4x78	241	1.5
December 31	14:11:29.98	9215.0966	4.10	4x61	246	1.4
2021						
January 02	15:25:19.11	9217.1479	4.24	4x83	249	1.5
January 03	13:41:59.49	9218.0762	4.31	4x61	251	1.3
January 04	13:10:27.14	9219.0543	4.38	4x61	250	1.5
January 05	13:00:23.34	9220.0473	4.45	4x66	243	1.4
January 06	13:57:54.22	9221.0873	4.53	4x61	249	1.3
January 07	14:05:48.84	9222.0928	4.60	4x61	247	1.3
January 08	14:15:30.20	9223.0996	4.67	4x66	243	1.4
February 21	11:23:11.74	9266.9790	7.83	4x72	234	1.5
February 22	12:44:47.36	9268.0356	7.90	4x72	250	1.5
February 23	14:13:45.11	9269.0974	7.98	4x72	113	3.5
February 23	14:56:45.73	9269.1272	7.98	4x72	206	1.6
February 26	10:15:48.22	9271.9320	8.18	4x72	269	1.3
February 28	14:29:34.27	9274.1081	8.34	4x72	280	1.0
March 02	14:02:39.82	9276.0892	8.48	4x72	235	1.5
March 03	12:08:50.87	9277.0101	8.55	4x72	240	1.3
March 04	13:42:07.40	9278.0748	8.62	4x72	285	1.2
March 20	12:54:55.01	9294.0409	9.77	4x72	275	1.2
March 21	11:56:28.50	9295.0002	9.84	4x72	232	1.5
March 22	13:26:55.90	9296.0629	9.92	4x72	224	1.5
March 23	11:52:40.55	9296.9974	9.98	4x72	273	1.1
March 24	13:02:40.05	9298.0459	10.06	4x72	277	1.3
March 26	12:24:48.47	9300.0194	10.20	4x72	175	2.0
March 27	7:03:51.09	9300.7965	10.26	4x72	233	1.3
March 31	11:11:31.74	9304.9681	10.56	4x72	252	1.4
April 01	12:19:51.08	9306.0155	10.63	4x72	269	1.2
April 22	10:49:28.41	9326.9507	12.14	4x72	246	1.5
April 23	8:52:58.20	9327.8698	12.20	4x72	269	1.4
April 24	10:56:14.16	9328.9553	12.28	4x72	241	1.5
April 25	9:52:11.19	9329.9107	12.35	4x72	173	1.8
April 26	10:03:37.95	9330.9185	12.42	4x72	157	2.5
April 26	10:52:46.47	9330.9527	12.43	4x72	183	2.8
April 27	11:01:16.31	9331.9585	12.50	4x72	240	1.4
April 28	10:58:29.76	9332.9564	12.57	4x72	257	1.2
April 30	10:17:36.74	9334.9279	12.71	4x72	280	1.2
May 01	10:26:10.76	9335.9337	12.78	4x72	261	1.4
May 02	10:13:59.09	9336.9252	12.86	4x72	224	1.7
May 03	9:56:11.36	9337.9127	12.93	4x72	234	1.3
June 19	6:32:04.07	9384.7675	16.29	4x72	182	1.6
June 19	6:38:49.98	9384.7722	16.29	4x72	171	1.7
June 20	6:32:32.52	9385.7677	16.37	4x72	241	1.3
June 21	6:27:02.17	9386.7639	16.44	4x72	280	1.4
June 23	6:00:08.67	9388.7451	16.58	4x72	258	1.3
June 24	5:57:16.62	9389.7431	16.65	4x72	283	1.2
June 25	6:06:01.63	9390.7491	16.72	4x72	235	1.4
June 26	5:57:21.88	9391.7430	16.80	4x72	293	1.3
June 27	5:59:26.04	9392.7444	16.87	4x72	286	1.5
June 28	6:02:42.25	9393.7467	16.94	4x72	295	1.4
June 29	5:56:45.44	9394.7425	17.01	4x72	242	1.6
June 30	5:58:09.69	9395.7435	17.08	4x72	220	1.6
July 01	5:58:11.25	9396.7434	17.16	4x72	241	1.6
July 02	5:57:49.39	9397.7432	17.23	4x72	195	2.0
July 17	5:56:11.39	9412.7417	18.31	4x72	271	1.3
July 19	5:46:33.47	9414.7350	18.45	4x72	239	1.4

Table E.2. Continued.

Date	UT [hh:mm:ss]	HJD [-2450000]	n_{cyc}	t_{exp} [s]	S/N	σ_{LSD} [$10^{-4}I_c$]
November 16	15:08:48.28	9535.1336	27.10	4x72	273	1.3
November 17	15:38:53.47	9536.1546	27.18	4x72	236	1.3
November 18	15:01:36.89	9537.1288	27.25	4x72	280	1.3
November 19	15:34:03.76	9538.1514	27.32	4x72	302	1.1
November 20	15:17:58.29	9539.1403	27.39	4x72	260	1.3
November 20	15:55:15.68	9539.1662	27.39	4x72	273	1.4
November 21	15:10:49.20	9540.1354	27.46	4x72	278	1.4
November 22	14:53:39.28	9541.1236	27.53	4x72	293	1.2
December 09	15:17:03.16	9558.1411	28.76	4x72	284	1.3
December 10	14:49:25.95	9559.1219	28.83	4x72	233	1.5
December 11	15:49:49.61	9560.1639	28.90	4x72	217	1.4
December 13	14:59:58.41	9562.1294	29.05	4x72	287	1.1
December 15	14:37:49.46	9564.1142	29.19	4x72	256	1.4
December 17	15:55:58.97	9566.1686	29.34	4x72	203	2.0
December 18	15:05:25.50	9567.1335	29.40	4x72	248	1.5
2022						
January 06	15:05:19.45	9586.1341	30.77	4x72	265	1.3
January 08	15:34:42.78	9588.1546	30.92	4x72	279	1.3
January 09	14:22:30.48	9589.1044	30.98	4x72	291	1.3
January 10	15:03:28.46	9590.1329	31.06	4x72	295	1.3
January 12	16:22:44.45	9592.1880	31.21	4x72	263	1.3
January 13	14:39:32.63	9593.1163	31.27	4x72	250	1.4
January 14	14:23:12.69	9594.1050	31.34	4x72	285	1.1
January 15	16:16:39.50	9595.1838	31.42	4x72	261	1.3
January 16	14:47:37.30	9596.1219	31.49	4x72	163	1.9
January 17	15:00:18.40	9597.1307	31.56	4x72	263	1.2
January 18	16:06:47.82	9598.1769	31.64	4x72	288	1.4
January 19	16:21:07.15	9599.1869	31.71	4x72	277	1.2
January 20	16:11:30.66	9600.1802	31.78	4x72	277	1.4
January 22	15:03:23.65	9602.1329	31.92	4x72	193	1.7
January 24	15:01:19.06	9604.1314	32.06	4x72	295	1.2
January 25	15:30:10.81	9605.1515	32.14	4x72	266	1.2
January 26	14:25:07.09	9606.1063	32.21	4x72	277	1.4
January 31	14:50:19.86	9611.1237	32.57	4x72	265	1.3
February 01	15:01:09.68	9612.1312	32.64	4x72	150	2.1
February 01	15:08:29.53	9612.1363	32.64	4x72	162	1.8
March 11	8:48:01.68	9649.8702	35.35	4x72	292	1.1
March 12	10:53:43.46	9650.9574	35.43	4x72	256	1.2
March 13	11:22:40.32	9651.9774	35.50	4x72	288	1.3
March 14	8:28:17.21	9652.8562	35.57	4x72	295	1.2
March 15	12:22:54.90	9654.0191	35.65	4x72	286	1.1
March 16	13:16:17.50	9655.0560	35.73	4x72	251	1.3
March 17	11:09:30.70	9655.9679	35.79	4x72	267	1.5
March 18	13:20:13.72	9657.0586	35.87	4x72	218	1.6
March 19	13:06:09.07	9658.0488	35.94	4x72	270	1.3
March 20	11:47:25.79	9658.9940	36.01	4x72	293	1.2
March 22	11:42:33.77	9660.9905	36.15	4x72	244	1.5
March 23	11:05:20.41	9661.9645	36.22	4x72	102	1.2
March 23	11:55:50.39	9661.9996	36.22	4x72	275	1.2
April 09	11:37:18.90	9678.9852	37.45	4x72	271	1.4
April 12	11:20:02.08	9681.9729	37.66	4x72	265	1.4
April 13	11:46:22.06	9682.9911	37.73	4x72	267	1.3
April 14	12:06:31.61	9684.0050	37.81	4x72	172	2.1
April 15	11:32:16.57	9684.9812	37.88	4x72	266	1.5
April 18	11:33:35.81	9687.9818	38.09	4x72	262	1.4
April 19	11:06:39.63	9688.9630	38.16	4x72	262	1.2
April 20	10:47:12.72	9689.9494	38.23	4x72	281	1.3
April 21	10:45:48.61	9690.9483	38.31	4x72	289	1.3
May 11	9:35:49.87	9710.8979	39.74	4x72	247	1.4
May 12	9:47:34.23	9711.9059	39.81	4x72	245	1.4
May 13	9:11:53.37	9712.8811	39.88	4x72	235	1.4
May 16	8:31:03.28	9715.8525	40.10	4x72	267	1.5
May 17	8:38:05.11	9716.8573	40.17	4x72	285	1.4
June 02	6:33:44.50	9732.7697	41.31	4x72	280	1.3
June 03	6:29:45.48	9733.7668	41.38	4x72	273	1.3
June 05	6:38:13.26	9735.7726	41.53	4x72	277	1.2
June 06	8:16:18.89	9736.8406	41.61	4x72	262	1.4
June 08	6:00:13.71	9738.7460	41.74	4x72	266	1.4
June 09	6:01:26.80	9739.7468	41.81	4x72	281	1.2
June 10	7:06:39.01	9740.7920	41.89	4x72	278	1.2

Table E.3. CN Leo observations collected with SPIRou. The columns are the same as in Table E.1.

Date	UT [hh:mm:ss]	HJD [-2450000]	n_{cyc}	t_{exp} [s]	S/N	σ_{LSD} [$10^{-4} I_c$]
2019						
April 16	12:13:42.22	8590.0095	22.56	4x128	176	2.5
April 18	9:09:19.88	8591.8815	23.25	4x117	171	2.8
April 19	10:44:28.81	8592.9476	23.65	4x128	163	2.8
April 20	9:35:28.57	8593.8996	24.00	4x128	171	2.7
April 21	11:35:37.16	8594.9831	24.40	4x128	170	2.8
April 22	9:19:34.48	8595.8886	24.74	4x111	172	2.6
April 23	9:33:44.59	8596.8984	25.11	4x111	172	2.7
April 24	8:19:40.68	8597.8470	25.46	4x111	174	2.7
April 25	9:49:38.88	8598.9095	25.86	4x105	173	2.9
April 26	8:22:17.22	8599.8488	26.20	4x128	192	2.5
April 27	8:25:34.09	8600.8511	26.58	4x128	175	2.4
May 01	9:09:09.90	8604.8814	28.07	4x117	171	2.7
May 15	6:56:10.26	8618.7890	33.22	4x83	172	2.7
June 13	6:21:17.73	8647.7648	43.95	4x72	170	2.6
June 14	5:53:42.23	8648.7456	44.31	4x66	173	2.6
June 16	6:04:10.29	8650.7529	45.06	4x83	179	2.7
June 17	5:47:17.17	8651.7412	45.42	4x89	173	2.4
June 19	6:03:42.60	8653.7526	46.17	4x89	178	2.8
June 21	6:26:25.16	8655.7683	46.92	4x105	175	2.4
October 31	15:11:53.11	8788.1333	95.94	4x128	214	1.9
November 01	15:29:15.11	8789.1453	96.31	4x128	184	2.2
November 02	15:44:00.94	8790.1556	96.69	4x128	214	2.2
November 03	15:03:29.07	8791.1274	97.05	4x128	204	2.2
November 07	15:23:03.22	8795.1410	98.53	4x128	175	2.5
November 09	14:49:54.88	8797.1180	99.27	4x128	155	2.7
November 11	15:43:55.63	8799.1555	100.02	4x128	171	2.9
November 13	14:54:25.58	8801.1211	100.75	4x105	233	2.1
November 14	14:48:53.61	8802.1173	101.12	4x105	232	2.4
December 07	15:35:36.87	8825.1497	109.65	4x128	196	2.2
December 08	14:55:34.82	8826.1219	110.01	4x117	228	2.2
December 09	14:45:15.59	8827.1148	110.38	4x117	229	2.0
December 10	13:54:07.22	8828.0792	110.73	4x117	235	2.4
December 11	15:20:36.69	8829.1393	111.13	4x117	229	2.1
December 12	14:56:48.41	8830.1228	111.49	4x128	229	2.1
2020						
January 26	12:28:07.86	8875.0195	128.12	4x111	233	2.3
January 27	12:23:43.97	8876.0165	128.49	4x117	230	2.2
January 28	13:14:47.18	8877.0519	128.87	4x128	219	2.0
February 05	8:54:48.40	8884.8714	131.77	4x111	228	2.1
February 09	8:19:52.83	8888.8471	133.24	4x128	182	2.5
February 16	7:47:00.30	8895.8243	135.82	4x111	227	2.1
February 17	9:28:00.93	8896.8945	136.22	4x128	206	2.2
February 18	7:46:31.47	8897.8240	136.57	4x128	229	2.0
February 19	10:11:34.85	8898.9247	136.97	4x105	233	2.2
March 11	12:52:11.14	8920.0362	144.79	4x111	233	1.8
March 12	11:12:15.25	8920.9668	145.14	4x100	236	2.2
May 07	10:50:12.93	8976.9515	165.87	4x128	218	2.2
May 09	9:49:53.90	8978.9097	166.60	4x111	231	2.0
May 12	9:47:44.18	8981.9082	167.71	4x128	222	2.1
May 13	9:52:29.17	8982.9114	168.08	4x100	231	2.2
May 14	7:54:40.23	8983.8296	168.42	4x94	229	1.9
May 15	9:57:54.46	8984.9152	168.82	4x128	196	2.3
June 05	6:51:51.44	9005.7860	176.55	4x128	197	2.1
June 07	7:06:16.26	9007.7960	177.30	4x128	175	2.7
June 08	6:17:14.27	9008.7620	177.65	4x128	179	3.2
June 09	6:43:04.47	9009.7799	178.03	4x128	174	2.6
June 10	7:04:25.72	9010.7947	178.41	4x128	230	1.9
October 31	15:20:34.06	9154.1393	231.50	4x111	226	2.1
November 02	15:34:13.01	9156.1488	232.24	4x128	211	2.1
November 03	15:43:02.82	9157.1549	232.61	4x89	225	2.1
November 04	14:48:35.82	9158.1171	232.97	4x83	222	2.3
November 05	14:39:48.09	9159.1110	233.34	4x78	220	2.3
December 24	13:17:50.80	9208.0541	251.47	4x78	228	2.2
December 25	14:34:01.34	9209.1070	251.86	4x83	225	2.4
December 26	13:02:53.07	9210.0437	252.20	4x117	223	2.4
December 29	14:57:23.81	9213.1232	253.34	4x128	158	2.5
December 30	14:59:32.48	9214.1247	253.71	4x128	223	2.4
December 31	14:19:08.41	9215.0966	254.07	4x100	226	2.4

Table E.3. Continued.

Date	UT [hh:mm:ss]	HJD [-2450000]	n_{cyc}	t_{exp} [s]	S/N	σ_{LSD} [$10^{-4} I_c$]
2021						
January 02	15:33:42.40	9217.1484	254.83	4x111	222	2.3
January 03	13:49:08.56	9218.0758	255.18	4x78	223	2.2
January 04	13:17:16.19	9219.0537	255.54	4x78	226	2.2
January 05	13:07:42.22	9220.0470	255.91	4x83	220	2.3
January 06	14:05:29.70	9221.0871	256.29	4x89	222	2.1
January 07	13:34:08.29	9222.0654	256.65	4x94	225	2.2
January 07	16:17:06.35	9222.1785	256.70	4x100	220	2.5
January 08	13:41:17.96	9223.0703	257.03	4x100	225	2.6
January 08	16:03:57.25	9223.1694	257.06	4x105	222	2.3
February 21	10:53:47.13	9266.9540	273.28	4x111	165	2.8
February 21	11:04:02.34	9266.9611	273.28	4x111	188	2.5
February 22	10:05:46.91	9267.9207	273.64	4x100	226	2.3
February 23	12:41:09.81	9269.0286	274.05	4x111	203	2.5
February 26	8:09:09.92	9271.8397	275.09	4x111	245	2.4
February 28	14:12:09.33	9274.0918	275.92	4x111	275	2.1
March 02	13:44:02.27	9276.0722	276.66	4x111	238	2.4
March 03	11:50:58.30	9276.9937	277.00	4x111	254	2.1
March 04	13:32:04.78	9278.0639	277.40	4x111	276	2.0
March 20	12:37:22.22	9294.0260	283.31	4x111	269	1.9
March 21	11:38:33.18	9294.9851	283.66	4x111	240	2.2
March 23	11:30:39.62	9296.9796	284.40	4x111	261	2.1
March 24	12:44:32.17	9298.0309	284.79	4x111	263	2.1
March 26	11:52:50.95	9299.9950	285.52	4x111	247	2.3
March 27	6:45:37.02	9300.7817	285.81	4x111	248	2.1
March 31	10:54:04.65	9304.9542	287.35	4x111	219	2.4
April 01	12:02:33.87	9306.0018	287.74	4x111	254	2.1
April 22	10:28:06.67	9326.9362	295.50	4x111	187	2.3
April 23	7:56:25.52	9327.8309	295.83	4x111	264	2.2
April 24	10:38:50.47	9328.9436	296.24	4x111	220	2.6
April 25	9:34:48.36	9329.8992	296.59	4x111	218	2.7
April 26	9:44:56.28	9330.9062	296.97	4x111	204	2.9
April 27	10:43:10.75	9331.9467	297.35	4x111	242	2.2
April 28	10:40:26.84	9332.9448	297.72	4x111	257	2.1
April 30	8:57:35.34	9334.8733	298.44	4x111	269	2.0
May 01	9:25:34.23	9335.8928	298.81	4x111	266	2.1
May 02	9:55:38.98	9336.9136	299.19	4x111	201	2.5
May 03	9:26:51.13	9337.8936	299.55	4x111	136	2.5
May 03	9:36:37.40	9337.9004	299.56	4x111	207	2.5
June 19	6:03:13.60	9384.7522	316.91	4x111	141	4.2
June 19	6:12:45.43	9384.7589	316.91	4x111	132	3.0
June 20	6:15:05.26	9385.7605	317.28	4x111	245	2.2
June 21	6:09:04.48	9386.7563	317.65	4x111	277	2.1
June 23	5:41:33.33	9388.7372	318.39	4x111	269	2.1
June 24	5:38:03.01	9389.7348	318.75	4x111	249	2.2
June 25	5:49:08.47	9390.7425	319.13	4x111	241	2.3
June 26	5:46:41.96	9391.7408	319.50	4x111	247	2.4
June 27	5:46:00.34	9392.7403	319.87	4x111	284	2.1
June 28	5:44:57.25	9393.7396	320.24	4x111	287	2.2
June 29	5:38:28.52	9394.7351	320.61	4x111	244	2.7
June 30	5:39:01.55	9395.7354	320.98	4x111	207	2.8
July 01	5:39:05.12	9396.7355	321.35	4x111	239	2.2
July 02	5:39:06.12	9397.7355	321.72	4x111	156	3.2
November 16	14:51:17.17	9535.1189	372.60	4x111	258	1.9
November 18	15:09:21.21	9537.1315	373.35	4x111	252	2.1
November 19	15:41:46.14	9538.1540	373.72	4x111	292	2.0
November 20	15:25:28.03	9539.1427	374.09	4x111	269	2.2
November 21	15:18:29.94	9540.1378	374.46	4x111	270	1.9
November 22	15:01:19.45	9541.1259	374.83	4x111	251	2.0
December 09	14:43:38.22	9558.1136	381.12	4x111	169	2.2
December 10	14:16:08.87	9559.0945	381.48	4x111	197	2.4
December 11	15:16:43.27	9560.1366	381.87	4x111	239	2.6
December 12	14:49:26.03	9561.1177	382.23	4x111	270	2.0
December 13	14:19:35.10	9562.0969	382.59	4x111	281	2.1
December 17	15:21:34.66	9566.1400	384.09	4x111	221	2.2

Table E.3. Continued.

Date	UT [hh:mm:ss]	HJD [−2450000]	n_{cyc}	t_{exp} [s]	S/N	σ_{LSD} [$10^{-4}I_c$]
2022						
January 08	16:08:05.82	9588.1723	392.25	4x111	237	2.1
January 09	14:54:37.52	9589.1213	392.60	4x111	290	2.2
January 10	15:11:57.75	9590.1333	392.98	4x111	268	2.0
January 11	15:15:49.27	9591.1360	393.35	4x111	228	1.9
January 13	15:15:45.97	9593.1359	394.09	4x111	273	2.0
January 14	14:57:46.42	9594.1235	394.45	4x111	275	1.9
January 15	14:30:58.09	9595.1048	394.82	4x111	217	2.5
January 15	16:24:18.06	9595.1835	394.85	4x111	248	2.0
January 16	16:17:06.12	9596.1785	395.22	4x111	208	2.1
January 17	14:48:47.16	9597.1172	395.56	4x111	259	1.9
January 18	16:14:14.92	9598.1766	395.96	4x111	281	1.9
January 19	16:03:54.92	9599.1694	396.32	4x111	242	2.0
January 20	16:19:00.43	9600.1799	396.70	4x111	275	2.0
January 22	14:51:44.64	9602.1193	397.42	4x111	197	2.1
January 23	12:33:17.06	9603.0231	397.75	4x111	253	1.8
January 24	15:39:39.54	9604.1525	398.17	4x111	278	1.9
January 25	14:54:38.57	9605.1213	398.53	4x111	268	2.1
January 26	15:22:06.80	9606.1404	398.90	4x111	258	2.1
January 27	15:04:51.26	9607.1284	399.27	4x111	251	1.6
January 31	15:25:45.41	9611.1429	400.76	4x111	264	1.8
February 01	15:16:42.73	9612.1366	401.13	4x111	224	2.4
March 11	8:37:55.01	9649.8597	415.10	4x111	287	1.8
March 12	8:40:28.21	9650.8614	415.47	4x111	289	2.0
March 13	8:01:40.95	9651.8345	415.83	4x111	292	1.8
March 15	10:37:12.00	9653.9425	416.61	4x111	281	2.1
March 17	8:44:34.57	9655.8643	417.32	4x111	244	2.1
March 20	9:52:07.34	9658.9112	418.45	4x111	270	1.8
March 22	9:46:22.44	9660.9072	419.19	4x111	226	2.4
April 12	11:02:15.07	9681.9599	426.99	4x111	246	2.2
April 18	11:23:26.56	9687.9746	429.21	4x111	251	2.1
May 11	9:17:57.19	9710.8875	437.70	4x111	230	2.4
May 14	9:36:00.15	9713.9000	438.82	4x111	198	2.4
June 10	6:03:21.25	9740.7523	448.76	4x111	281	2.2

Table E.4. Optical and near-infrared measurements of longitudinal magnetic field for EV Lac. The columns are: (1) heliocentric Julian date of the observation, (2) B_l with formal error bar (see Eq. (4)), and (3) instrument used.

HJD [−2450000]	B_l [G]	Instrument
3569.1119	144.4±8.3	ESPaDOnS
3606.1478	−305.9±20.4	ESPaDOnS
3631.9065	23.9±9.4	ESPaDOnS
3631.9447	−106.2±11.0	ESPaDOnS
3631.9828	−82.9±9.6	ESPaDOnS
3953.0731	−529.5±20.6	ESPaDOnS
3955.0663	319.8±15.1	ESPaDOnS
3956.0600	−354.3±13.8	ESPaDOnS
3957.0597	−422.4±18.1	ESPaDOnS
3958.0723	−282.6±15.9	ESPaDOnS
3959.0728	290.1±15.0	ESPaDOnS
3960.0761	−161.0±15.2	ESPaDOnS
4986.5995	264.8±18.4	NARVAL
4994.6321	0.5±20.9	NARVAL
4995.5842	251.6±38.6	NARVAL
5059.3898	48.0±18.3	NARVAL
5370.5520	92.9±16.7	NARVAL
5384.6114	−49.5±13.4	NARVAL
5385.5601	−176.2±15.1	NARVAL
5388.5822	23.4±14.6	NARVAL
5390.5888	−203.6±25.4	NARVAL
5392.5938	−73.6±14.2	NARVAL
5396.5771	22.4±13.2	NARVAL
5401.5894	76.7±14.0	NARVAL
5402.5222	−87.1±14.5	NARVAL
5403.5208	−270.5±18.7	NARVAL
5411.5386	−194.8±15.6	NARVAL
5414.5135	93.9±14.1	NARVAL
5415.5838	−105.8±16.3	NARVAL
5416.5916	−297.6±16.2	NARVAL
5419.5954	−58.9±14.3	NARVAL
5420.5813	−306.3±19.1	NARVAL
5425.6210	−231.6±14.9	NARVAL
5426.5908	−143.6±14.6	NARVAL
5429.5743	−355.4±21.8	NARVAL
5430.6048	−168.5±16.1	NARVAL
7584.5642	−97.8±15.2	NARVAL
7585.5742	−107.6±20.7	NARVAL
7588.5683	5.1±13.9	NARVAL
7595.5856	−93.8±15.0	NARVAL
7608.4675	−61.2±15.2	NARVAL
7612.5894	−50.4±17.5	NARVAL
8738.0805	120.8±26.4	SPIRou
8744.8848	−151.5±22.6	SPIRou
8745.8461	47.1±22.6	SPIRou
8746.9965	57.1±28.9	SPIRou
8750.8405	130.8±21.0	SPIRou
8751.9348	−14.5±22.0	SPIRou
8752.8467	−82.0±21.9	SPIRou
8758.8646	−42.6±34.0	SPIRou
8761.8343	−71.1±22.1	SPIRou
8762.8207	−114.5±22.0	SPIRou
8763.9244	201.6±26.9	SPIRou
8765.9023	−23.3±22.3	SPIRou
8768.9492	64.0±24.4	SPIRou
8770.8726	−160.7±24.0	SPIRou
8772.8746	113.7±25.4	SPIRou

Table E.4. Continued.

HJD [−2450000]	B_l [G]	Instrument
8787.8492	−43.4±28.4	SPIRou
8788.8650	−171.5±22.8	SPIRou
8789.8035	121.3±21.6	SPIRou
8790.8372	82.6±23.3	SPIRou
8791.8001	18.3±29.9	SPIRou
8792.9242	−136.4±25.1	SPIRou
8794.8605	149.6±31.5	SPIRou
8796.8614	−126.4±34.2	SPIRou
8797.8884	−66.1±37.9	SPIRou
8798.8829	182.5±42.1	SPIRou
8799.8233	−57.3±29.1	SPIRou
8800.8467	−53.9±31.4	SPIRou
8801.8228	−101.7±31.7	SPIRou
8822.7855	−164.5±33.4	SPIRou
8825.8037	6.6±28.6	SPIRou
8826.8194	9.1±32.7	SPIRou
8827.7660	−205.7±29.1	SPIRou
8828.7799	−5.1±25.3	SPIRou
8829.7371	201.0±24.4	SPIRou
8830.7822	−30.8±28.0	SPIRou
9058.1250	−173.8±20.7	SPIRou
9059.9728	54.1±17.8	SPIRou
9060.9682	222.0±18.8	SPIRou
9062.1226	−45.8±18.8	SPIRou
9062.9968	−355.7±19.6	SPIRou
9063.9722	−119.3±18.8	SPIRou
9065.0092	175.9±18.9	SPIRou
9065.9459	119.8±18.6	SPIRou
9068.0267	−329.2±43.3	SPIRou
9068.0312	−293.3±42.1	SPIRou
9070.0256	206.8±30.3	SPIRou
9071.0446	−137.7±21.0	SPIRou
9072.0181	−381.7±19.1	SPIRou
9073.0616	21.9±16.9	SPIRou
9087.9929	−13.6±24.4	SPIRou
9088.9728	−315.0±19.7	SPIRou
9089.9193	−304.9±17.8	SPIRou
9091.0053	116.5±17.4	SPIRou
9092.0072	160.0±19.9	SPIRou
9092.9975	−237.8±17.2	SPIRou
9093.9327	−305.1±18.7	SPIRou
9094.9279	12.8±16.2	SPIRou
9096.0192	217.5±18.1	SPIRou
9097.0196	−95.4±18.3	SPIRou
9098.0086	−387.9±22.0	SPIRou
9098.9935	−92.1±18.3	SPIRou
9100.9554	71.0±17.0	SPIRou
9101.9244	−258.0±20.4	SPIRou
9102.9258	−273.3±18.2	SPIRou
9110.8924	−327.2±21.0	SPIRou
9111.9207	−166.5±26.8	SPIRou
9112.9920	137.9±18.2	SPIRou
9113.8478	184.2±25.4	SPIRou
9114.8580	−227.5±18.5	SPIRou
9115.8426	−338.7±19.5	SPIRou
9117.8855	254.0±18.3	SPIRou
9118.8149	−30.6±21.3	SPIRou

Table E.4. Continued.

HJD [−2450000]	B_l [G]	Instrument
9119.8209	−469.1±19.2	SPIRou
9120.8204	−94.8±18.3	SPIRou
9121.8184	191.1±18.3	SPIRou
9122.8613	82.0±17.2	SPIRou
9123.9069	−364.0±20.7	SPIRou
9125.8420	120.7±18.7	SPIRou
9126.8730	250.2±20.7	SPIRou
9127.8539	−223.5±18.6	SPIRou
9128.9388	−320.2±19.2	SPIRou
9129.8487	−8.8±17.2	SPIRou
9154.8442	−388.4±17.2	SPIRou
9156.8789	216.9±16.9	SPIRou
9157.8683	43.0±18.3	SPIRou
9158.7828	−323.0±17.3	SPIRou
9207.7586	−227.0±18.1	SPIRou
9208.7037	23.9±17.9	SPIRou
9209.7317	153.5±17.7	SPIRou
9212.7597	−15.4±20.3	SPIRou
9213.6973	136.5±22.7	SPIRou
9214.7422	−29.1±21.0	SPIRou
9215.6925	−355.8±21.3	SPIRou
9216.7152	−173.8±18.7	SPIRou
9217.7413	78.8±17.1	SPIRou
9218.7086	130.8±17.2	SPIRou
9219.7204	−293.7±19.6	SPIRou
9220.7093	−357.7±18.6	SPIRou
9221.7231	12.6±19.5	SPIRou
9221.7556	36.1±19.4	SPIRou
9222.7286	140.4±18.7	SPIRou
9222.7623	163.7±18.7	SPIRou
9386.0143	−370.1±17.9	SPIRou
9387.0063	−83.9±18.7	SPIRou
9387.9405	143.6±55.6	SPIRou
9387.9446	120.0±42.8	SPIRou
9389.0138	155.7±16.8	SPIRou
9390.0506	−314.4±19.2	SPIRou
9391.0437	−240.4±19.7	SPIRou
9392.0613	194.9±18.0	SPIRou
9393.0468	86.5±18.1	SPIRou
9394.0751	−180.9±17.8	SPIRou
9395.0160	−360.0±19.2	SPIRou
9396.1236	174.1±19.3	SPIRou
9397.0375	72.0±20.9	SPIRou
9398.0271	105.6±20.4	SPIRou
9413.0426	−174.6±20.2	SPIRou
9414.0396	216.1±24.3	SPIRou
9414.9480	171.8±28.5	SPIRou
9416.0206	−264.2±17.3	SPIRou

Table E.4. Continued.

HJD [−2450000]	B_l [G]	Instrument
9417.0727	−321.1±19.7	SPIRou
9421.0846	−442.5±28.9	SPIRou
9423.0645	177.7±17.9	SPIRou
9440.0290	249.7±18.8	SPIRou
9440.8931	104.1±17.2	SPIRou
9441.8620	−22.3±16.3	SPIRou
9442.8526	−455.8±20.0	SPIRou
9443.9164	82.2±18.8	SPIRou
9445.0174	112.8±18.5	SPIRou
9445.8257	167.7±17.7	SPIRou
9446.9087	−405.0±32.7	SPIRou
9447.9479	−164.1±24.4	SPIRou
9448.9333	259.2±19.3	SPIRou
9449.9149	111.8±18.2	SPIRou
9451.0469	−294.0±23.0	SPIRou
9451.8786	−367.3±19.4	SPIRou
9452.8702	194.3±16.7	SPIRou
9472.9042	−272.5±19.6	SPIRou
9474.9013	272.7±17.4	SPIRou
9475.8372	137.8±16.7	SPIRou
9476.8210	−9.3±16.3	SPIRou
9477.8592	−394.8±18.4	SPIRou
9478.8431	17.4±22.1	SPIRou
9479.8398	173.0±17.4	SPIRou
9480.8265	154.8±17.5	SPIRou
9481.8316	−340.5±18.2	SPIRou
9502.7917	104.2±16.0	SPIRou
9503.8325	−371.1±18.2	SPIRou
9504.8194	−106.2±18.7	SPIRou
9506.9874	85.4±16.6	SPIRou
9507.8015	−239.0±17.9	SPIRou
9508.8368	−242.1±19.3	SPIRou
9509.7826	226.4±21.8	SPIRou
9510.8080	87.4±17.0	SPIRou
9511.8528	−92.6±20.2	SPIRou
9512.7546	−363.7±17.6	SPIRou
9513.7934	28.4±16.6	SPIRou
9514.9074	129.1±17.7	SPIRou
9537.7819	−25.7±17.8	SPIRou
9538.7691	−330.5±18.8	SPIRou
9539.7679	−43.1±20.1	SPIRou
9540.7944	152.8±35.0	SPIRou

Table E.5. Optical and near-infrared measurements of longitudinal magnetic field for DS Leo. The columns are the same as in Table E.4.

HJD [−2450000]	B_l [G]	Instrument
3748.1023	4.7±5.9	ESPaDOnS
3748.9053	23.6±13.1	ESPaDOnS
3774.0359	9.8±6.0	ESPaDOnS
3781.1526	−7.9±9.1	ESPaDOnS
4126.6502	−16.5±8.9	NARVAL
4127.6349	−4.5±7.3	NARVAL
4128.6469	1.7±5.9	NARVAL
4129.6107	22.4±5.7	NARVAL
4130.6536	23.1±5.4	NARVAL
4133.6704	20.2±5.5	NARVAL
4134.6568	14.0±5.5	NARVAL
4135.6695	12.6±5.3	NARVAL
4136.6303	30.1±10.0	NARVAL
4462.6760	5.0±6.0	NARVAL
4463.7049	7.8±5.3	NARVAL
4465.7095	27.0±7.2	NARVAL
4466.7091	25.0±5.4	NARVAL
4468.7075	74.6±11.7	NARVAL
4472.6258	16.4±13.3	NARVAL
4473.6232	1.5±7.2	NARVAL
4484.5805	17.1±11.7	NARVAL
4485.5564	−6.5±10.5	NARVAL
4487.5839	−0.8±8.6	NARVAL
4489.5328	19.8±7.6	NARVAL
4491.5490	13.4±7.5	NARVAL
4492.5717	2.9±5.8	NARVAL
4493.5834	1.7±6.4	NARVAL
4499.6016	−10.8±6.8	NARVAL
4501.5834	6.5±7.7	NARVAL
4502.5820	12.2±6.0	NARVAL
4503.5804	4.3±6.2	NARVAL
4506.5933	18.7±6.1	NARVAL
4507.5570	6.3±5.7	NARVAL
4508.5856	29.6±6.3	NARVAL
4509.5907	28.6±6.7	NARVAL
4510.5857	27.9±8.4	NARVAL
4511.6026	−0.9±6.2	NARVAL
4512.5883	−0.5±6.8	NARVAL
4513.5876	−2.1±6.0	NARVAL
4862.6428	46.2±14.1	NARVAL
5266.4448	29.3±7.0	NARVAL
5268.4569	55.1±6.5	NARVAL
5269.4287	41.6±6.8	NARVAL
5270.5521	22.8±7.5	NARVAL
5271.5597	9.2±5.3	NARVAL
5272.5173	−5.3±11.5	NARVAL
5278.4970	−16.0±5.7	NARVAL
5284.4554	61.1±9.6	NARVAL
5292.4695	163.2±27.1	NARVAL
5293.3366	22.5±6.2	NARVAL
5295.5424	38.9±6.1	NARVAL
5296.4579	44.9±5.7	NARVAL
5297.3607	33.0±5.7	NARVAL
5302.5069	−10.0±5.9	NARVAL
5303.4522	−9.5±5.8	NARVAL
5304.3913	−17.4±5.6	NARVAL

Table E.5. Continued.

HJD [−2450000]	B_l [G]	Instrument
5310.3818	19.8±6.6	NARVAL
5311.4403	21.0±6.5	NARVAL
5312.3920	35.1±5.9	NARVAL
5586.5978	18.2±7.0	NARVAL
5587.5790	18.5±6.0	NARVAL
5588.5849	25.8±5.6	NARVAL
5589.5985	44.9±7.0	NARVAL
5593.5929	−3.9±6.1	NARVAL
5596.5681	−0.3±6.5	NARVAL
5597.5715	−0.8±5.4	NARVAL
5598.5820	18.2±6.3	NARVAL
6048.3494	−4.6±7.2	NARVAL
6050.3464	34.7±13.0	NARVAL
6084.3812	61.7±17.4	NARVAL
6092.3807	12.1±13.0	NARVAL
6093.3758	68.2±19.5	NARVAL
6094.3724	46.5±19.9	NARVAL
6095.3935	3.3±12.2	NARVAL
6100.3997	32.7±10.3	NARVAL
6101.3914	23.4±8.9	NARVAL
6102.4207	16.7±10.5	NARVAL
6103.4078	24.9±14.6	NARVAL
6667.6945	0.1±5.9	NARVAL
6669.6203	4.5±6.7	NARVAL
6744.3769	31.2±14.3	NARVAL
6754.4270	33.0±8.1	NARVAL
6756.4720	24.4±5.7	NARVAL
6757.4436	14.9±5.7	NARVAL
6759.5429	7.3±7.0	NARVAL
6760.4614	16.6±6.2	NARVAL
6761.4555	10.6±5.9	NARVAL
6762.4030	17.1±8.0	NARVAL
6763.4675	13.5±5.9	NARVAL
6764.4372	1.0±5.7	NARVAL
6765.4610	4.6±7.1	NARVAL
6786.3669	18.8±6.7	NARVAL
6787.3714	3.9±6.0	NARVAL
9158.1132	−23.1±7.1	SPIRou
9159.1076	0.1±7.1	SPIRou
9208.0545	1.3±7.5	SPIRou
9209.1069	−3.3±7.3	SPIRou
9210.0431	−17.6±7.6	SPIRou
9213.1208	−10.8±10.0	SPIRou
9214.1222	−10.7±8.1	SPIRou
9215.0966	8.5±7.1	SPIRou
9217.1479	50.3±7.2	SPIRou
9218.0762	30.9±7.3	SPIRou
9219.0543	25.0±7.2	SPIRou
9220.0473	7.9±7.4	SPIRou
9221.0873	19.4±7.4	SPIRou
9222.0928	0.5±7.2	SPIRou
9223.0996	−25.3±7.2	SPIRou
9266.9790	−26.9±8.0	SPIRou
9268.0356	−34.3±6.9	SPIRou
9269.0974	−10.1±21.6	SPIRou
9269.1272	−10.5±9.9	SPIRou

Table E.5. Continued.

HJD [−2450000]	B_l [G]	Instrument
9271.9320	24.7±7.1	SPIRou
9274.1081	28.4±6.2	SPIRou
9276.0892	8.3±8.1	SPIRou
9277.0101	19.6±7.6	SPIRou
9278.0748	5.7±6.0	SPIRou
9294.0409	−22.1±6.3	SPIRou
9295.0002	−28.7±7.6	SPIRou
9296.0629	−16.8±8.1	SPIRou
9296.9974	−17.8±6.2	SPIRou
9298.0459	−15.9±6.3	SPIRou
9300.0194	13.8±10.0	SPIRou
9300.7965	17.5±7.2	SPIRou
9304.9681	24.8±7.1	SPIRou
9306.0155	3.7±6.5	SPIRou
9326.9507	21.8±7.5	SPIRou
9327.8698	24.1±7.1	SPIRou
9328.9553	24.1±7.5	SPIRou
9329.9107	8.5±10.4	SPIRou
9330.9185	5.0±14.0	SPIRou
9330.9527	56.5±16.7	SPIRou
9331.9585	31.4±7.2	SPIRou
9332.9564	20.3±6.7	SPIRou
9334.9279	4.2±6.4	SPIRou
9335.9337	−22.0±7.1	SPIRou
9336.9252	−34.0±8.0	SPIRou
9337.9127	−26.9±7.2	SPIRou
9384.7675	−16.4±10.6	SPIRou
9384.7722	−8.1±10.1	SPIRou
9385.7677	−4.6±7.5	SPIRou
9386.7639	39.9±6.2	SPIRou
9388.7451	27.9±6.9	SPIRou
9389.7431	17.5±6.3	SPIRou
9390.7491	−16.2±7.2	SPIRou
9391.7430	−36.3±6.2	SPIRou
9392.7444	−48.3±6.7	SPIRou
9393.7467	−53.5±6.2	SPIRou
9394.7425	−33.7±7.6	SPIRou
9395.7435	−19.6±8.5	SPIRou
9396.7434	−15.0±7.9	SPIRou
9397.7432	38.1±10.3	SPIRou
9412.7417	2.6±6.8	SPIRou
9414.7350	30.3±7.6	SPIRou
9535.1336	8.1±6.7	SPIRou
9536.1546	0.6±7.2	SPIRou
9537.1288	17.3±6.7	SPIRou
9538.1514	3.0±5.9	SPIRou
9539.1403	−3.0±7.2	SPIRou
9539.1662	11.7±6.8	SPIRou
9540.1354	−7.2±6.7	SPIRou
9541.1236	−2.4±6.4	SPIRou
9558.1411	−20.4±6.7	SPIRou
9559.1219	−5.6±8.1	SPIRou
9560.1639	−10.5±8.4	SPIRou
9562.1294	−2.2±6.1	SPIRou
9564.1142	23.9±7.1	SPIRou
9566.1686	26.4±11.7	SPIRou
9567.1335	2.1±7.6	SPIRou
9586.1341	−15.5±6.4	SPIRou

Table E.5. Continued.

HJD [−2450000]	B_l [G]	Instrument
9588.1546	−16.4±6.2	SPIRou
9589.1044	−25.0±6.1	SPIRou
9590.1329	−30.8±5.9	SPIRou
9592.1880	31.6±6.6	SPIRou
9593.1163	36.9±6.9	SPIRou
9594.1050	33.5±6.0	SPIRou
9595.1838	29.1±6.4	SPIRou
9596.1219	19.4±9.9	SPIRou
9597.1307	−4.8±6.3	SPIRou
9598.1769	−1.7±6.2	SPIRou
9599.1869	−22.7±6.2	SPIRou
9600.1802	−22.5±6.5	SPIRou
9602.1329	11.4±10.1	SPIRou
9604.1314	−14.0±5.8	SPIRou
9605.1515	−5.9±6.5	SPIRou
9606.1063	10.3±6.2	SPIRou
9611.1237	14.3±6.7	SPIRou
9612.1312	−15.2±10.5	SPIRou
9612.1363	2.1±9.6	SPIRou
9649.8702	28.7±5.8	SPIRou
9650.9574	15.3±6.9	SPIRou
9651.9774	28.7±6.2	SPIRou
9652.8562	23.9±6.0	SPIRou
9654.0191	−7.1±6.1	SPIRou
9655.0560	−3.6±7.0	SPIRou
9655.9679	−14.7±6.7	SPIRou
9657.0586	−14.8±8.5	SPIRou
9658.0488	−20.6±6.7	SPIRou
9658.9940	−19.4±6.0	SPIRou
9660.9905	5.4±7.6	SPIRou
9661.9645	9.8±6.3	SPIRou
9661.9996	9.8±6.3	SPIRou
9678.9852	12.5±6.7	SPIRou
9681.9729	−10.0±7.1	SPIRou
9682.9911	−34.1±6.7	SPIRou
9684.0050	−18.1±11.7	SPIRou
9684.9812	−15.7±7.0	SPIRou
9687.9818	−5.8±7.6	SPIRou
9688.9630	8.6±6.9	SPIRou
9689.9494	7.2±6.5	SPIRou
9690.9483	2.5±6.6	SPIRou
9710.8979	−5.0±7.4	SPIRou
9711.9059	−22.3±7.1	SPIRou
9712.8811	−13.4±7.7	SPIRou
9715.8525	−20.7±6.9	SPIRou
9716.8573	12.9±6.7	SPIRou
9732.7697	3.7±6.6	SPIRou
9733.7668	9.3±6.8	SPIRou
9735.7726	−1.8±6.7	SPIRou
9736.8406	−15.7±6.9	SPIRou
9738.7460	−4.2±6.9	SPIRou
9739.7468	−2.2±6.5	SPIRou
9740.7920	6.2±6.5	SPIRou

Table E.6. Optical and near-infrared measurements of longitudinal magnetic field for CN Leo. The columns are the same as in Table E.4.

HJD [−2450000]	B_l [G]	Instrument
4546.9935	−633.8±52.7	ESPaDOnS
4547.9162	−669.7±61.8	ESPaDOnS
4547.9584	−779.1±64.6	ESPaDOnS
4548.8749	−825.1±64.4	ESPaDOnS
8590.0095	−576.1±73.6	SPIRou
8591.8815	−632.6±70.9	SPIRou
8592.9476	−592.8±77.2	SPIRou
8593.8996	−577.7±71.6	SPIRou
8594.9831	−596.9±76.2	SPIRou
8595.8886	−551.8±69.6	SPIRou
8596.8984	−617.6±72.0	SPIRou
8597.8470	−554.8±69.2	SPIRou
8598.9095	−490.6±74.2	SPIRou
8599.8488	−651.8±67.0	SPIRou
8600.8511	−577.6±65.9	SPIRou
8604.8814	−579.3±73.0	SPIRou
8618.7890	−588.8±75.9	SPIRou
8647.7648	−645.6±77.5	SPIRou
8648.7456	−682.4±83.9	SPIRou
8650.7529	−529.2±76.1	SPIRou
8651.7412	−413.7±76.7	SPIRou
8653.7526	−656.2±79.1	SPIRou
8655.7683	−444.1±75.2	SPIRou
8788.1333	−441.9±51.6	SPIRou
8789.1453	−469.5±62.6	SPIRou
8790.1556	−460.3±54.0	SPIRou
8791.1274	−534.4±57.9	SPIRou
8795.1410	−437.4±73.6	SPIRou
8797.1180	−547.4±108.2	SPIRou
8799.1555	−493.0±91.1	SPIRou
8801.1211	−257.9±61.9	SPIRou
8802.1173	−492.1±66.4	SPIRou
8825.1497	−425.0±67.3	SPIRou
8826.1219	−512.7±58.9	SPIRou
8827.1148	−521.8±57.0	SPIRou
8828.0792	−401.8±56.5	SPIRou
8829.1393	−514.5±58.2	SPIRou
8830.1228	−440.7±56.5	SPIRou
8875.0195	−543.8±54.7	SPIRou
8876.0165	−533.8±52.2	SPIRou
8877.0519	−493.1±54.0	SPIRou
8884.8714	−509.5±51.8	SPIRou
8888.8471	−585.1±61.4	SPIRou
8895.8243	−512.7±51.0	SPIRou
8896.8945	−536.2±60.0	SPIRou
8897.8240	−423.4±52.0	SPIRou
8898.9247	−589.4±55.4	SPIRou
8920.0362	−461.1±51.3	SPIRou
8920.9668	−476.0±51.2	SPIRou
8976.9515	−568.9±60.1	SPIRou
8978.9097	−417.4±50.9	SPIRou
8981.9082	−535.9±52.8	SPIRou
8982.9114	−564.9±54.3	SPIRou
8983.8296	−382.6±49.4	SPIRou
8984.9152	−470.6±68.4	SPIRou
9005.7860	−451.6±56.9	SPIRou
9007.7960	−555.0±70.4	SPIRou

Table E.6. Continued.

HJD [−2450000]	B_l [G]	Instrument
9008.7620	−542.4±88.7	SPIRou
9009.7799	−623.4±86.5	SPIRou
9010.7947	−516.0±47.5	SPIRou
9154.1393	−492.8±49.1	SPIRou
9156.1488	−477.1±47.5	SPIRou
9157.1549	−508.2±51.2	SPIRou
9158.1171	−648.4±56.5	SPIRou
9159.1110	−438.6±53.6	SPIRou
9208.0541	−518.3±54.8	SPIRou
9209.1070	−662.0±56.2	SPIRou
9210.0437	−636.0±56.9	SPIRou
9213.1232	−470.8±61.8	SPIRou
9214.1247	−652.1±55.3	SPIRou
9215.0966	−665.6±57.3	SPIRou
9217.1484	−675.6±54.9	SPIRou
9218.0758	−504.9±54.8	SPIRou
9219.0537	−532.3±53.9	SPIRou
9220.0470	−585.9±57.6	SPIRou
9221.0871	−533.6±52.4	SPIRou
9222.0654	−561.2±54.3	SPIRou
9222.1785	−616.2±54.4	SPIRou
9223.0703	−585.6±55.9	SPIRou
9223.1694	−599.8±55.7	SPIRou
9266.9540	−531.2±66.8	SPIRou
9266.9611	−615.6±66.1	SPIRou
9267.9207	−609.4±56.4	SPIRou
9269.0286	−673.1±68.8	SPIRou
9271.8397	−581.6±56.3	SPIRou
9274.0918	−638.0±51.0	SPIRou
9276.0722	−563.4±54.4	SPIRou
9276.9937	−660.1±52.1	SPIRou
9278.0639	−568.2±43.7	SPIRou
9294.0260	−577.6±47.4	SPIRou
9294.9851	−576.7±48.1	SPIRou
9296.9796	−513.5±46.1	SPIRou
9298.0309	−632.2±48.3	SPIRou
9299.9950	−609.5±47.1	SPIRou
9300.7817	−634.4±53.6	SPIRou
9304.9542	−572.0±50.7	SPIRou
9306.0018	−610.6±47.3	SPIRou
9326.9362	−578.2±56.4	SPIRou
9327.8309	−703.8±52.3	SPIRou
9328.9436	−734.4±60.3	SPIRou
9329.8992	−666.4±58.8	SPIRou
9330.9062	−679.2±64.9	SPIRou
9331.9467	−644.3±51.2	SPIRou
9332.9448	−662.3±53.8	SPIRou
9334.8733	−607.8±48.0	SPIRou
9335.8928	−627.8±49.3	SPIRou
9336.9136	−643.4±67.4	SPIRou
9337.8936	−620.4±54.8	SPIRou
9337.9004	−620.4±54.8	SPIRou
9384.7522	−597.8±127.1	SPIRou
9384.7589	−592.4±86.9	SPIRou
9385.7605	−570.4±51.2	SPIRou

Table E.6. Continued.

HJD [−2450000]	B_l [G]	Instrument
9386.7563	−629.1±48.7	SPIRou
9388.7372	−544.6±44.0	SPIRou
9389.7348	−668.5±50.6	SPIRou
9390.7425	−663.1±54.5	SPIRou
9391.7408	−640.6±53.5	SPIRou
9392.7403	−654.5±48.1	SPIRou
9393.7396	−598.9±50.6	SPIRou
9394.7351	−688.8±54.2	SPIRou
9395.7354	−690.6±63.2	SPIRou
9396.7355	−649.1±54.8	SPIRou
9397.7355	−674.6±77.6	SPIRou
9535.1189	−525.7±50.9	SPIRou
9537.1315	−618.9±50.8	SPIRou
9538.1540	−665.1±50.5	SPIRou
9539.1427	−605.4±47.5	SPIRou
9540.1378	−584.7±46.5	SPIRou
9541.1259	−512.2±47.7	SPIRou
9558.1136	−555.7±64.6	SPIRou
9559.0945	−558.5±58.7	SPIRou
9560.1366	−618.6±55.3	SPIRou
9561.1177	−510.0±47.5	SPIRou
9562.0969	−508.2±45.8	SPIRou
9566.1400	−462.7±60.3	SPIRou
9588.1723	−477.5±48.5	SPIRou
9589.1213	−520.8±45.6	SPIRou
9590.1333	−528.1±44.8	SPIRou
9591.1360	−493.6±51.3	SPIRou
9593.1359	−566.9±46.5	SPIRou
9594.1235	−479.8±43.5	SPIRou
9595.1048	−387.1±69.0	SPIRou
9595.1835	−511.1±48.4	SPIRou
9596.1785	−516.0±53.0	SPIRou
9597.1172	−546.3±47.2	SPIRou
9598.1766	−480.6±43.1	SPIRou
9599.1694	−528.8±48.5	SPIRou
9600.1799	−539.3±46.3	SPIRou
9602.1193	−516.0±56.8	SPIRou
9603.0231	−470.1±48.3	SPIRou
9604.1525	−467.0±44.8	SPIRou
9605.1213	−542.9±47.7	SPIRou
9606.1404	−512.9±47.7	SPIRou
9607.1284	−478.2±45.9	SPIRou
9611.1429	−497.2±46.0	SPIRou
9612.1366	−575.6±56.6	SPIRou
9649.8597	−577.9±45.3	SPIRou
9650.8614	−556.2±46.2	SPIRou
9651.8345	−516.9±44.7	SPIRou
9653.9425	−492.8±43.1	SPIRou
9655.8643	−519.3±49.3	SPIRou
9658.9112	−536.1±43.8	SPIRou
9660.9072	−486.9±57.1	SPIRou
9681.9599	−566.0±50.8	SPIRou
9687.9746	−448.5±49.7	SPIRou
9710.8875	−624.3±55.3	SPIRou
9713.9000	−607.5±61.9	SPIRou
9740.7523	−496.4±43.6	SPIRou